LEVEL Ⅱ 12

A HYBRID TECHNIQUE FOR COMBINING THE MOMENT METHOD TREATMENT OF WIRE ANTENNAS WITH THE GTD FOR CURVED SURFACES

Ernest P. Ekelman, Jr.
Gary A. Thiele

The Ohio State University

ElectroScience Laboratory

Department of Electrical Engineering
Columbus, Ohio 43212

D D C

SEP 12 1978

F

78 08 11 012

NOTICES

When Government drawings, specifications, or other data are used for any purpose other than in connection with a definitely related Government procurement operation, the United States Government thereby incurs no responsibility nor any obligation whatsoever, and the fact that the Government may have formulated, furnished, or in any way supplied the said drawings, specifications, or other data, is not to be regarded by implication or otherwise as in any manner licensing the holder or any other person or corporation, or conveying any rights or permission to manufacture, use, or sell any patented invention that may in any way be related thereto.

REPORT DOCUMENTATION PAGE		READ INSTRUCTIONS BEFORE COMPLETING FORM
1. REPORT NUMBER	2. GOVT ACCESSION NO.	3. RECIPIENT'S CATALOG NUMBER
4. TITLE (and Subtitle) A HYBRID TECHNIQUE FOR COMBINING THE MOMENT METHOD TREATMENT OF WIRE ANTENNAS WITH THE GTD FOR CURVED SURFACES		5. TYPE OF REPORT & PERIOD COVERED Technical Report
		6. PERFORMING ORG. REPORT NUMBER ESL-784372-5
7. AUTHOR(s) Ernest P. Ekelman, Jr. Gary A. Thiele		8. CONTRACT OR GRANT NUMBER(s) Contract N00014-76-C-0573
9. PERFORMING ORGANIZATION NAME AND ADDRESS The Ohio State University ElectroScience Laboratory, Department of Electrical Engineering, Columbus, Ohio 43212		10. PROGRAM ELEMENT, PROJECT, TASK AREA & WORK UNIT NUMBERS Project No. NR 371-108/12-29-77 (427)
11. CONTROLLING OFFICE NAME AND ADDRESS Department of the Navy, Office of Naval Research 800 N. Quincy Street Arlington, Virginia 22217		12. REPORT DATE July 1978
		13. NUMBER OF PAGES 126
14. MONITORING AGENCY NAME & ADDRESS(If different from Controlling Office)		15. SECURITY CLASS. (of this report) Unclassified
		15a. DECLASSIFICATION/DOWNGRADING SCHEDULE

16. DISTRIBUTION STATEMENT (of this Report)

This document has been approved for public release and sale; its distribution is unlimited.

17. DISTRIBUTION STATEMENT (of the abstract entered in Block 20, if different from Report)

18. SUPPLEMENTARY NOTES

The material contained in this report is also used as a dissertation submitted to the Department of Electrical Engineering, The Ohio State University as partial fulfillment for the degree Doctor of Philosophy.

19. KEY WORDS (Continue on reverse side if necessary and identify by block number)

Hybrid method	Scattering
Moment method	Antennas
GTD	Geometrical optics
	Diffraction

20. ABSTRACT (Continue on reverse side if necessary and identify by block number)

The hybrid technique presented in this paper is a method for solving electromagnetic problems in which an antenna or other discontinuity is located on or near a conducting body, such as antennas on ships or aircraft. The technique solves these kinds of problems by properly analyzing the interaction between the antenna or scatterer and the conducting body. The hybrid technique accomplishes this by casting the antenna structure in a moment method format then modifying

DD FORM 1 JAN 73 **1473** EDITION OF 1 NOV 65 IS OBSOLETE

20.

that format to account for the effects of the conducting body via the geometrical theory of diffraction. The technique extends the moment method to handle many problems that cannot be solved by GTD or the moment method alone.

In general, arbitrary radiators located on or near canonical shapes or combinations thereof can be solved using the hybrid technique. Electromagnetic parameters for which the hybrid technique can solve include the near and far fields, current distributions, impedances, and scattering data. In this paper, wire antennas are analyzed to find their input impedance when they are located near perfectly-conducting circular cylinders.

The purpose of this paper is to present the technique and demonstrate some of its facility and its accuracy. Three orthogonal orientations were identified and antennas to match them were used. For each case, the hybrid solution is checked with one of three independent solutions; an MM-eigenfunction solution, image theory, or experimental measurement. The hybrid technique was verified for these orthogonal orientations. Thus a more general radiator with an arbitrary combination of orientations could be solved with confidence.

TABLE OF CONTENTS

iii

CHAPTER I

INTRODUCTION

In recent years the analysis of electromagnetic problems has been advanced tremendously by the digital computer and use of two powerful theories, the method of moments and the geometrical theory of diffraction. The moment method, MM, is a numerical technique which converts an integral equation, containing field terms and appropriate source terms that describe the electromagnetic problem, into a system of linear algebraic equations. The equations have unknown coefficients related to an expansion of a current distribution on the structure of interest. The moment method is characterized as a low frequency method since its practical use is limited to structures that are not electrically large. The geometrical theory of diffraction, GTD, is a ray optical method whose solution is based on the asymptotic approximation to the integral defining the electromagnetic problem. GTD is characterized as a high frequency method as it is applicable to bodies that are arbitrarily large electrically. Both of these methods are powerful computational tools which permit application to a wide range of problems. In this paper these two techniques are combined into a single technique called the "hybrid technique." The hybrid technique permits one to solve many problems that are not solvable by either technique alone.

The hybrid technique presented in this paper is a method for solving electromagnetic problems in which an antenna or other discontinuity is located on or near a conducting body, such as antennas on ships or aircraft, feed antennas near the reflecting surfaces of reflector antennas, and slots or other discontinuities on conducting surfaces. The technique solves these kinds of problems by properly analyzing the interaction between the antenna or scatterer and the conducting body. The hybrid technique accomplishes this by casting the antenna structure in a moment method format then modifying that format to account for the effects of the conducting body via the geometrical theory of diffraction. The technique extends the moment method to handle many problems that cannot be solved by GTD or the moment method alone.

The basic hybrid technique used in this paper was first described in the literature by Thiele and Newhouse [1]. In that paper the technique was applied to antennas on and near finite planar surfaces. The moment method solution was modified to account for the finite planar surfaces using wedge diffraction theory. In the present paper

1

a hybrid technique for combining the moment method treatment of wire antennas with the GTD for curved surfaces will be presented. Specifically, wire antennas will be analyzed near perfectly conducting circular cylinders.

The wire antenna will be cast in a moment method format given by Richmond [2,3] in his computer program for thin-wire structures. The use of piecewise sinusoidal basis functions in this method will be exploited. The effects of the cylinder will be found using GTD. The field expressions are obtained using the uniform geometrical theory of diffraction for an edge given by Kouyoumjian and Pathak [4]. The application of the GTD to the cylinder is based on techniques presented by Marhefka [5].

The hybrid technique as presented here is applicable to a much broader class of problems than those that are demonstrated. In general, arbitrary radiators located on or near canonical shapes or combinations thereof can be solved using the hybrid technique. The arbitrary radiator would be modeled with a thin-wire grid and set up in the moment method format. The conducting body is restricted to canonical shapes for which a GTD solution exists. Electromagnetic parameters for which the hybrid technique can solve include the near and far fields, current distributions, impedances, and scattering data. Of course, many geometries present special problems for which the technique will fail and therefore need to be modified. For example, part of the radiator might lie in the caustic of a needed GTD field.

It is impossible to cover all the possible applications of the hybrid technique in one paper. The purpose of this paper is to present the technique and demonstrate some of its facility and its accuracy. To accomplish this, various antenna radiators are considered in the presence of circular cylinders. Chapter II provides the theoretical background of the methods used in the hybrid technique. The method of moments with the specializations used is first described. Then the GTD expressions used in this paper are presented. In Chapter III the hybrid technique is described in detail. The very effective way in which GTD is incorporated into the thin-wire theory is presented and demonstrated.

Chapter IV is the results section in which the hybrid technique is applied to find the input impedance of antennas as a function of their distance from the circular cylinder. For each case, the hybrid solution is checked with one of three independent solutions, an MM-eigenfunction solution, image theory, or experimental measurement. Chapter V concludes the paper with a summary and discussion.

CHAPTER II

THEORETICAL BACKGROUND

In this chapter brief descriptions of the methods which are combined to form the hybrid technique used in this paper are presented. Since the development of these methods is not the subject of this paper, the descriptions will be short and not necessarily complete. Only the parts of the theories used in this paper will be presented. More complete explanations and developments can be found in the references cited.

The moment method part of the hybrid technique is the specialization used by Richmond in his thin-wire computer program [3]. The GTD part of the hybrid technique is programmed as presented by Marhefka [5]. These two references provided the major material for their respective theories in the development of the hybrid technique of this paper.

A.   Moment Method

A clear description of moment method is given by Stutzman and Thiele [6]. The moment method is a procedure for reducing an integral equation of the first kind of the form

$$\int_{\text{over structure}} I(z') \ K(z,z') \ dz' = - \ E^i(z) \tag{1}$$

to a system of simultaneous linear algebraic equations in terms of the unknown current distribution $I(z')$. Once the current is known, determination of radiation patterns and impedance is fairly straightforward. Electromagnetic radiation problems can almost always be expressed as integral equations in the form of Equation (1). The inhomogeneous source terms are on the right and the unknown currents are within the integral sign on the left.

1.   Weighted residuals and the moment method

A general moment method procedure can be accomplished by using the method of weighted residuals [6]. The unknown current $I(z')$ is expanded on the structure of interest using an appropriate expansion

3

function, $J_n(z')$. Equation (1) becomes a sum of the expansion terms as follows:

$$\sum_{n=1}^{N} I_n \int_{\text{over structure}} J_n(z')K(z,z')dz' = - E^i(z). \tag{2}$$

A residual R is defined to be the sum of the tangential components of scattered and incident fields

$$R = E_{\text{tan}}^{s} + E_{\text{tan}}^{i} . \tag{3}$$

At points on the surface of the perfectly conducting structure of interest the residual must be zero. So

$$R = \sum_{n=1}^{N} I_n \int_{\text{over structure}} J_n(z')K(z,z')dz' + E^i(z) = 0 \tag{4}$$

where z is on the structure's surface. In the method of weighted residuals the I_n's are found so that the residual is forced to zero in an average sense. The weighted integrals of the residual are set equal to zero as

$$\int_{\text{over structure}} W_m \, Rdz = 0, \qquad m=1,2,\cdots N. \tag{5}$$

where W_m is the weighting or test function. The choice of expansion and weighting functions is very important and has been the subject of many papers. As a rule of thumb, it is desirable to choose expansion functions that closely resemble the anticipated form of the current on the structure of interest. It is often advantageous to use the same functions for the weighting functions as used for the expansion functions. This makes the procedure a Galerkin's method.

If the structure of interest is an antenna structure modeled by thin-wire segments, more specific expressions can be described. Substituting Equation (3) into Equation (5) gives

4

$$\int\limits_{\substack{over \\ wire}} \overline{W}_m \cdot \overline{E}^s \, d\ell + \int\limits_{\substack{over \\ wire}} \overline{W}_m \cdot \overline{E}^i \, d\ell = 0,$$

$$m = 1, 2, \cdots N. \tag{6}$$

Denoting the scattered field from the n-th expansion function of the current by $\overline{E}_n^s$, the mn-th term of the moment method impedance matrix is

$$Z_{mn} = \int\limits_{\substack{over \\ wire}} \overline{W}_m \cdot \overline{E}_n^s \, d\ell \tag{7}$$

and the m-th voltage matrix element is

$$V_m = -\int\limits_{\substack{over \\ wire}} \overline{W}_m \cdot \overline{E}^i \, d\ell \quad . \tag{8}$$

$\overline{W}_m$ is the m-th testing function located interior to the wire and on its axis. Rigorously, the test function should be located on the surface of the wires making Equations (7) and (8) double integrals over the wire surfaces. Placing the test function on the axis is an extension of the electric field boundary condition for the sake of mathematical simplification. This approximation makes it necessary to restrict the method to wires for which the radius is less than about $.007\lambda$.

The method of weighted residuals is equivalent to the steps in the usual development of the moment method where a linear operator and an appropriate inner product are defined. In terms of these concepts, Equations (7) and (8) are

$$Z_{mn} = \langle W_m, L(J_n) \rangle$$

$$V_m = \langle W_m, E^i \rangle \tag{9}$$

where $\langle , \rangle$ denotes the inner product and L is the linear operator acting on J_n to give $\overline{E}_n^s$.

5

2. Reaction integral equation

A general approach to the formulation of boundary value problems was presented by Rumsey [7] when he introduced a physical observable called <u>reaction</u>. His formulation resulted in the reaction integral equation in electromagnetic theory. Reaction is a measure of coupling between two sources. If the weighting function is taken to be a test source, then the impedance matrix elements given by Equation (7) may be taken as a calculation of the coupling between the m-th test source and the field from the n-th expansion function or actual source. Similarly, the m-th voltage matrix element in Equation (8) is interpreted as the coupling between the m-th test source and the incident E-field. In both cases the m-th test source current is reacted with the E-field from another source.

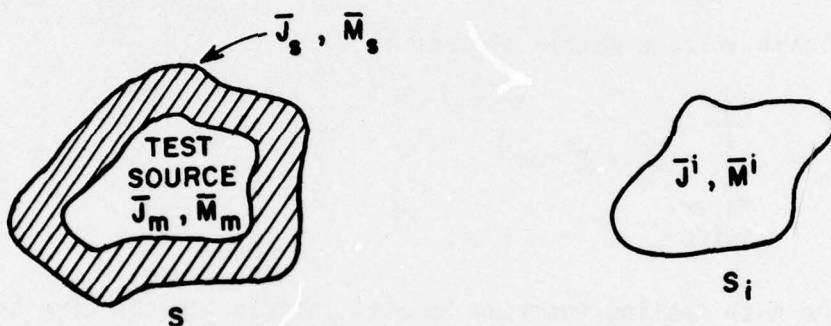For the very general geometry of Figure 1, a more general

Figure 1. Test source ($\overline{J}_m,\overline{M}_m$) inside conducting body surface S.

reaction integral equation is formed from which Equations (7) and (8) are found. Let ($\overline{J}_m,\overline{M}_m$) be the surface current densities of a test source and let ($\overline{E}_m,\overline{H}_m$) be the fields from that source. Equivalent surface-current densities are introduced

$$\overline{J}_s = \hat{n} \times \overline{H}$$

$$\overline{M}_s = \overline{E} \times \hat{n}$$

(10)

on the body S. ($\overline{J}_s,\overline{M}_s$) radiate the fields ($\overline{E}^s,\overline{H}^s$) in free space and replace the conducting body. The reaction integral and generalization of Equation (6) becomes

6

$$\iint_S (\bar{J}_m \cdot \bar{E}^s - \bar{M}_m \cdot \bar{H}^s) ds + \iint_S (\bar{J}_m \cdot \bar{E}^i - \bar{M}_m \cdot \bar{H}^i) ds = 0,$$

$$m = 1, 2, \cdots N \ . \tag{11}$$

where the integrals are over the test source's surface. The physical interpretation is that there is zero reaction or coupling between the test source and the sum of the incident and scattered fields. This is clearly equivalent to the weighted residual interpretation of Equation (5). If the fields from the n-th expansion function of the actual source current are given by $(\bar{E}_n^s, \bar{H}_n^s)$, the sum of the N fields being $(\bar{E}^s, \bar{H}^s)$, then for the general mn-th element in the impedance matrix

$$Z_{mn} = \iint_S (\bar{J}_m \cdot \bar{E}_n^s - \bar{M}_m \cdot \bar{H}_n^s) ds \ . \tag{12}$$

Similarly, the m-th voltage element is

$$V_m = - \iint_S (\bar{J}_m \cdot \bar{E}^i - \bar{M}_m \cdot \bar{H}^i) ds. \tag{13}$$

For the antenna situations of interest in this paper, $(\bar{E}^i, \bar{H}^i)$ originate from impressed currents $\bar{J}_i$ located on s.

3. Piecewise sinusoidal Galerkin method

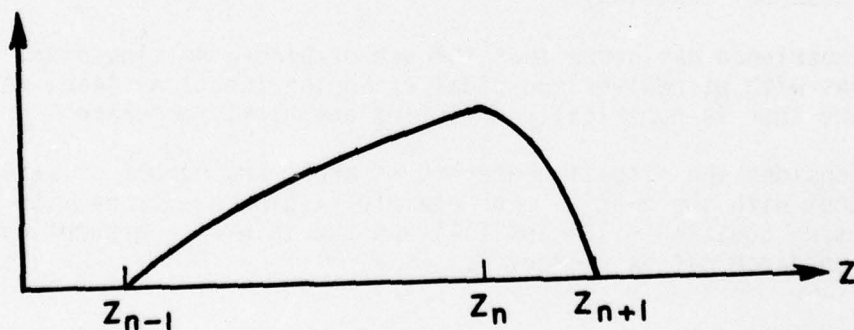The piecewise sinusoidal function as shown in Figure 2 is one of

Figure 2. Typical two segment dipole with piecewise sinusoidal distribution.

7

the most useful basis functions for wires in free space. It may be expressed mathematically for each z-directed segment by

$$I(z) = \frac{I_1 \sinh\gamma(z_2-z) + I_2\sinh\gamma(z-z_1)}{\sinh\gamma d} \tag{14}$$

where I_1 and I_2 are the endpoint currents, γ is the complex propagation constant of the medium, and $d=z_2-z_1$ is the source length. A piecewise sinusoidal approximation to a current distribution is given in Figure 3. Note that each piecewise sinusoidal function spans two
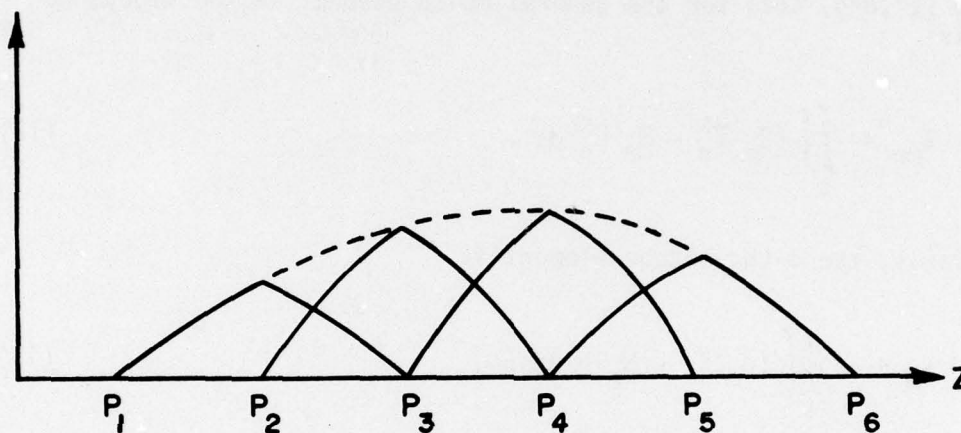

Figure 3. Current distribution modeled by overlapping piecewise sinusoidal modes.

connected segments and that each interior segment contains two piecewise sinusoidal functions.

Experience has shown that the use of piecewise sinusoidal testing functions with piecewise sinusoidal expansion functions leads to a procedure that is numerically efficient and highly accurate.

Consider the situation wherein an arbitrary number of segments are coincident with the z-axis. For example, a dipole antenna with N segments using Equations (12) and (14) and the thin-wire assumption, the mn-th impedance matrix element is

8

$$Z_{mn} = \int_{z_{m-1}}^{z_m} \frac{\sin\gamma(z-z_{m-1})}{\sin\gamma|z_{m-1}-z_m|} \; \hat{z}\cdot\overline{E}_n^s \; dz$$

$$+ \int_{z_m}^{z_{m+1}} \frac{\sin\gamma(z_{m+1}-z)}{\sin\gamma|z_m-z_{m+1}|} \; \hat{z}\cdot\overline{E}_n^s \; dz \quad . \tag{15}$$

$\overline{E}_n^s$ is needed to carry out Equation (15). This field may be found in a straightforward manner and the derivation is included in many electromagnetic texts including [6]. The geometry is shown in Figure 4. For the piecewise sinusoidal excitation current of Equation (14), $\overline{E}_n^s$ is
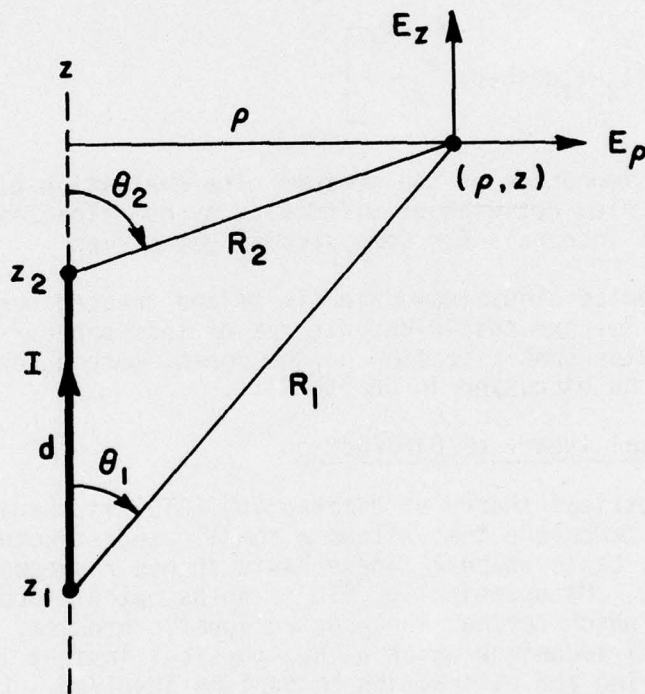

Figure 4.   z-directed monopole segment source with the observation point (ρ,z).

9

$$E_\rho = \frac{\eta}{4\pi\rho\sinh\gamma d} \left[\left(I_1 e^{-\gamma R_1} - I_2 e^{-\gamma R_2} \right) \sinh\gamma d \right.$$

$$+ (I_1\cosh\gamma d - I_2)e^{-\gamma R_1}\cos\theta_1$$

$$\left. + (I_2\cosh\gamma d - I_1)e^{-\gamma R_2}\cos\theta_2 \right] \tag{16}$$

$$E_z = \frac{\eta}{4\pi\sinh\gamma d} \left[(I_1 - I_2\cosh d)\frac{e^{-\gamma R_2}}{R_2} \right.$$

$$\left. + (I_2 - I_1\cosh\gamma d)\frac{e^{-\gamma R_1}}{R_1} \right] \tag{17}$$

where η is the impedance of the medium. The evaluation of Equation (15) may be carried out without difficulty by numerical integration or by Si and Ci integrals for some special geometries.

The piecewise sinusoidal Galerkin method treated here is the procedure used for the thin-wire antennas of this paper. The importance of this particular specialization of the moment method for the hybrid technique will be discussed in Chapter III.

B.   Geometrical Theory of Diffraction

The geometrical theory of diffraction (GTD) is characterized as a high frequency technique that allows a complicated structure to be approximated by basic shapes. These basic shapes represent canonical problems in GTD. Mathematically, GTD is an asymptotic approximation to an integral which defines the electromagnetic problem. The GTD is a ray optical technique which allows physical insight into the various scattering and diffraction mechanisms involved. Consequently, the dominant or significant scattering or diffraction mechanism for a given geometry can be identified leading to an accurate engineering solution.

Again, only the solutions needed for the problems solved in this paper are presented. More cases and derivations including more complete explanations are found in the literature cited.

10

In the format of GTD, the total electric field may be represented as

$$\bar{E} = \bar{E}^i u^i + \bar{E}^r u^r + \bar{E}^d \quad . \tag{18}$$

The $\bar{E}^i$ field is the incident field in free space. $\bar{E}^r$ is the field reflected from the surface of the structure of interest. $\bar{E}^d$ is the diffracted field from discontinuities of the structure, such as edges, corners, or curved surfaces. u^i and u^r are unit step functions to cut off their corresponding field at the incident and reflection shadow boundaries. The extent of these fields is determined by geometrical optics (GO). The surfaces in this paper are all perfectly conducting and the medium is free space. Also the $e^{j\omega t}$ time dependence is assumed and not explicitly shown.

1. Geometrical optics field

The incident electric field $\bar{E}^i$ is considered to be a spherical wave for the equations given in this paper. Other cases have been treated in the literature but the importance of using the spherical wave expressions in the hybrid technique will be discussed in the next chapter.

The reflected electric field from a curved surface S, as shown in Figure 5, is given in geometrical optics terms by

$$\bar{E}^r(s) = \bar{E}^i(Q_R) \cdot \bar{\bar{R}} \sqrt{\frac{\rho_1^r \rho_2^r}{(\rho_1^r + s)(\rho_2^r + s)}} \; e^{-jks} \quad . \tag{19}$$

$\bar{E}^i(Q_R)$ is the incident field at the reflection point (Q_R) on the surface and $\bar{\bar{R}}$ is the dyadic reflection coefficient such that

$$\bar{\bar{R}} = \hat{e}_{\parallel}^i \hat{e}_{\parallel}^r - \hat{e}_{\perp} \hat{e}_{\perp} \quad . \tag{20}$$

Unit vectors $\hat{e}_{\parallel}^i$ and $\hat{e}_{\parallel}^r$ are parallel to the plane of incidence and the unit vector $\hat{e}_{\perp}$ is perpendicular to the plane of incidence. The point of reflection Q_R is found from the laws of reflection which state that the angle of incidence is equal to the angle of reflection. That is

$$- \hat{I} \cdot \hat{n} = \hat{S} \cdot \hat{n} \tag{21}$$

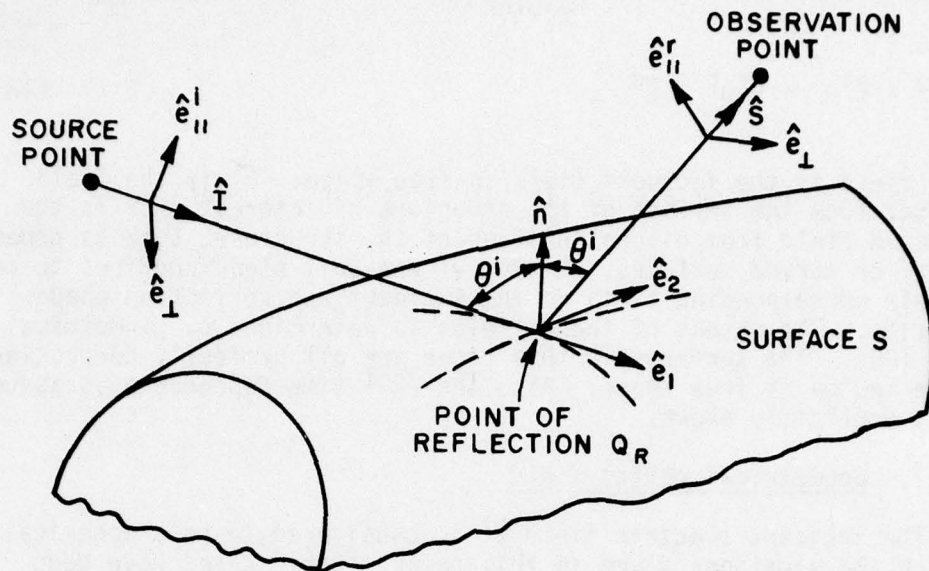and that the incident, reflected, and surface normal vectors all lie in the same plane

11

OBSERVATION
POINT

$\hat{e}_{\parallel}^r$

$\hat{e}_{\parallel}^i$

SOURCE
POINT

$\hat{S}$

$\hat{e}_\perp$

$\hat{I}$

$\hat{e}_\perp$

$\hat{n}$

θ^i θ^i

$\hat{e}_2$

$\hat{e}_1$

SURFACE S

POINT OF
REFLECTION Q_R

Figure 5.   Reflection by a smooth
convex surface.

$$\hat{I} \times \hat{n} = \hat{S} \times \hat{n} \quad . \tag{22}$$

Finding Q_R will be considered in more detail in the last section of this chapter.

The quantities ρ_1^r and ρ_2^r are the principal radii of curvature of the reflected wavefront at the reflection point Q_R. Kouyoumjian and Pathak [4] show how to find these values for an arbitrary wavefront by diagonalizing the curvature matrix for the reflected wavefront given by Deschamps [8]. The wavefront is incident on the curved surface S shown in Figure 5 at the reflection point Q_R. Unit vectors $\hat{e}_1$ and $\hat{e}_2$ are in the principal direction of S at Q_R with surface radii of curvature R_1 and R_2. For the case where the incident field is spherical, the principal radii of curvature of the reflected wavefront are given by Kouyoumjian and Pathak as

$$\frac{1}{\rho_{1,2}^r} = \frac{1}{s'} + \frac{1}{\cos\theta^i}\left[\frac{\sin^2\theta_2}{R_1} + \frac{\sin^2\theta_1}{R_2}\right]$$
$$\pm \sqrt{\frac{1}{\cos^2\theta^i}\left[\frac{\sin^2\theta_2}{R_1} + \frac{\sin^2\theta_1}{R_2}\right]^2 - \frac{4}{R_1 R_2}} \quad . \tag{23}$$

12

S' is the radius of curvature of the incident wavefront at Q_R, θ_1 is the angle between the direction of the incident ray $\hat{I}$ and unit vector $\hat{e}_1$, and θ_2 is the angle between the direction of the incident ray $\hat{I}$ and the unit vector $\hat{e}_2$.

2. Diffraction by a curved wedge

The curved wedge problem is illustrated in Figures 6 and 7. This report will consider finite cylinders where the ends of the cylinders are formed by a flat surface with a resulting curved wedge. The diffracted field due to the curved wedge is analyzed using GTD techniques developed by Kouyoumjian and Pathak [4].

The diffracted field from the curved wedge is written in the form

$$\bar{E}^d(s) \sim \bar{E}^i(Q_E) \cdot \bar{D}_E(\hat{s}, \hat{I}) \sqrt{\frac{\rho}{s(\rho+s)}} \ e^{-jks} \ . \tag{24}$$

The ρ is the distance between the caustic at the edge and the second caustic of the diffracted ray. It is given by

$$\frac{1}{\rho} = \frac{1}{\rho_e^i} - \frac{\hat{n}_e \cdot (\hat{I}-\hat{S})}{a_e \sin^2\beta_o} \tag{25}$$

where ρ_e^i, $\hat{n}_e$, a_e will be defined shortly. The diffraction coefficients for the curved wedge are extended from those for wedge diffraction to allow the diffracted field to be continuous at the incident and reflected shadow boundaries. To accomplish this the appropriate distance parameters L in each of the transition functions make the fields continuous. The diffraction coefficient for the curved wedge is given by

$$D_{s,h}(\phi,\phi',\beta_o) = \frac{e^{-j\pi/4}}{2n\sqrt{2\pi k}\sin\beta_o} \left[\frac{2\,\sin(\frac{\pi}{n})F[kL^i a(\beta^-)]}{\cos(\frac{\pi}{n})-\cos(\frac{\beta^-}{n})} \right.$$

$$\pm \left\{ \cot\left(\frac{\pi+\beta^+}{2n}\right) F[kL^{rn}a^+(\beta^+)] \right.$$

$$\left. \left. + \cot\left(\frac{\pi-\beta^+}{2n}\right) F[kL^{ro}a(\beta^+)] \right\} \right] \tag{26}$$

where $a(\beta) = 2\cos^2\beta/2$ and $a^+(\beta) = 2\cos^2\frac{(2\pi n-\beta)}{2}$.

13

S' is the radius of curvature of the incident wavefront at Q_R, θ_1 is the angle between the direction of the incident ray $\hat{I}$ and unit vector $\hat{e}_1$, and θ_2 is the angle between the direction of the incident ray $\hat{I}$ and the unit vector $\hat{e}_2$.

2. Diffraction by a curved wedge

The curved wedge problem is illustrated in Figures 6 and 7. This report will consider finite cylinders where the ends of the cylinders are formed by a flat surface with a resulting curved wedge. The diffracted field due to the curved wedge is analyzed using GTD techniques developed by Kouyoumjian and Pathak [4].

The diffracted field from the curved wedge is written in the form

$$\bar{E}^d(s) \sim \bar{E}^i(Q_E) \cdot \bar{D}_E(\hat{s},\hat{I}) \sqrt{\frac{\rho}{s(\rho+s)}} \ e^{-jks} \ . \tag{24}$$

The ρ is the distance between the caustic at the edge and the second caustic of the diffracted ray. It is given by

$$\frac{1}{\rho} = \frac{1}{\rho_e^i} - \frac{\hat{n}_e \cdot (\hat{I}-\hat{S})}{a_e \sin^2\beta_o} \tag{25}$$

where ρ_e^i, $\hat{n}_e$, a_e will be defined shortly. The diffraction coefficients for the curved wedge are extended from those for wedge diffraction to allow the diffracted field to be continuous at the incident and reflected shadow boundaries. To accomplish this the appropriate distance parameters L in each of the transition functions make the fields continuous. The diffraction coefficient for the curved wedge is given by

$$D_{s,h}(\phi,\phi',\beta_o) = \frac{e^{-j\pi/4}}{2n\sqrt{2\pi k}\sin\beta_o} \left[\frac{2 \sin(\frac{\pi}{n})F[kL^i a(\beta^-)]}{\cos(\frac{\pi}{n})-\cos(\frac{\beta^-}{n})} \right.$$

$$\pm \left\{ \cot\left(\frac{\pi+\beta^+}{2n}\right) F[kL^{rn}a^+(\beta^+)] \right.$$

$$\left. + \cot\left(\frac{\pi-\beta^+}{2n}\right) F[kL^{ro}a(\beta^+)] \right\} \left. \vphantom{\frac{\frac{\pi}{n}}{\frac{\pi}{n}}} \right] \tag{26}$$

where $a(\beta) = 2\cos^2\beta/2$ and $a^+(\beta) = 2\cos^2\frac{(2\pi n-\beta)}{2}$.

13
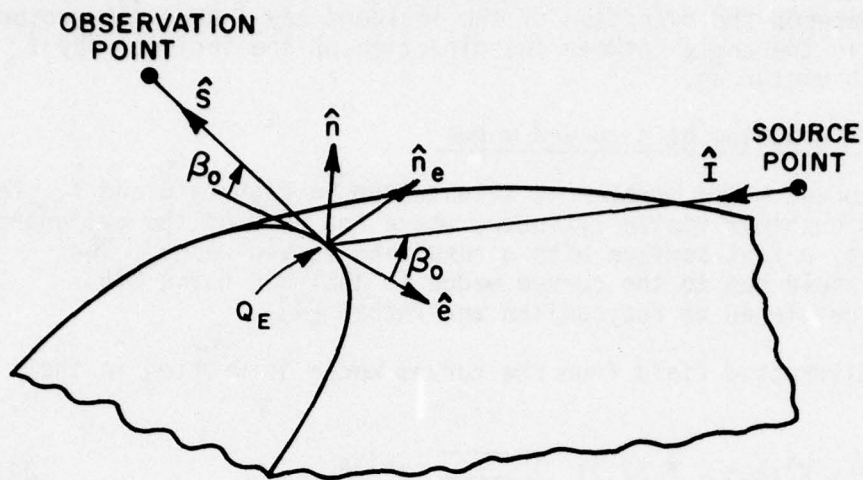
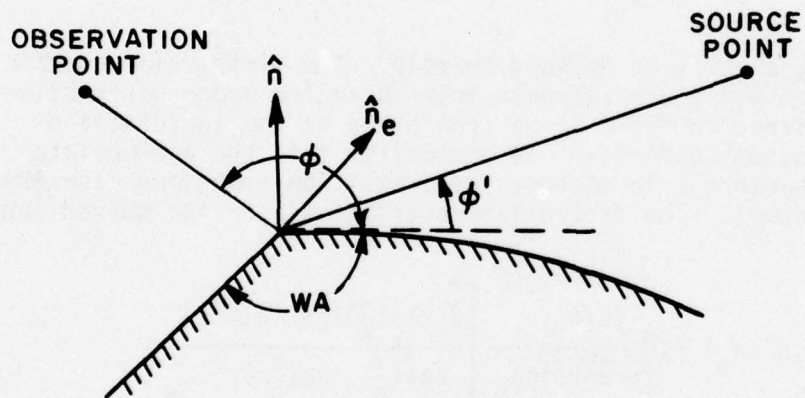Figure 6. Geometry for the three-dimensional
curved wedge diffraction problem.

Figure 7. The curved wedge in the plane
perpendicular to ê at Q_E.

14

The D_s coefficient applies for the E-field vector parallel to the edge (i.e., acoustically soft $\bar{E}|_{Edge} = 0$) while D_h applies to the field component perpendicular to the edge (i.e., acoustically hard $\frac{\partial \bar{E}}{\partial n}\Big|_{Edge} = 0$). The angular relationships are expressed by $\beta \approx \beta^{\mp} = \phi \mp \phi'$. The transition function F(x) is

$$F(x) = 2j \ |\sqrt{x}| \ e^{jx} \int_{|\sqrt{x}|}^{\infty} e^{-jz^2} \, dz \quad . \tag{27}$$

The distance parameter associated with the incident field is given by

$$L^i = \frac{s(\rho_e^i + s)\rho_1^i \rho_2^i \sin^2 \beta_0}{\rho_e^i (\rho_1^i + s)(\rho_2^i + s)} \quad . \tag{28}$$

The distance parameter associated with the reflected field from the surface with superscript o (reflection boundary at $\pi - \phi'$) and the reflected field from the surface with superscript n (reflection boundary $(2n-1)\pi - \phi'$) is given by

$$L^r = \frac{s(\rho_e^r + s)\rho_1^r \rho_2^r \sin^2 \beta_0}{\rho_e^r (\rho_1^r + s)(\rho_2^r + s)} \quad . \tag{29}$$

The parameter ρ_e^i is the radius of curvature of the incident wavefront at the diffraction point Q_E taken in the plane containing the incident ray and the unit vector $\hat{e}$ which is tangent to the edge at Q_E. For the case of spherical waves $\rho_e^i = s'$. ρ_1^i and ρ_2^i are the principal radii of curvature of the incident wavefront at Q_E. Similarly, ρ_1^r and ρ_2^r are the principal radii of crrvature of the reflected wavefront at Q_E, which are found using Equation (23) for spherical wavefront incidence also, the parameter ρ_e^r is the radius of curvature of the reflected wavefront at Q_E taken in the plane containing the reflected ray and $\hat{e}$. It is found using

$$\frac{1}{\rho_e^r} = \frac{1}{\rho_e^i} - \frac{2(\hat{n} \cdot \hat{n}_e)(\hat{I} \cdot \hat{n})}{a_e \sin^2 \beta_0} \tag{30}$$

15

where $\hat{n}$ is the unit vector normal to the surface at Q_E, $\hat{n}_e$ is the associated unit normal to the edge directed away from the center of curvature, and $a_e > 0$ is the radius of curvature of the edge at Q_E.

3. Specular point calculation

The previous sections presented the GO and GTD E-field expressions assuming that the specular point Q_R and Q_E were already known on the surface. For special geometries they are often known intuitively. Marhefka [5] has presented several methods for finding these points for more general geometries. Greer and Burnside [9] have also investigated various methods of finding edge diffraction points. The reflection point Q_R on the surface of a circular cylinder is desired when a nearby source and field point are known. A method presented by Marhefka was modified to accomplish this. Figure 8 shows the geometry for the determination of the reflection point on an elliptic cylinder.
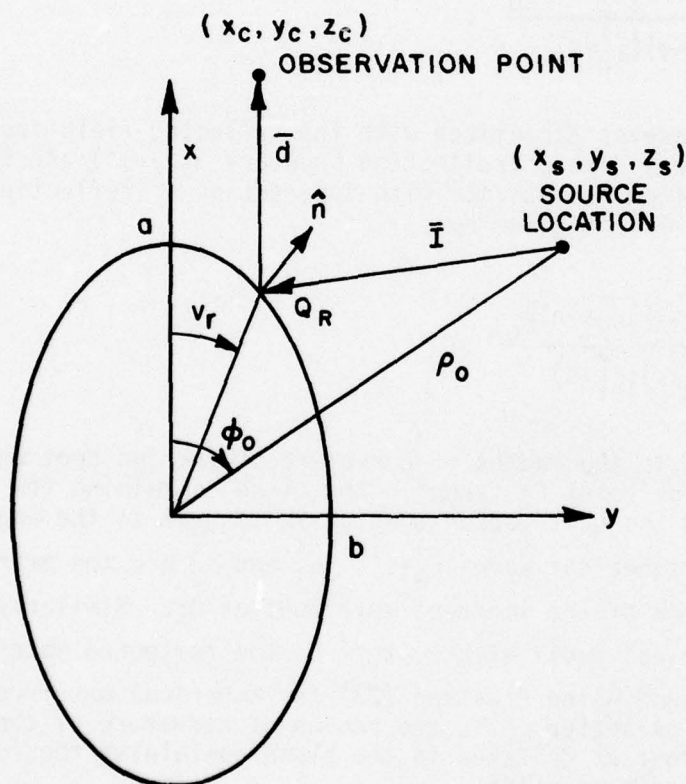
Figure 8. Geometry for determination of reflection point on elliptic cylinder.

16

To find the reflection point in the lit zone, the laws of reflection as given by Equations (21) and (22) are the starting point. These equations are written such that

$$\frac{-\overline{n} \cdot \overline{I}}{\overline{n} \cdot \overline{d}} = \frac{|\overline{d}|}{|\overline{I}|} = \frac{\overline{n} \times \overline{I}}{\overline{n} \times \overline{d}} \tag{31}$$

or

$$(\overline{n} \times \overline{I})(\overline{n} \cdot \overline{d}) + (\overline{n} \cdot \overline{I})(\overline{n} \times \overline{d}) = 0. \tag{32}$$

Note that the normalization factors may be removed. The incident and observation vectors are written as follows

$$\overline{I}(v,z) = I_x(v)\hat{x} + I_y(v)\hat{y} + I_z(z)\hat{z}$$

$$= (a \cos v - x_s)\hat{x} + (b \sin v - y_s)\hat{y} + (z - z_s)\hat{z} \tag{33}$$

and

$$\overline{d}(v,z) = d_x(v)\hat{x} + d_y(v)\hat{y} + \overline{d}_z(z)\hat{z}$$

$$= (x_c - a \cos v)\hat{x} + (y_c - b \sin v)\hat{y} + (z_c - z)\hat{z} \tag{34}$$

The normal to the curved surface is given in general by

$$\overline{n} = \hat{t}_e \times \hat{z} = b \cos v \, \hat{x} + a \sin v \, \hat{y}$$

or

$$\overline{n} = n_x(v)\hat{x} + n_y(v)\hat{y} . \tag{35}$$

Performing the necessary dot and cross products, Equation (32) becomes two equations

$$f(v,z) = (n_x I_x + n_y I_y)(n_x d_y - n_y d_x) + (n_x d_x + n_y d_y) \cdot$$

$$\cdot (n_x I_y - n_y I_x) = 0 \tag{36}$$

and

17

$$g(v,z) = (n_x I_x + n_y I_y)d_z + (n_x d_x + n_y d_y)I_z = 0. \tag{37}$$

Then the values of Equations (33), (34), and (35) are substituted into Equation (36) with the fact $\alpha = e^{jv}$. The equation is multiplied out and like terms in α are collected so that a sixth order polynomial is obtained given by

$$C_6\alpha^6 + C_5\alpha^5 + C_4\alpha^4 + C_3\alpha^3 + C_2\alpha^2 + C_1\alpha^1 + C_0 = 0 \tag{38}$$

where

$$C_6 = (a^2-b^2)\,[a(y_c+y_s) + jb(x_c+x_s)]$$

$$C_5 = -2(a^2+b^2)\,(x_s y_c + y_s x_c) - j4ab[(a^2-b^2) + (x_s x_c - y_s y_c)]$$

$$C_4 = a(5b^2-a^2)\,(y_c+y_s) + jb(5a^2-b^2)(x_c+x_s)$$

$$C_3 = 4(a^2-b^2)(x_s y_c + y_s x_c)$$

$$C_2 = C_4^* \text{ (complex conjugate of } C_4)$$

$$C_1 = C_5^*$$

$$C_0 = C_6^* \quad .$$

The six roots of the polynomial correspond to v in that

$$v = \tan^{-1}\frac{\text{Im}(\alpha)}{\text{Re}(\alpha)} \quad . \tag{39}$$

The value which is the true reflection point is found by determining the v that minimizes the distance given by $|\bar{I}| + |\bar{d}|$, which is necessary to satisfy Fermat's principle. Using this v parameter representing the reflection point in the x-y plane, the z-coordinate can be found from Equation (37) to be

$$z_r = \frac{(n_x d_x + n_y d_y)z_s - (n_x I_x + n_y I_y)\,z_c}{(n_x d_x + n_y d_y) - (n_x I_x + n_y I_y)} \quad . \tag{40}$$

18

The above method for finding the reflection point can be considered exact. It is, however, slow for some applications and other methods are presented in the references mentioned above.

In conclusion, the moment method and the GTD material presented in this chapter are by no means complete. The material does, however, provide the background and the equations necessary for the hybrid technique developed in the next chapter. The expressions given here are the ones used in the computer programs to obtain the results of Chapter IV.

CHAPTER III

THE HYBRID TECHNIQUE

In this chapter the hybrid technique is described in detail. The various problems arising when GTD is combined with the moment method are presented and solved. Results are included which demonstrate the effectiveness of these solutions.

A. Description

The hybrid technique is used here to solve electromagnetic problems in which antennas or other discontinuities are located on or near a large conducting structure. The basic technique was first presented in the literature by Thiele and Newhouse [1]. This method consists of casting the antenna structure in a moment method format and then modifying the generalized impedance matrix to account for the effects of the conducting body via GTD.

Following the notation used by Thiele and Newhouse, the moment method is applied to the antenna structure alone by expanding the surface current J in a series of basis functions J_1, J_2, J_3 $\cdots$, such that

$$J = \sum_{n=1}^{N} I_n J_n \; . \tag{41}$$

A linear operator L is defined to relate the expansion currents to their electric fields. A set of weighting functions W_1, W_2, $W_3 \cdots$ is selected and an inner product is defined so that,

$$\sum_{n=1}^{N} I_n \langle W_m, L(J_n) \rangle = \langle W_m, E^i \rangle, \tag{42}$$

where E^i is the field incident on the antenna. This is the m-th row of the system of N equations described in Section A of Chapter II under the moment method. Equation (42) is represented as

$$[Z] \, (I) = (V). \tag{43}$$

The elements of this impedance matrix are those of the free space impedance matrix since only the antenna structure has been considered so far. These elements are given by

$$Z_{mn} = \langle W_m, L(J_n) \rangle. \tag{44}$$

The inner product forms a unitary space in which

$$\langle J, aE_1 + bE_2 \rangle = a\langle J, E_1 \rangle + b\langle J, E_2 \rangle, \tag{45}$$

where a and b are complex scalars. If aE_1 in Equation (45) represents $L(J_n)$ in Equation (44) (that is, the field due to J_n) and if bE_2 in Equation (45) represents an additional field contribution to Z_{mn} (that is also due to J_n but not due to the field arriving directly), then

$$Z_{mn}' = \langle W_m, aE_1 + bE_2 \rangle$$

$$= \langle W_m, L(J_n) + bL(J_n) \rangle \quad, \quad a=1, b=b(m,n) \tag{46}$$

or

$$Z_{mn}' = \langle W_m, L(J_n) \rangle + \langle W_m, bL(J_n) \rangle$$

$$= Z_{mn} + Z_{mn}^g. \tag{47}$$

The superscript g indicates that Z_{mn}^g is added to each impedance matrix term to account for contributions at the m-th observation point due to the J_n fields scattered from the conducting body. Thus Equation (43) becomes

$$[Z'] [I'] = (V) \tag{48}$$

where $[Z']$ is the generalized impedance matrix properly modified to account for the presence of the scattering body as well as for the antenna itself. Z_{mn}^g elements are found with the aid of GTD. The solution of Equation (48) is

$$(I') = [Z']^{-1} (V) \tag{49}$$

where (I') is the current on the antenna structure located on or near the conducting body. Thus the hybrid technique used in this paper is a modification or extension of the moment method. This differs from other approaches that consider extension of GTD via the method of moments [10].

21

The starting point for the hybrid technique used in this paper is Richmond's thin-wire program [2,3]. Some reasons for this choice are obvious. It is a very general and powerful technique for modeling and solving a great variety of antenna and scattering problems with relatively simple inputs to the computer code, it is widely known and used, and its accuracy has been repeatedly demonstrated. The practical limitation on its capabilities is the size of the impedance matrix required by the geometry of the particular problem. The computer must invert and solve this matrix. Long and expensive computer runs become a problem if the structure is electrically large.

Another less obvious reason for choosing Richmond's thin-wire approach is that it uses piecewise sinusoidal expansion and weighting basis functions. The advantages of these functions other than rapid convergence and the corresponding mode economy, are made clear in the section of this chapter on integrating GTD with the moment method.

To facilitate a more detailed explanation of the hybrid technique, its application to a specific geometry is presented. The case chosen is a half-wave dipole, axially oriented, near a perfectly conducting circular cylinder. The geometry is depicted in Figure 9. The current distribution on the dipole near the cylinder is determined and from this the input impedance is calculated. The choice of this particular geometry and determination of the input impedance does not imply restrictions on the hybrid technique described. This method can be applied to an arbitrarily shaped radiator near any scattering structure for which a GTD solution exists. It may be used to find near and far fields and scattering data as well as current distributions and input impedance.

The dipole in Figure 9 is divided into segments not longer than a quarter wavelength in extent. These segments are grouped two at a time to form modes. A moment method formulation of the dipole in free space is first carried out by assuming a piecewise sinusoidal current distribution on a particular two-segment mode. This test mode current generates an E-field which is reacted with all of the two-segment modes on the dipole. Each of these reactions gives an impedance matrix term

$$Z_{jk} = - \int_{\text{Rec Mode k}} \bar{E}_j^i(\ell) \cdot I_k(\ell) \, \overline{d\ell} \tag{50}$$

$\bar{E}_j^i(\ell)$ is the E-field from test mode j at the receiving mode k. $I_k(\ell)$ is the expansion current distribution also assumed to be piecewise sinusoidal making this a Galerkin method. A row of the impedance matrix is created by carrying out this integration for each expansion mode on the dipole. The other rows are found by moving the test
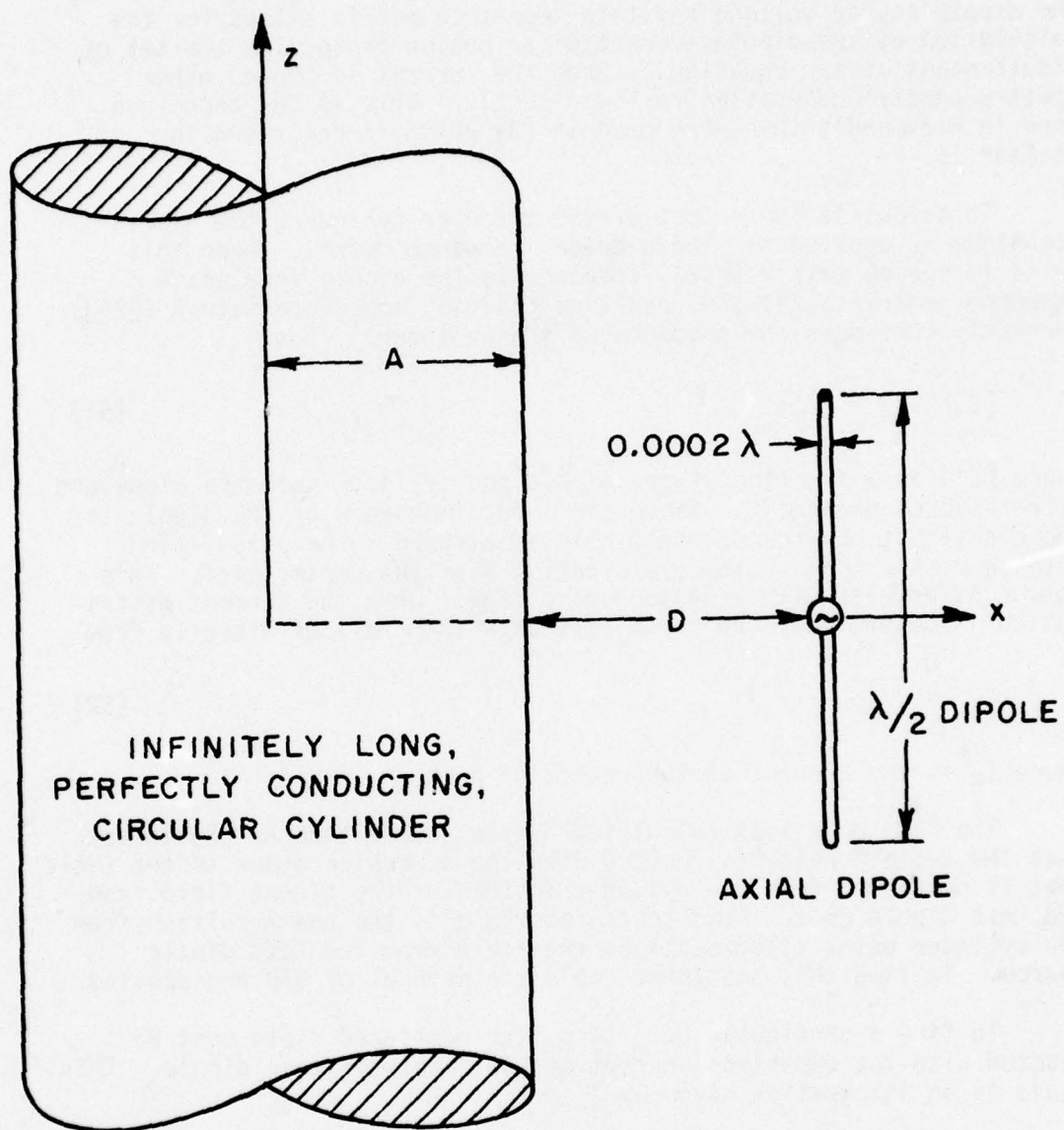
22

Figure 9. Half-wave dipole axially oriented a distance D from a
perfectly conducting circular cylinder of
radius A.

current source to each mode in turn. The resulting free space
impedance matrix is a function of the dipole geometry alone. Knowing
the dipole source voltage and this impedance matrix allows for the
calculation of the dipole current distribution by solving the set of
simultaneous linear equations. Once the current is known, other
electromagnetic quantities follow directly. This is the technique
used in Richmond's thin-wire program [3] which is described in
ChaPter II.

To calculate the effect of the circular cylinder, the hybrid
technique is applied to find a delta impedance matrix. When this
delta impedance matrix ([ΔZ]) is added to the dipole free space
impedance matrix ([Z]) the resulting modified impedance matrix ([Z'])
correctly considers the presence of the cylinder. Thus

$$[Z]+[\Delta Z] = [Z'] \qquad (51)$$

where [Z'] is a function of the dipole and cylinder geometry alone and
is not source dependent. Since the input impedance of the dipole is
the quantity to be found, the dipole is assumed to be a radiating
antenna with a known voltage excitation V at the center port. This
source is modeled with a delta gap voltage. When the current distri-
bution is determined, the input impedance then follows directly from

$$Z_{in} = V/I_g \qquad (52)$$

where I_g is the current at the generator port.

The [ΔZ] matrix is calculated by the same method as [Z] except
that the E-field which is reacted with the expansion modes is the field
that is scattered from the cylinder instead of the direct field from
the test dipole mode. This scattered field is the one resulting from
the cylinder being illuminated by the field from the test dipole
source. To find this scattered field the methods of GTD are applied.

To find a particular [ΔZ] term, the scattered field must be
reacted with the expansion current on the receiving mode dipole. This
again is an integration given by

$$\Delta Z_{jk} = - \int_{Rec\ Mode\ k} \overline{E}_j^s(\ell) \cdot I_k(\ell) \; \overline{d\ell} \qquad (53)$$

where $I_k(\ell)$ is the piecewise sinusoidal distribution on the receiving
mode dipole k and $\overline{E}_j^s$ is the field scattered from the cylinder when
illuminated by the test source $I_j(\ell)$ which also has an assumed piece-

24

wise sinusoidal distribution. This integration is carried out numerically using the Newton-Cotes equation after $\bar{E}^s(\ell)$ has been determined. In the computer program, these mode-to-mode ΔZ_{jk}'s are found by combining the appropriate segment-to-segment mutual impedance terms. Again, this procedure is modeled after Richmond's thin-wire program. Each mode impedance term results from the superposition of four segment impedances making it possible to have two segment "Vee" dipole modes or dipole modes which are not linear. Vee dipole modes would be necessary in a more complex antenna structure than the dipole now under consideration. Thus, what must be found with the aid of GTD is the field scattered from the cylinder at points along the receiving segment resulting from the test current on the source segment.

To find $\bar{E}^s(\ell)$ using a GTD format would require breaking $\bar{E}^s(\ell)$ into three basic components as sketched in Figure 10. $\bar{E}^s(\ell)$ contains a reflected component originating from the source segment and reflecting directly to the receiving or observation segment. $\bar{E}^s(\ell)$ also contains edge-diffracted components originating from the source segment and diffracting off the cylinder ends. Finally $\bar{E}^s(\ell)$ contains a creeping wave contribution coming from the source segment, attaching to the cylinder, then propagating around the cylinder as a surface wave and finally shedding to the observation segment. Other components (such as from the source to an edge diffraction, to surface wave to another edge diffraction, to the observation segment) are possible but these contributions would be minute and are justifiably neglected.

For the particular geometry under consideration, two assumptions are made. The cylinder is assumed to be electrically long so that diffraction from the ends is negligible, and the circular cylinder is assumed to have a large electrical diameter so that the creeping wave contribution is minute and may be ignored. These assumptions are made to simplify the problem used to describe and explain the hybrid technique and are not restrictions on solvable geometries. For the case in study, the dominant contribution to the scattered field $\bar{E}^s(\ell)$ is the reflected field $\bar{E}^r(\ell)$. The problem has been reduced to one of finding the reflected field $\bar{E}^r(\ell)$ at observation points on the receiving segment given an incident field from the source segment. To find this reflected field, GTD, (or in this case GO), is applied.
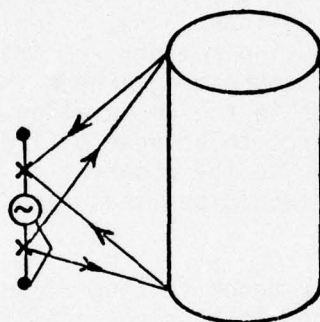
Referring to Section B of Chapter II, the GO field at an observation point (as shown in Figure 5) is

$$\bar{E}^r(s) = \bar{E}^i(Q_R) \cdot \bar{R} \sqrt{\frac{\rho_1^r \rho_2^r}{(\rho_1^r+s)(\rho_2^r+s)}}\ e^{-jks} \tag{54}$$

25
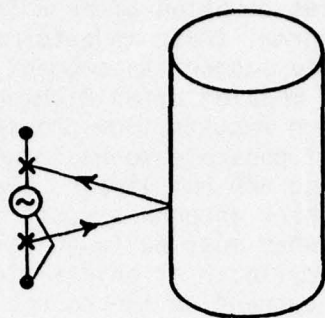
REFLECTION

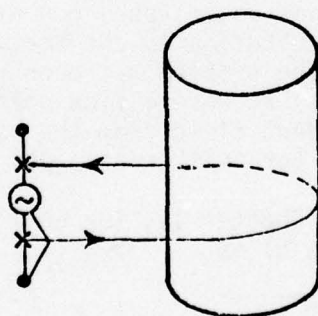**EDGE DIFFRACTION**

CREEPING WAVE

Figure 10. Scattering mechanisms for dipole interaction
with cylinder.

26

where $\overline{E}^i(Q_R)$ is the field incident at the reflection Q_R generated by the test current on the source segment where $\overline{\overline{R}}$ is the dyadic reflection coefficient

$$\overline{\overline{R}} = \hat{e}_\parallel^i \, \hat{e}_\parallel^r - \hat{e}_\perp \, \hat{e}_\perp = \begin{bmatrix} 1 & 0 \\ 0 & -1 \end{bmatrix} \cdot \tag{55}$$

$\rho_{1,2}^r$ are defined in Equation (23). The field $\overline{E}^i(Q_R)$ is known exactly for a monopole segment with a piecewise sinusoidal current distribution. This field will be considered in detail in the next section. The reflection point Q_R is found by applying the technique described in Section B of Chapter II. In applying Equation (54) two important points warrant special attention. First, to find Q_R on the cylinder, a source and observation point must be specified. The observation point presents no problem. In finding the segment-to-segment impedance terms a numerical integration is performed over the observation segment. The observation segment is divided into a specified number of integration sampling points which also serve as observation points. Specification of the source point, however, poses a problem. The source of $\overline{E}^i(Q_R)$ is actually distributed over the source segment, so an assumption must be made that the source appears to radiate from one specific point located on the source segment. This assumption allows the location of Q_R to be determined. The next section discusses the actual choice of the source point location and the ramifications of this choice.

The second important point for consideration involves the ray optical nature of GTD or GO. The field $\overline{E}^i(Q_R)$ is known at the reflection point Q_R, but in finding $\overline{E}^r(\ell)$ only the components of $\overline{E}^i(Q_R)$ which are perpendicular ($\perp$) to the incident ray path $\hat{I}$ are used as seen in Equation (54). GTD does not provide a method of including components of the field along the ray path. The assumption that must be made, then, is that the ray path component of $\overline{E}^i(Q_R)$ is negligible. That this assumption is fairly accurate until the dipole gets very close to the cylinder is demonstrated by the results presented in the next section.

Once $\overline{E}^r(\ell)$ is known, it is dotted with $I(\ell)\overline{d\ell}$ on the observation or receiving segment. The segment-to-segment impedance terms are found by carrying out the integration indicated in Equation (53) numerically. These terms are combined to get the ΔZ mode-to-mode impedance terms, thus forming the $[\Delta Z]$ matrix. This matrix, representing the cylinder effects, is added to $[Z]$ to form $[Z']$ the modified impedance matrix which is solved in the normal moment method manner. The matrix is inverted and multiplied by the voltage source column giving the desired current distribution. The input impedance of the dipole is found using the method described by Equation (52).

27

B.   Combining GTD With Thin-Wire Theory

The hybrid technique as described in the previous section is applied to the problem shown in Figure 9 and the solution of the problem is discussed here. The input impedance of the half-wave dipole, axially oriented at a distance D from a perfectly conducting circular cylinder of radius A, is calculated. The real and imaginary parts of the impedance are determined as a function of dipole distance D from the cylinder and are stored for plotting. The accuracy of this method is checked by comparing the plot obtained by this procedure with that obtained by an independent method.

The independent method is a solution by Ersoy and Wang [11]. The method consists of finding the solution of an axial dipole near an infinitely long, perfectly conducting circular cylinder.   This is accomplished by a technique very similar to the hybrid technique described in this paper. A delta impedance matrix representing the cylinder effects is found via a moment method procedure. The method incorporates the cylindrical Green's function in the kernel of the integral equation. These eigenfunctions account for the cylinder. To avoid the confusion of distinguishing between two hybrid type techniques, this method will be called the "MM-eigenfunction" technique.

The MM-eigenfunction solution is obtained in the form of a summation, and accurate results are obtained when sufficient terms are included. The MM-eigenfunction solution is taken to be the correct (exact) one. Figures 11a and b show the plots for the case $A=\lambda/2$ and D is varied from near zero to one wavelength. The agreement between the hybrid solution and the MM-eigenfunction solution is good until the dipole is less than 0.2λ from the cylinder. The input impedance of the half-wave dipole of diameter 0.0002λ in free space with one piece-wise sinusoidal mode is $73.22 + j\ 43.41\Omega$. The vertical scales of the plots are in ohms. The input impedance of the dipole is seen to be a damped sinusoid oscillating about the free space value as the dipole moves away from the cylinder. This is intuitively logical since the energy reflected from the cylinder to the dipole should alternately enhance and subtract from that of the free space dipole, thus modifying the dipole current distribution and giving the resulting input impedance plots.

Several other details of this problem should be discussed. The MM-eigenfunction solution used assumed an infinitely thin dipole whose current distribution was exactly $\cos kz$ in free space. Comparing this solution with the hybrid solution required that the hybrid dipole also have exactly the $\cos kz$ distribution. To accomplish this only one mode was used to model the $\lambda/2$ dipole. The piecewise sinusoidal current on this mode gave the desired $\cos kz$ distribution. This restriction of one mode to model the dipole was recognized as a detraction from the accuracy of the hybrid solution and provided the motivation for finding another independent check as described

28

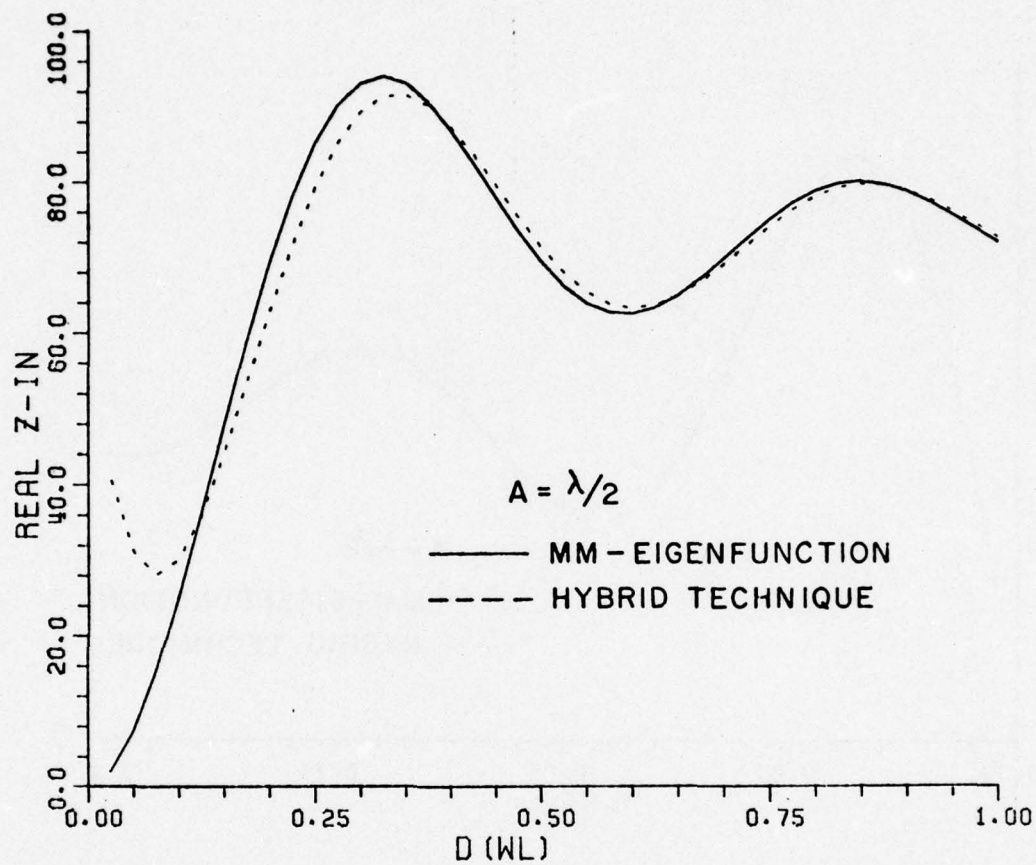Figure 11a. Real part of axial dipole input impedance
near cylinder of radius
A=0.5λ.

29
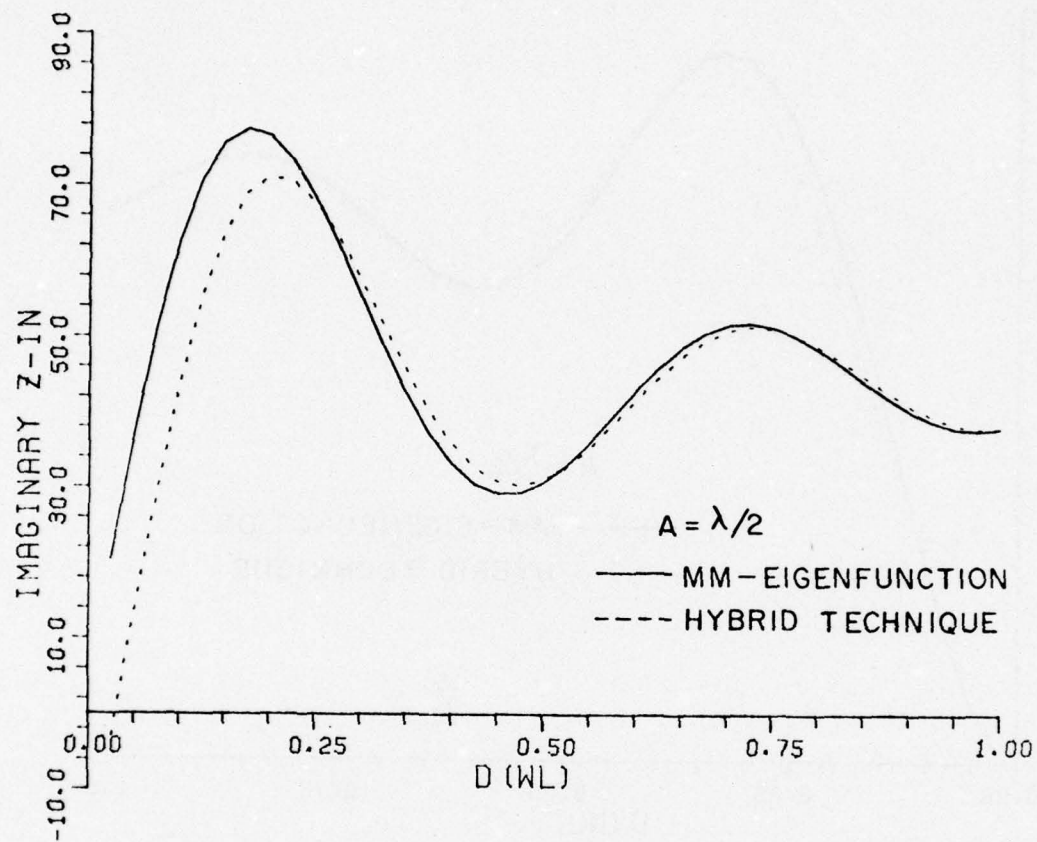
Figure 11b. Imaginary part of axial dipole input
impedance near cylinder of
radius A=0.5λ.

30

shortly. Also, for these results, both the MM-eigenfunction and hybrid solutions assumed an infinitely long cylinder. The hybrid technique accomplished this by simply not including any edge diffraction.

Another important detail, as pointed out in the previous section, was the selection of a single source point on the source segment. Its location was needed to find the field scattered from the cylinder in the segment-to-segment impedance term calculations. A logical choice, and the one used here to find the curves of Figures 11a and b, was the center of the source segment.

Three reasons were postulated for the breakdown of the hybrid solution when the dipole was closer than 0.2λ to the cylinder. The first, already mentioned, was that more modes might be required for better accuracy. That is, segments shorter than 0.25λ could be used to model the dipole. The second reason was that the approximation that the source emanates from the center of the segment became less accurate as the dipole approached the cylinder. The third reason was that the ray path component of $\overline{E}^i(Q_R)$ which GO ignores increased as the dipole approached the cylinder. All three of these situations would be improved if the dipole was divided into shorter segments. By doing this, the ability to compare the results of the hybrid solution with those of the MM-eigenfunction solution is lost since the MM-eigenfunction solution requires only one mode.

Another independent method of calculation was formulated using ground plane image theory. Richmond's thin-wires over an infinite ground plane computer code [12] was the method used. Consider a horizontal half wave dipole at a distance D above a perfectly conducting infinite ground plane. This geometry is similar to that of the dipole near the infinitely long cylinder of radius A as A gets very large. So the hybrid technique may be compared with ground plane image theory if a large enough radius is chosen. In fact, since the differences to be compared are small, it is advantageous to eliminate the approximation of large enough A as follows: The radius of the cylinder appears in the calculation of the reflection point Q_R and in the reflected field $\overline{E}^r(Q_R)$ of the GO expression, Equation (54). The reflection point calculation does not need modification for this particular geometry since it will be independent of the radius A. In the spread factor part of Equation (54), ρ_1^r and ρ_2^r are the principal radii of curvature of the reflected wavefront at the reflection point Q_R. They are given by Equation (23) for a spherical wavefront incident and repeated here as

31

$$\frac{1}{\rho_{1,2}^r} = \frac{1}{s^r} + \frac{1}{\cos\theta^i}\left[\frac{\sin^2\theta_2}{R_1} + \frac{\sin^2\theta_1}{R_2}\right]$$

$$\pm \sqrt{\frac{1}{\cos^2\theta^i}\left[\frac{\sin^2\theta_2}{R_1} + \frac{\sin^2\theta_1}{R_2}\right]^2 - \frac{4}{R_1 R_2}} \quad . \tag{56}$$

For a cylinder, $R_2 = \infty$ and Equation (56) reduces to

$$\frac{1}{\rho_{1,2}^r} = \frac{1}{s^r} + \frac{1}{\cos\theta^i}\left(\frac{\sin^2\theta_2}{R_1}\right) \pm \left(\frac{1}{\cos\theta^i}\right)\left(\frac{\sin^2\theta_2}{R_1}\right) \quad . \tag{57}$$

The cylinder radius is $R_1=A$. As the cylinder radius approaches infinity, $R_1 \to \infty$, it becomes an infinite ground plane and Equation (57) becomes

$$\frac{1}{\rho_{1,2}^r} = \frac{1}{s^r} \quad . \tag{58}$$

Using this in the hybrid program is equivalent to $A=\infty$. Figure 12 shows the geometry of this problem.

The ground plane image theory solution places no restriction on the number of modes; modes were increased to three and input impedance plots were again determined. As illustrated in Figure 12 the segment length is d and the source point location on the segment is indicated by x_0. For the particular case that was run $x_0=0.5d$. Since the focus was on input impedance when the dipole was close to the cylinder, D varied from near zero to only $\lambda/2$. The real and imaginary components of the input impedance were calculated by the two methods and the resulting curves plotted as Figures 13a and b. The ground plane image theory was considered correct and is indicated by the solid curve while the hybrid solution is indicated by the dotted curve.

These curves demonstrated that the postulated improvement in hybrid theory accuracy for an increased number of modes did not materialize. This was explained partly by the fact that although the segments were smaller and therefore the errors introduced due to the previously discussed approximations were smaller, they added up to about the same error when combined to include the entire dipole. To

32
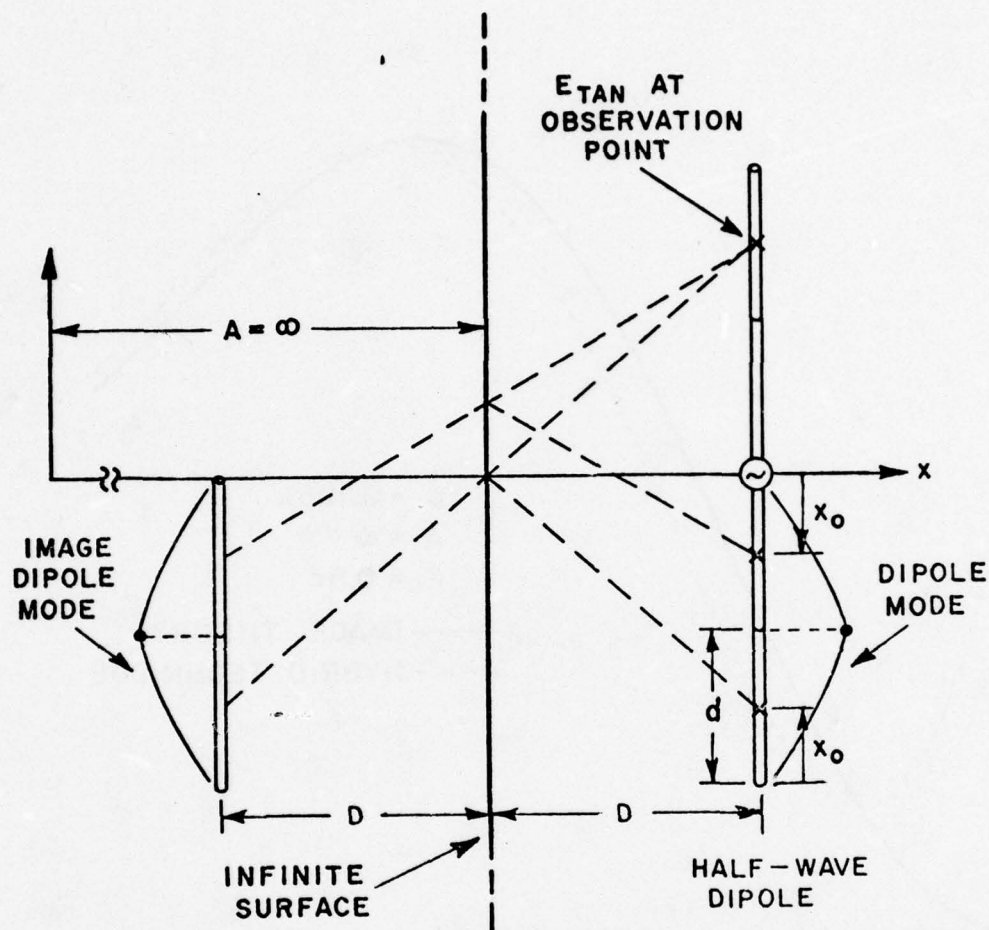
Figure 12. Geometry of dipole near cylinder of radius A=∞ showing source point location and image dipole mode.

33
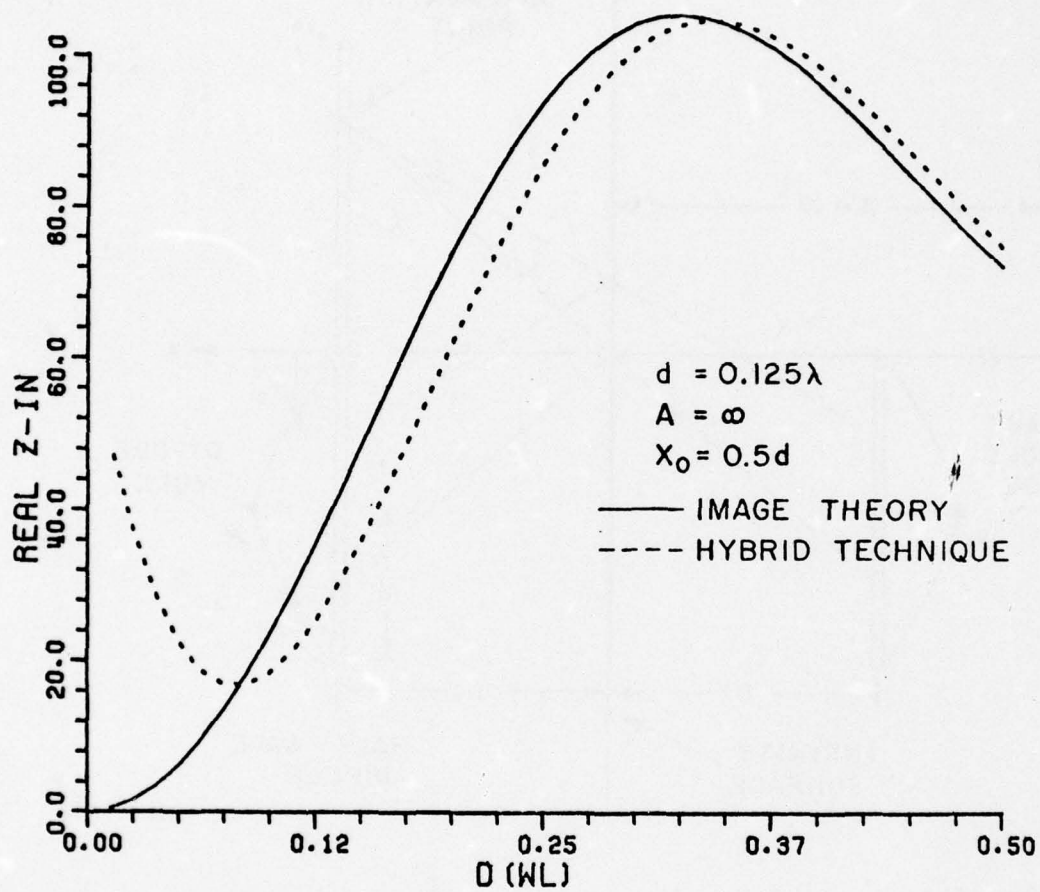
Figure 13a. Real part of axial dipole input impedance
near cylinder of radius A=∞.

34
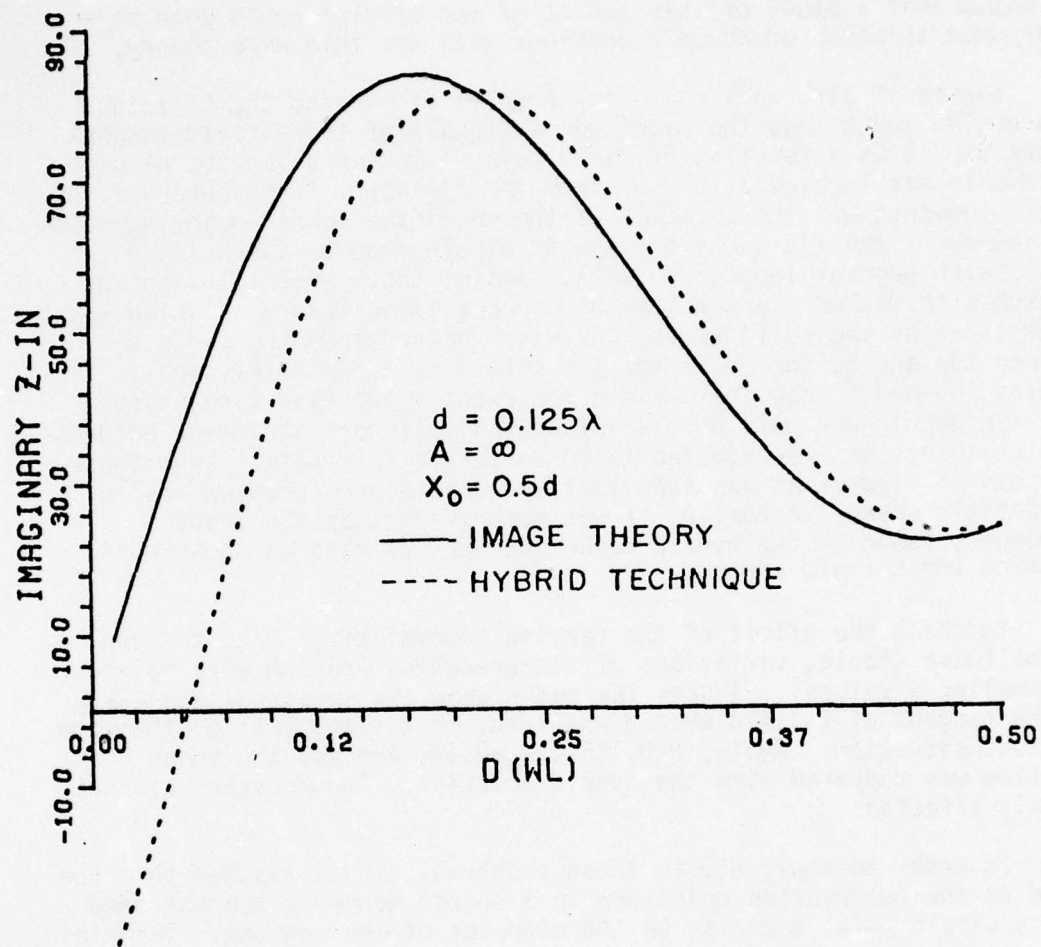
Figure 13b. Imaginary part of axial dipole input impedance
near cylinder of radius A=∞.

investigate the effects of the GTD approximations, the reflected field along the dipole was studied. Specifically the component tangent to the dipole, the one employed when integrating to determine the mutual impedance terms, was calculated over the length of the dipole L. It was hoped that a study of this aspect of the problem would lead to a clear understanding of how GTD combines with the thin wire theory.

Figure 12 also applies to the problem of finding the E-field. Figures 14a and b show the magnitude and phase of the E-field tangent to the dipole as a function of field point location along the dipole. The dipole was located at $D=0.5\lambda$ from the cylinder. The center of the source segments was the location of the specified source point $x_0=0.5d$. The source of the field was the lowest dipole mode on the halfwave dipole with segment length $d=0.125\lambda$. Again, the hybrid solution was plotted with dashed lines while the correct image theory solution was represented by the solid curve. As was expected from the plots on Figures 13a and b, for $D=.5\lambda$ the two solutions agree fairly well. Figures 15a and b show the E-field for exactly the same case except that the dipole was only $D=0.125\lambda$ from the cylinder; agreement between the two solutions was expected to be worse for this case. From these two sets of figures it was seen that the most severe problem was in the E-field phase. Actually, it was surprising that the input impedances found by the hybrid technique were as good as shown considering the E-field errors.

To check the effect of the varying segment sizes used to model the halfwave dipole, variations of the preceding problem were solved for smaller d values. Figures 16a and b show the magnitude and phase of the tangential E-field when d was $\lambda/40$, or 5 times smaller than the previous situation. Again, $D=0.125\lambda$, $x_0=0.5d$, $A=\infty$ and the image solution was compared with the hybrid solution. The accuracy was not greatly affected.

In order to apply GTD to these problems, it was assumed that the field at the observation point due to a source monopole segment came from a single point taken to be the midpoint of the segment. The field was actually generated from current distributed over the source segment. Since the current on the monopole segment was not symmetric about the selected center point, it seemed reasonable that a more accurate source point could be chosen. Several alternative source points were tried, a logical choice was the point of equal moments. Figure 17 shows a piecewise sinusoidal distribution $\sin \beta x$ on a monopole segment of length d. Equating first moments gave the following equation

$$\int_0^{x_m} (x_m - x)\sin \beta x \, dx = \int_{x_m}^d (x - x_m)\sin \beta x \, dx. \qquad (59)$$

36
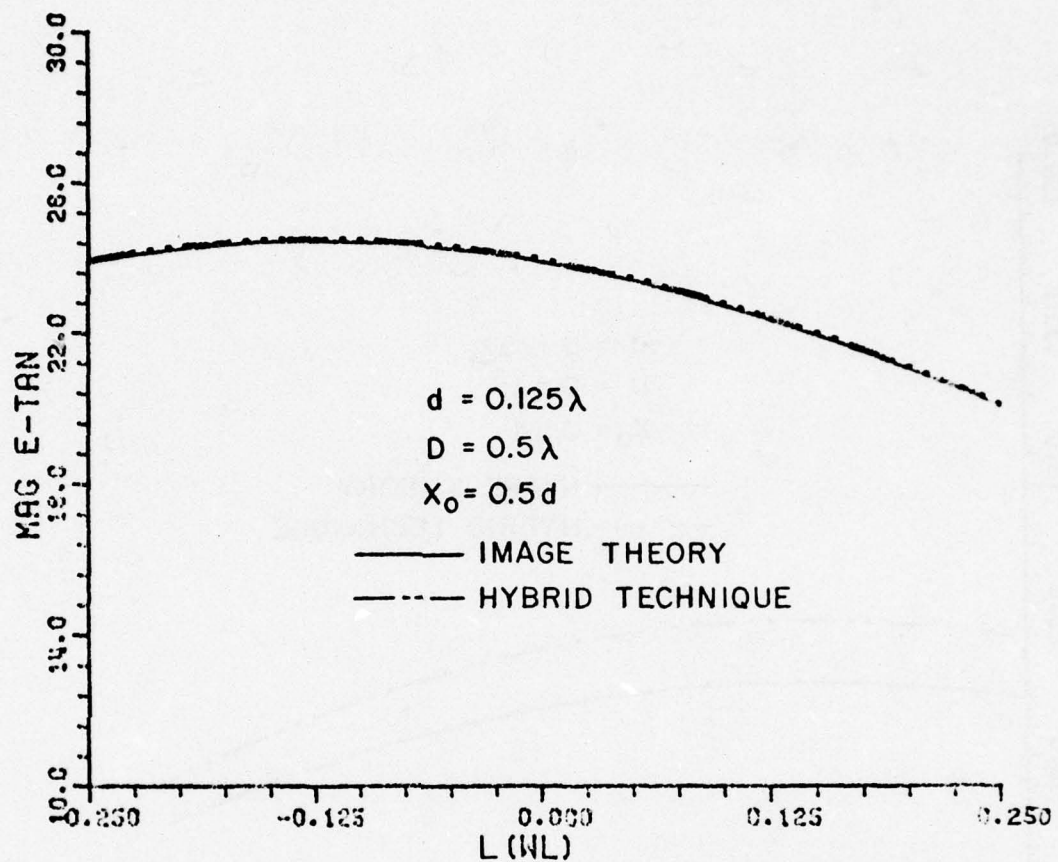
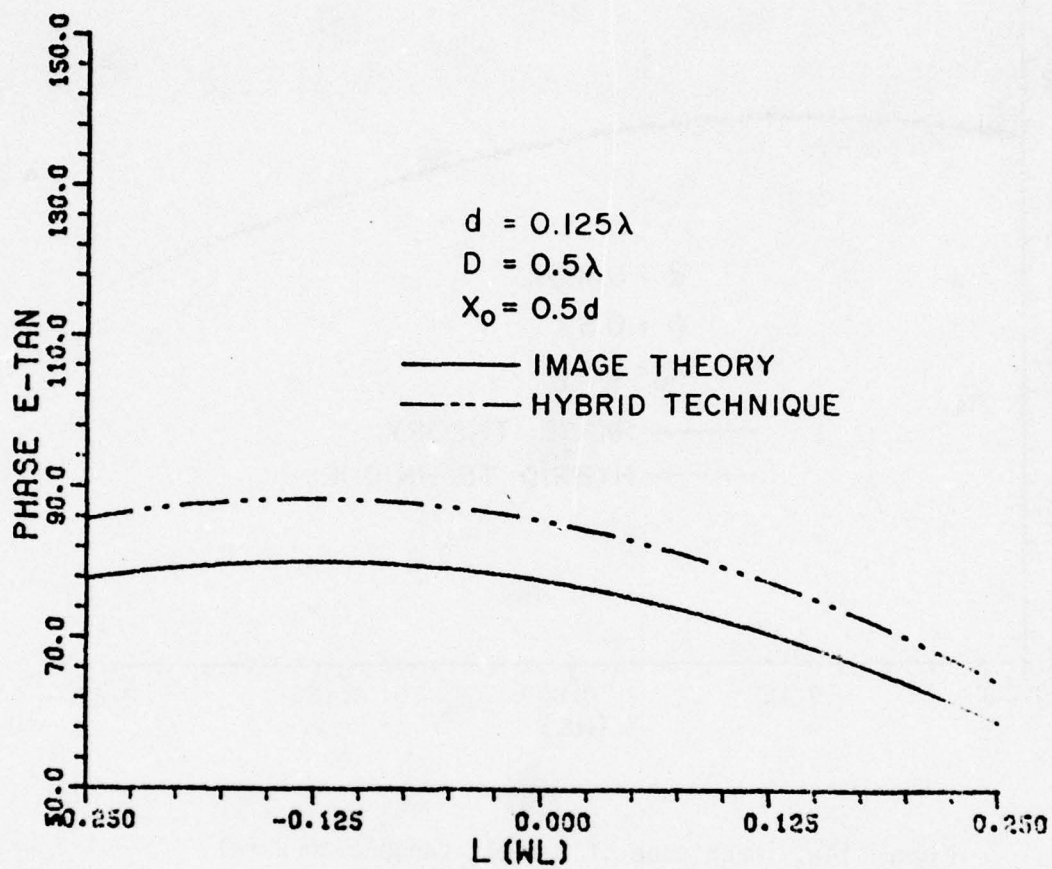Figure 14a. Magnitude of E-field tangent to axial dipole along its length.

Graph axis label: MAG E-TAN

Y-axis values: 30.0, 26.0, 22.0, 18.0, 14.0, 10.0

X-axis label: L(WL)

X-axis values: -0.250, -0.125, 0.000, 0.125, 0.250

$d = 0.125\lambda$
$D = 0.5\lambda$
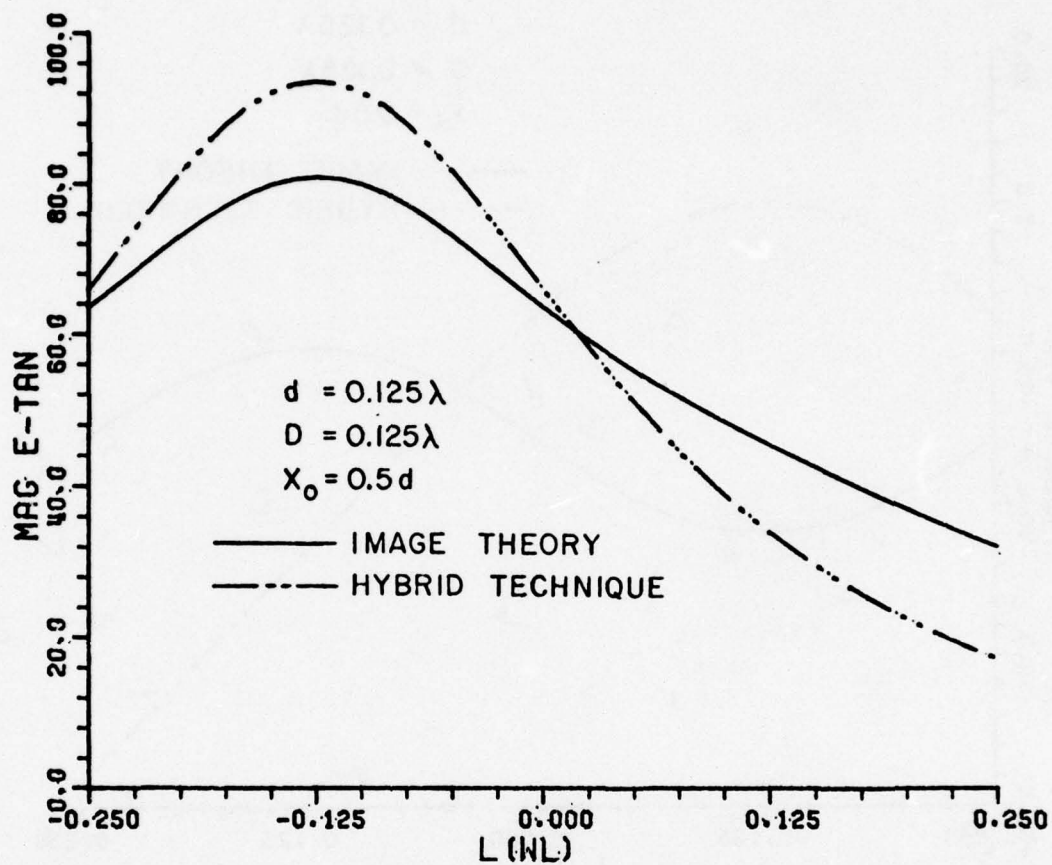$X_0 = 0.5d$

—— IMAGE THEORY
—·—·— HYBRID TECHNIQUE

37

Figure 14b. Phase of E-field tangent axial dipole along its length.

38

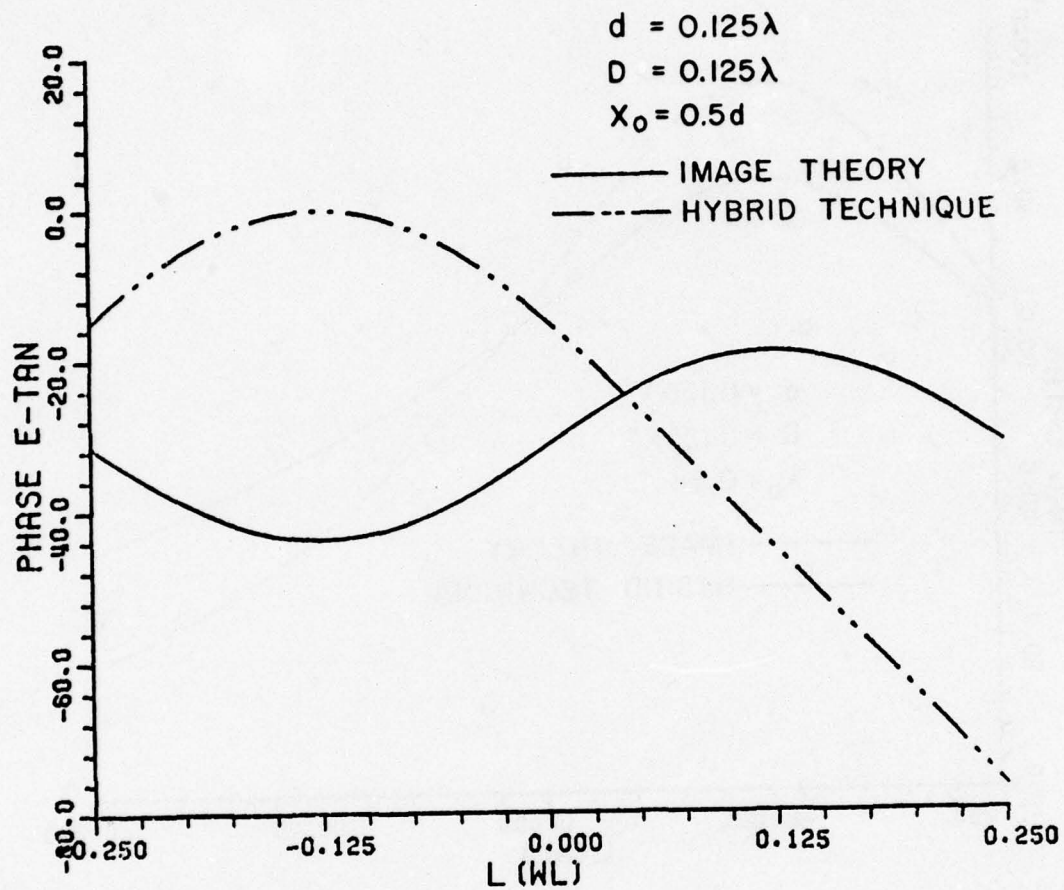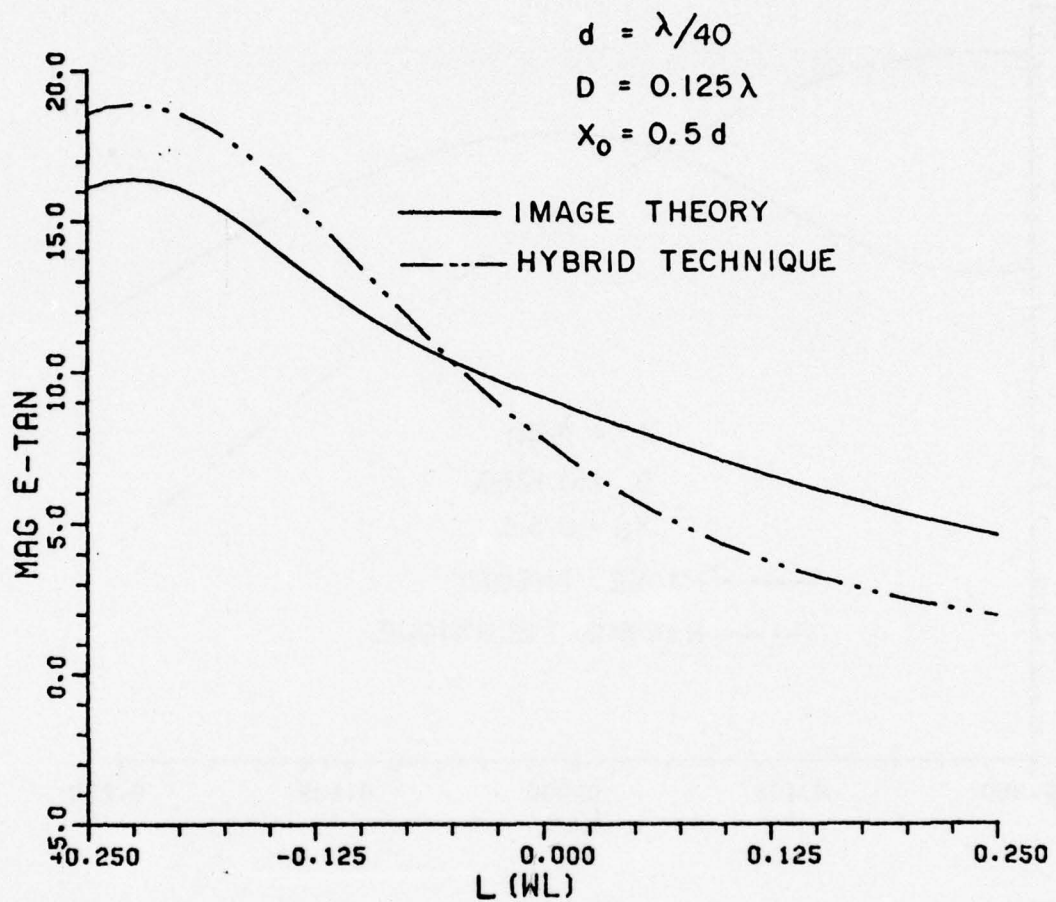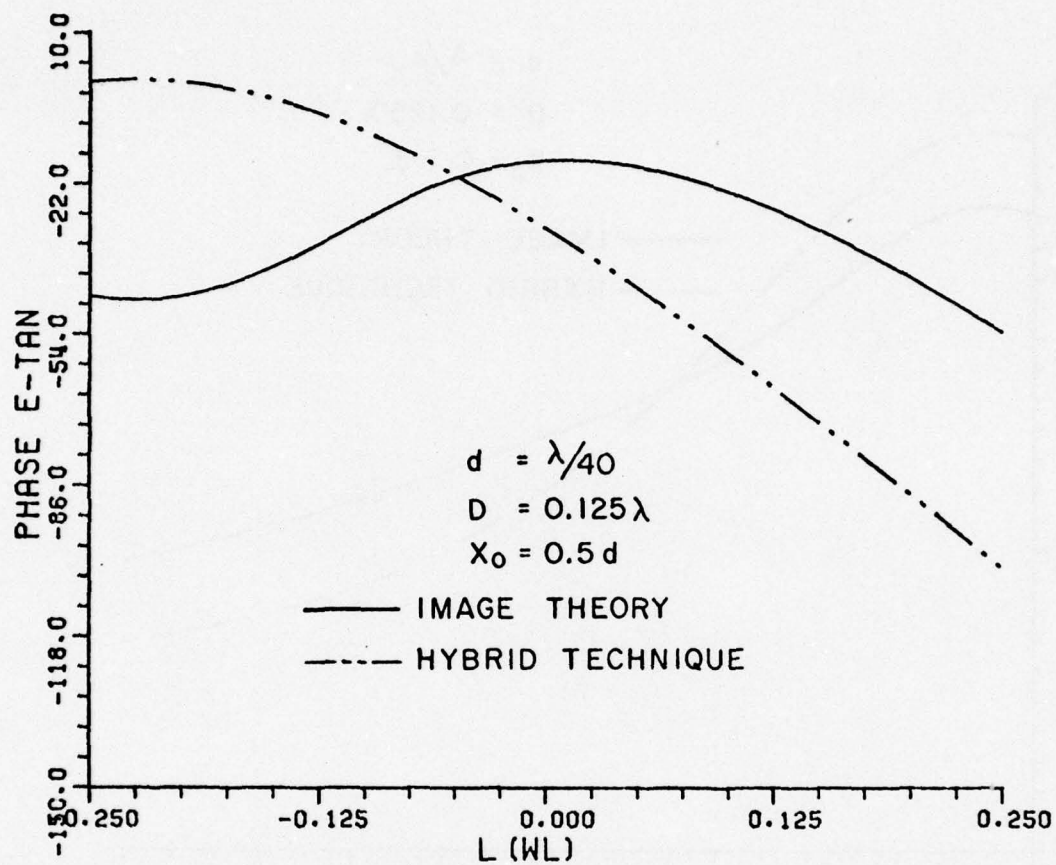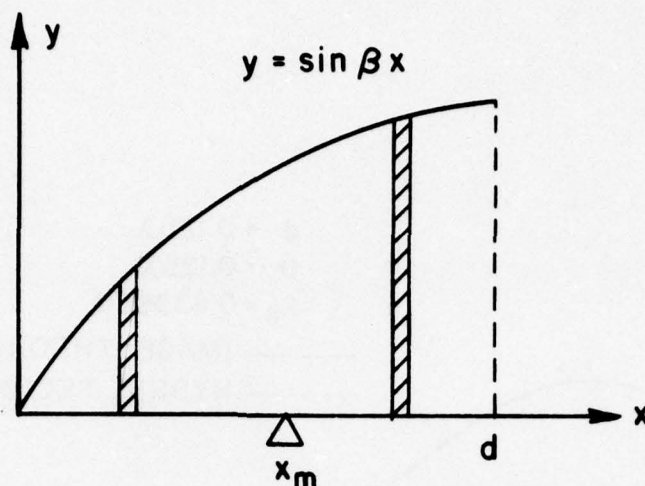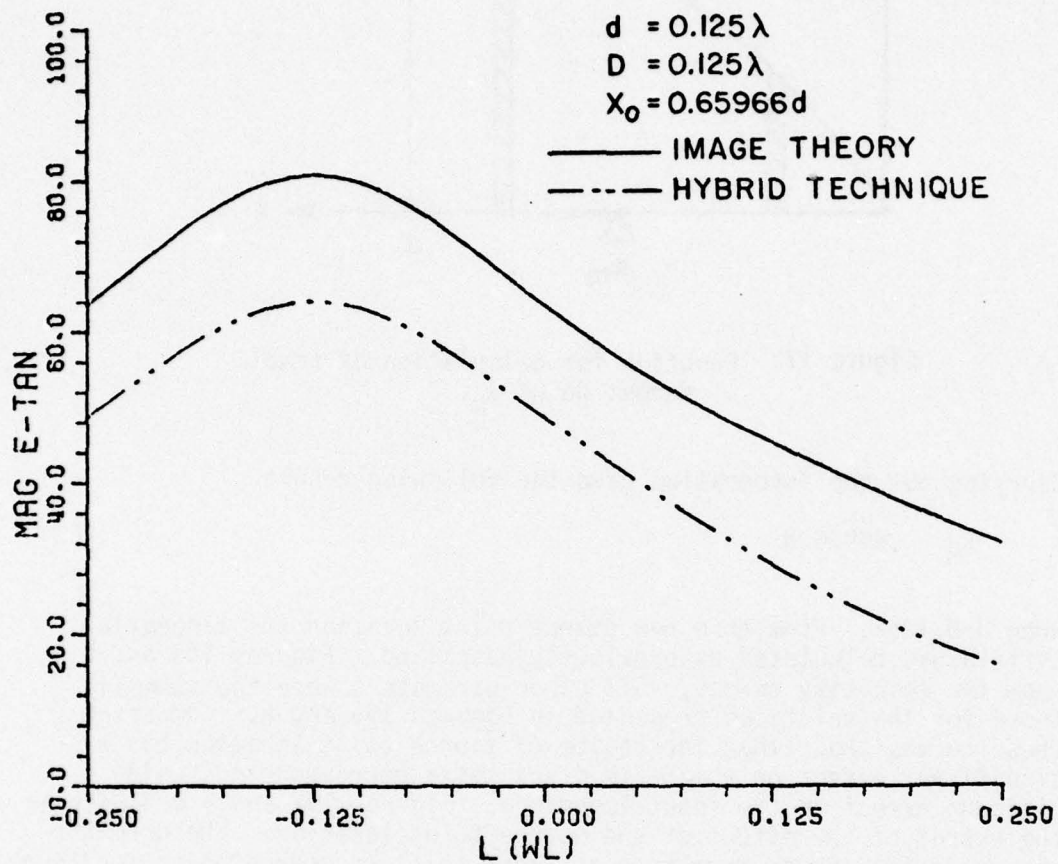Figure 15a. Magnitude of E-field tangent to axial dipole along its length.

39

Figure 15b. Phase of E-field tangent to axial
dipole along its length.

40

$d = \lambda/40$

$D = 0.125\lambda$

$X_0 = 0.5\,d$

———— IMAGE THEORY

—·—·— HYBRID TECHNIQUE

Figure 16a. Magnitude of E-field tangent to axial dipole along its length.

41

Figure 16b. Phase of E-field tangent to axial
dipole along its length.

Figure 17. Function for calculation of equal
moment point x_m.

Carrying out the integration gave the following result

$$x_m = .65966 \, d \tag{60}$$

when $d=0.125\lambda$. From this new source point location the tangential
E-field was calculated as previously described. Figures 18a and b
show the resulting curves. All other parameters were the same as
those for the solutions presented in Figures 15a and b. Comparing
these curves shows that the choice of source point location has a
significant effect on the E-field and has a correspondingly sig-
nificant effect on the input impedance. Figures 19a and b demonstrate
the extent of the effect of the source point location. The dramatic
change in the curves from such a slight shift in source point location
demonstrates the sensitivity of the hybrid solution to this parameter.
From this data it was concluded that an improved method for integrating
GTD with the moment method was essential if the desired accuracy was
to be obtained when the dipole was located close to the cylinder.

As mentioned previously, two important assumptions were made
in finding $\overline{E}^r(\ell)$ using the GO expression. To find Q_R a specific
source point was chosen even though the actual source was distributed
over the entire segment. $\overline{E}^i(Q_R)$ was the exact field at Q_R, but in
determining $\overline{E}^r(\ell)$ only the components of $\overline{E}^i(Q_R)$ which were perpen-
dicular and parallel to the incident ray path were used; the assumption
was that the ray path component of $\overline{E}^i(Q_R)$ was negligible. A careful
look at the exact near field expressions from a monopole segment with
a piecewise sinusoidal current distribution showed how making both of
these assumptions could be avoided.

43

Figure 18a. Magnitude of E-field tangent to axial
dipole along its length.
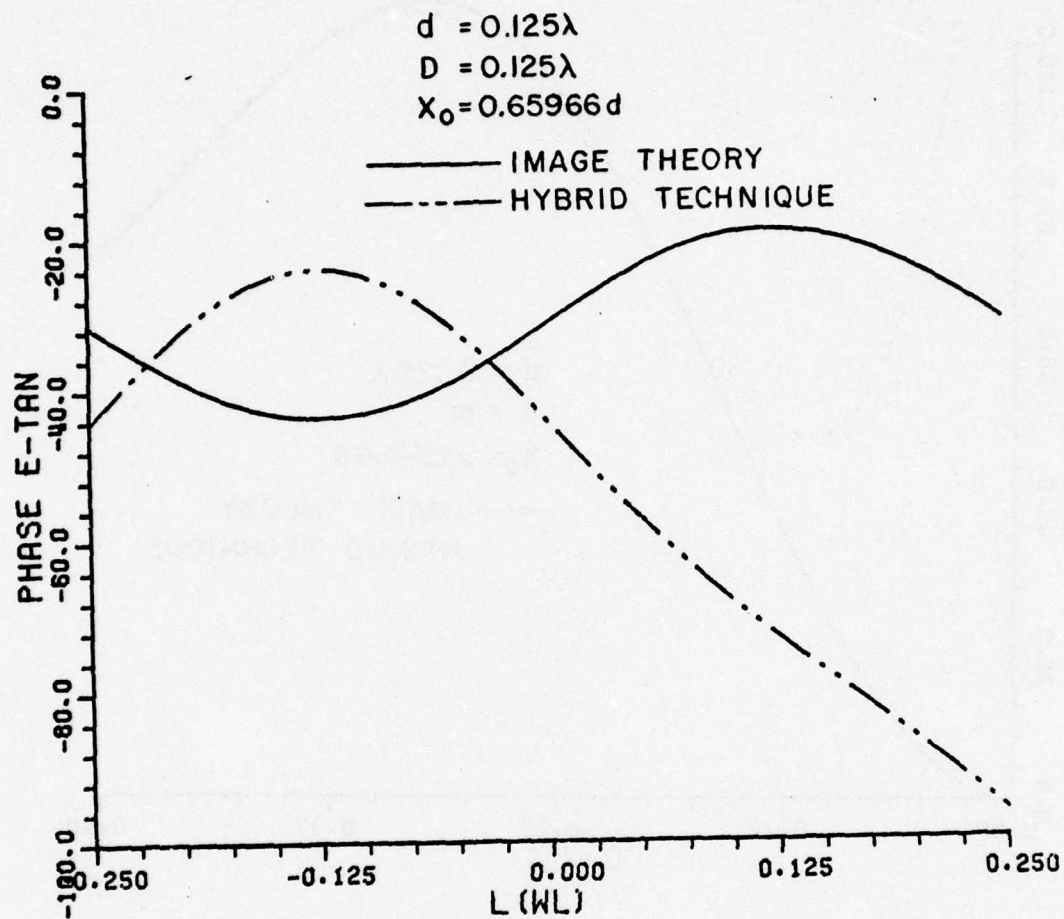
Figure 18b. Phase of E-field tangent to axial
dipole along its length.

45
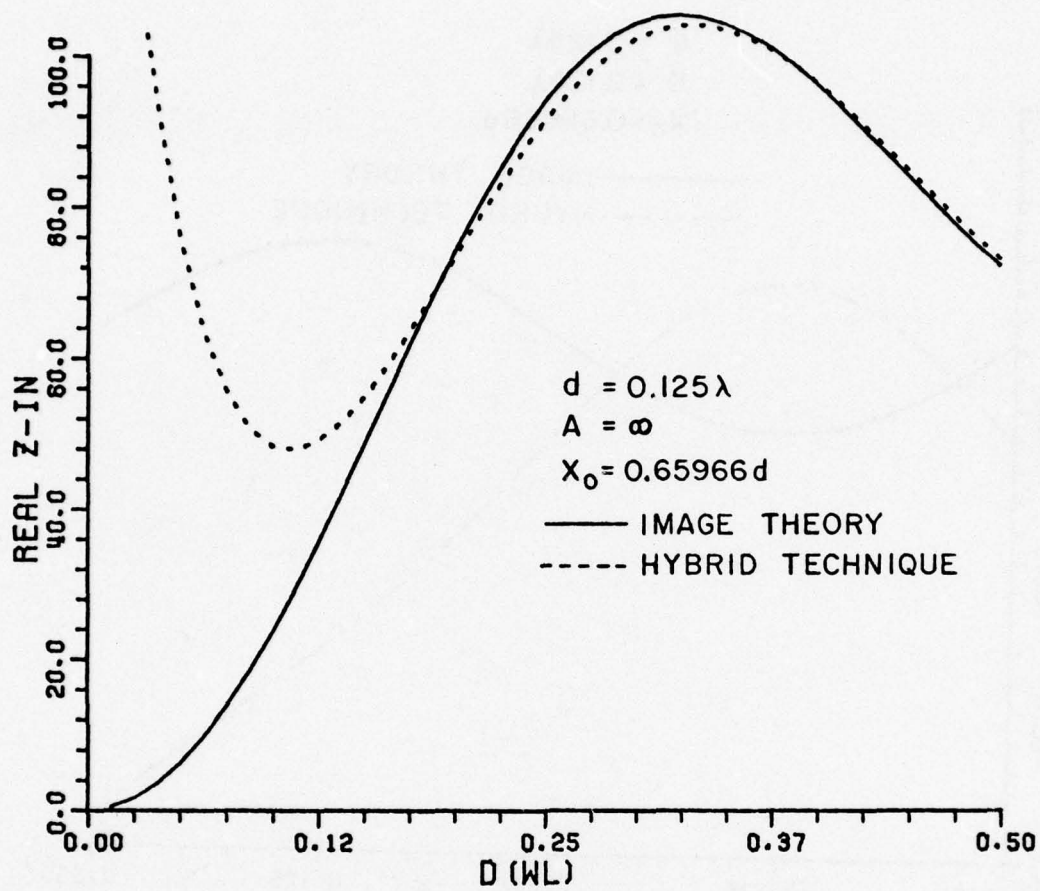
Figure 19a. Real part of axial dipole input impedance
near cylinder of radius A=∞.

46
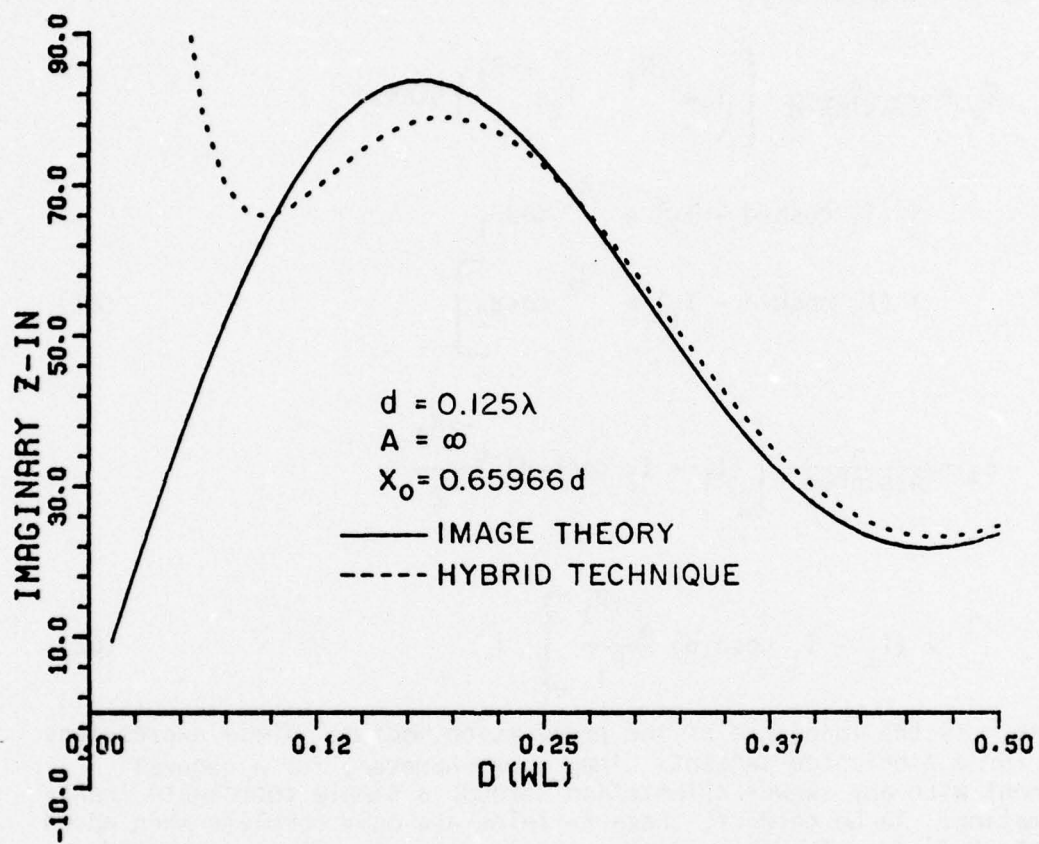
Figure 19b. Imaginary part of axial dipole input impedance
near cylinder of radius A=∞.

47

The fields radiated from the monopole segments are given by Richmond [2]. Figure 20 shows the z oriented monopole segment. The piecewise sinusoidal current distribution is

$$I(z) = \frac{I_1 \sinh\gamma(z_2-z) + I_2 \sinh\gamma(z-z_1)}{\sinh\gamma d} \tag{60}$$

where I_1 or I_2 is zero, γ is the complex propagation constant, d is the segment length, and $z_{1,2}$ are the endpoints. The resulting fields at any point (ρ,z) are

$$E_\rho = \frac{\eta}{4\pi\rho\sinh\gamma d} \left[\left(I_1 e^{-\gamma R_1} - I_2 e^{-\gamma R_2} \right) \sinh\gamma d \right.$$

$$+ (I_1 \cosh\gamma d - I_2) e^{-\gamma R_1} \cos\theta_1$$

$$\left. + (I_2 \cosh\gamma d - I_1) e^{-\gamma R_2} \cos\theta_2 \right] \tag{61}$$

and

$$E_z = \frac{\eta}{4\pi\sinh\gamma d} \left[(I_1 - I_2 \cosh\gamma d) \frac{e^{-\gamma R_2}}{R_2} \right.$$

$$\left. + (I_2 - I_1 \cosh\gamma d) \frac{e^{-\gamma R_1}}{R_1} \right] \tag{62}$$

where η is the impedance of the propagation medium. These expressions are for a z oriented segment. They work, however, for a general segment with any skewed orientation through a simple coordinate transformation. To be correct, these E-fields are only complete when added to the E-fields of a connecting monopole segment. These connected monopole segments make a dipole mode that is used in the thin-wire theory. The crucial fact to note about these E-fields is that they may be separated into fields emanating from the two endpoints. More-over, these separated field contributions have an $e^{-\gamma R}/R$ term multiplied by a pattern factor form, and are recognized as spherical waves emanating from the endpoints. These observations may be exploited with remarkable results to improve the integration of GTD with thin-wire theory. At the observation point on the dipole, the reflected field $\overline{E}^r(\ell)$ will now be the superposition of the contribution from one endpoint of the source segment plus the contribution from the other

48
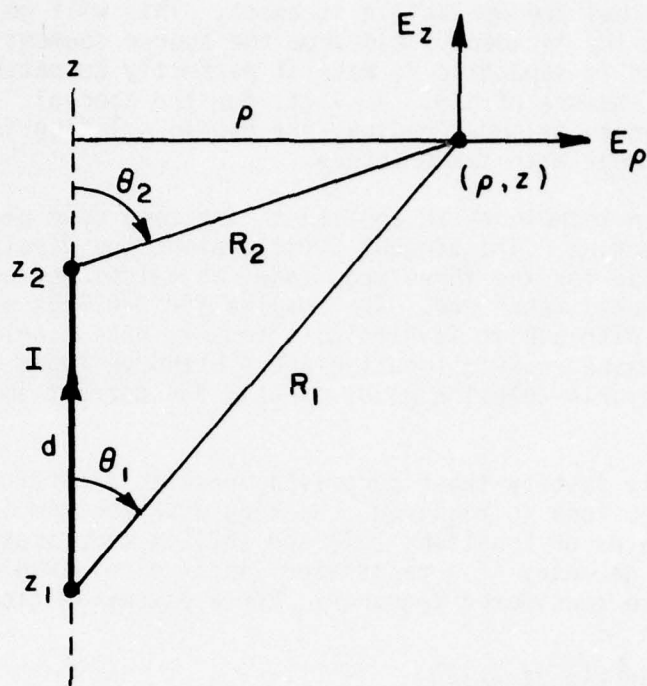
Figure 20.   z-directed monopole segment source with
the observation point (ρ,z).

49

endpoint. Each endpoint will have its own reflection point on the cylinder. By separating the fields in this way the distributed nature of the source has been properly accounted for. Less obvious is the fact that the ray path components of the separated fields are zero so that the assumption that they are negligible is exact. This will be demonstrated later. Thus the incident field from the source segment at the reflection points is separated to make it perfectly compatible with the ray optical nature of GTD. In fact, for the special geometry of the infinite cylinder radius, the hybrid solution is shown to be in exact agreement with image theory.

This separation technique was applied to the same case previously presented in this section. The tangent E-field along the dipole from the lowest dipole mode for the three mode case was calculated and plotted using the hybrid technique. The results for $D = 0.125\lambda$ are in Figures 21a and b. Although it is difficult to see, both a solid image theory curve and a dashed hybrid solution are plotted on those figures. For this case, the hybrid solution gives exactly the correct image theory solution.

To analytically justify these surprising results a careful look at the E-field expressions is required. Working with the combined monopole segment fields of Equations (61) and (62) is complicated. Figure 22 shows the geometry of a center-fed linear dipole where the monopole segments are considered together. For a piecewise sinusoidal current distribution

$$\overline{I}(z) = \frac{\hat{z}\, I_0 \, \sin[k(d-|z-z_2|)]}{\sin kd} \tag{63}$$

where $k = \omega\sqrt{\mu\epsilon}$,

Richmond [13] gives the following rigorous fields

$$E_\phi = 0 \tag{64}$$

$$E_\rho = \frac{j\eta\, I_0}{4\pi\rho\sin kd}\left[e^{-jkR_1} \cos\theta_1 \right.$$

$$\left. - 2\cos(kd)\, e^{-jkR_2} \cos\theta_2 + e^{-jkR_3} \cos\theta_3 \right] \tag{65}$$

$$E_z = -\frac{j\eta\, I_0}{4\pi\sin kd}\left[\frac{e^{-jkR_1}}{R_1} - 2\cos(kd)\frac{e^{-jkR_2}}{R_2} \right.$$

$$\left. + \frac{e^{-jkR_3}}{R_3} \right] \ . \tag{66}$$

50
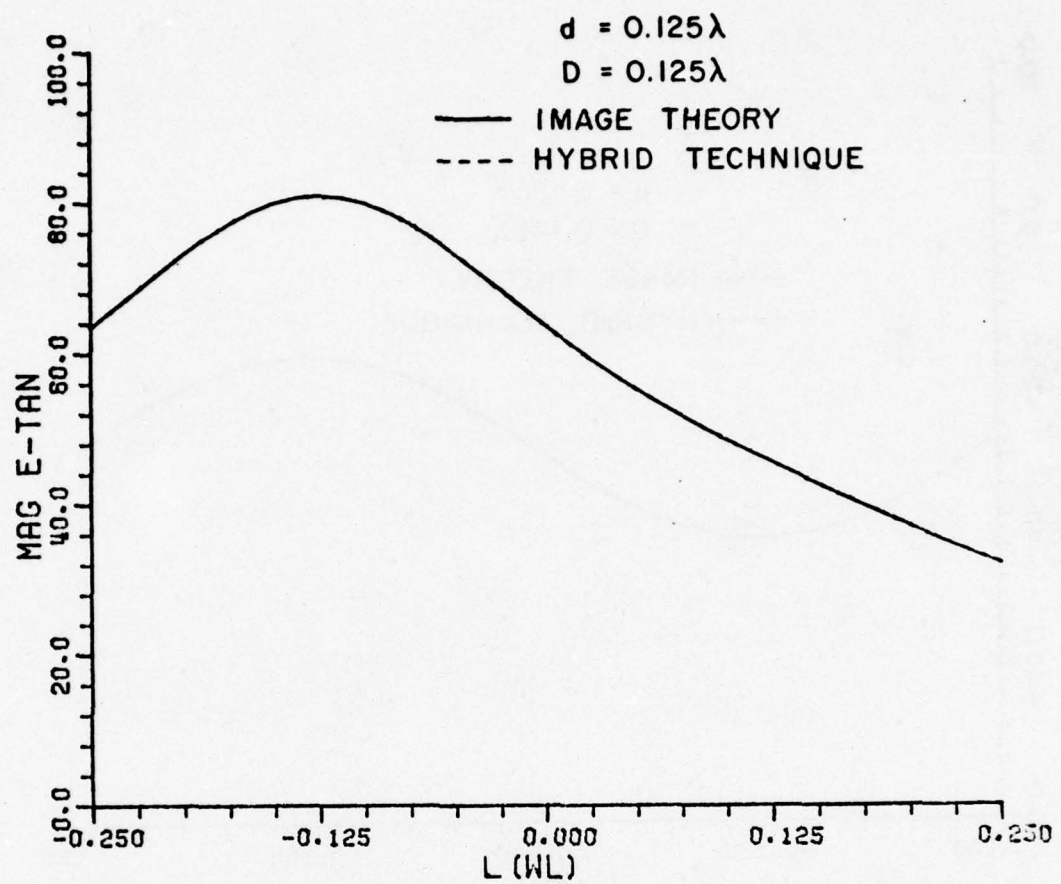
Figure 21a. Magnitude of E-field tangent to axial dipole along its length with endpoint separation.
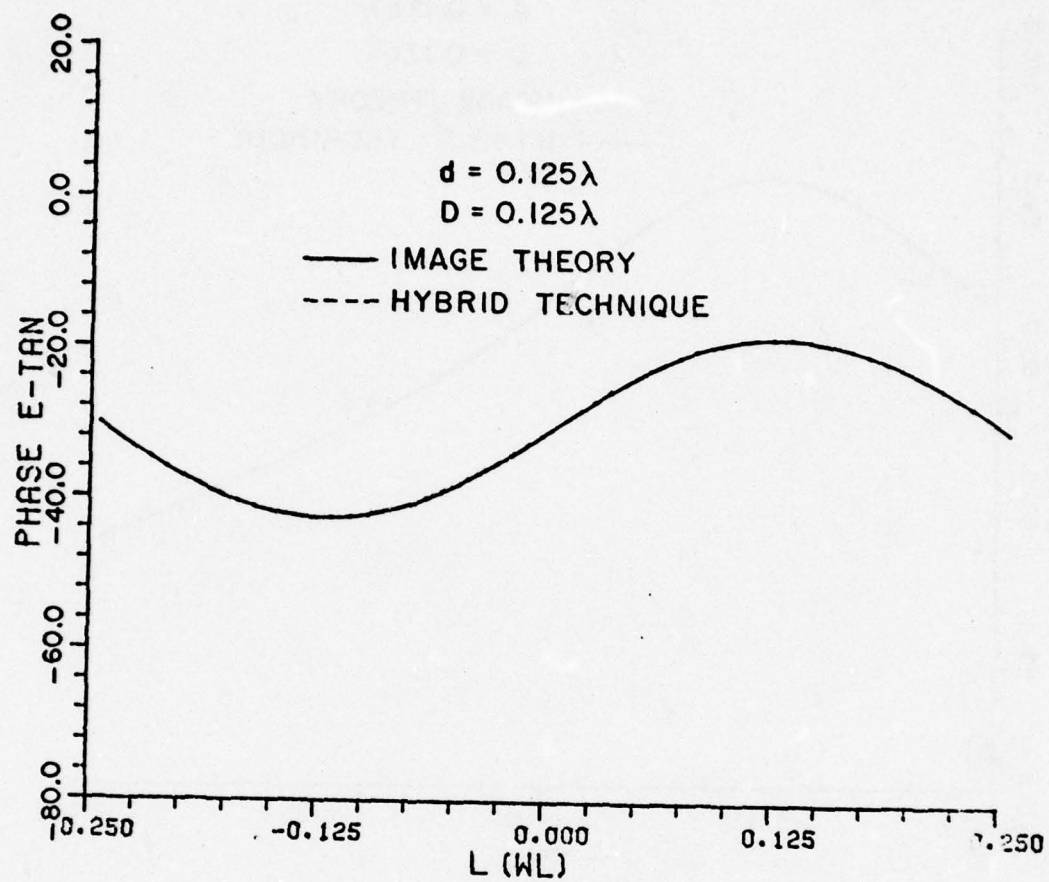
51

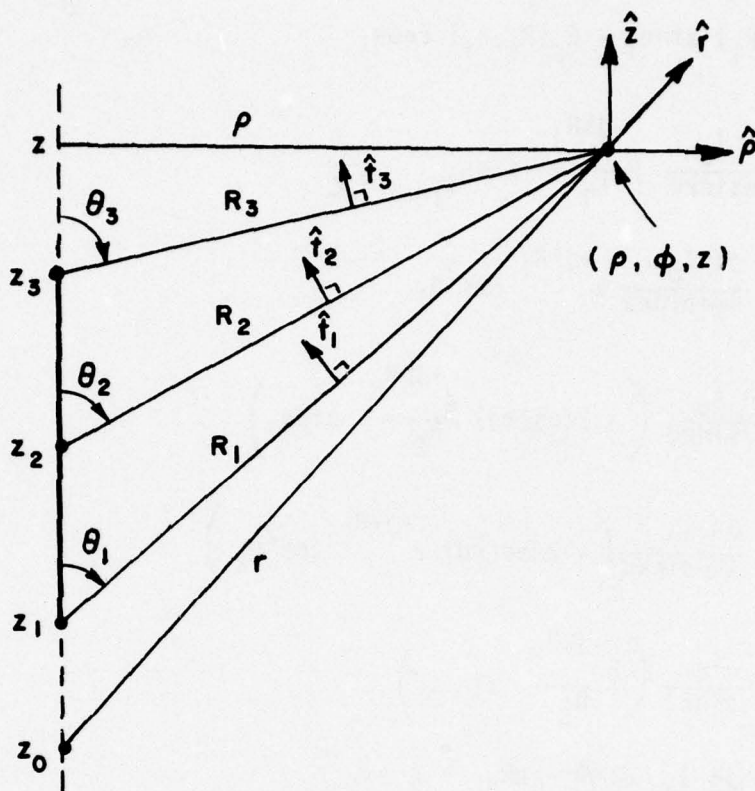Figure 21b. Phase of E-field tangent to axial dipole along its length with endpoint separation.

Figure 22. Z-directed center fed dipole source
with observation point (ρ, ϕ, z).

When fields from two connecting monopole segments are combined these expressions are derived directly from Equations (61) and (62). Again, the fields may be separated into contributing fields from z_1, z_2 and z_3. Justification of the separation technique as well as demonstration of zero ray path contribution can be shown by proving the following hypothesis:

$$\vec{E}(\rho, Z) = E_\rho \, \hat{\rho} + E_z \, \hat{z} \stackrel{?}{=} E_1\hat{t}_1 + E_2\hat{t}_2 + E_3\hat{t}_3 . \qquad (67)$$

That is, the total field at the observation point is postulated to be the superposition of contributions from the two endpoints and the feed point. In addition the total field is said to be contained in components which are only transverse to the ray paths. In Equation (67) E_ρ and E_z are the known total fields given by Equations (65)

53

and (66). Let E_i be the contribution from point i transverse to ray path i (i=1,2,3). From the geometry in Figure 22 after some trigonometry

$$E_i = E_z(R_i) \sin\theta_i - E_\rho(R_i,\theta_i) \cos\theta_i \quad . \tag{68}$$

Specifically,

$$E_1 = \frac{-j\eta I_o}{4\pi \sin kd} \frac{e^{-jkR_1}}{R_1} \sin\theta_1$$

$$-\frac{j\eta I_o}{4\pi\rho \sin kd} e^{-jkR_1} \cos^2\theta_1 \tag{69}$$

$$E_2 = -\frac{j\eta I_o}{4\pi \sin kd}\left(-2\cos(kd)\frac{e^{-jkR_2}}{R_2} \sin\theta_2 \right)$$

$$-\frac{j\eta I_o}{4\pi\rho \sin kd}\left(-2\cos(kd) e^{-jkR_2} \cos^2\theta_2 \right) \tag{70}$$

$$E_3 = -\frac{j\eta I_o}{4\pi \sin kd}\left(\frac{e^{-jkR_3}}{R_3} \sin\theta_3 \right)$$

$$-\frac{j\eta I_o}{4\pi\rho \sin kd}\left(e^{-jkR_3} \cos^2\theta_3 \right) \quad . \tag{71}$$

To verify Equation (67), E_1, E_2, and E_3 should give the total field E_z and E_ρ. Using geometry again

$$E_z = E_1 \sin\theta_1 + E_2 \sin\theta_2 + E_3 \sin\theta_3. \tag{72}$$

Also using $\rho = R_1\sin\theta_1 = R_2\sin\theta_2 = R_3\sin\theta_3$ in E_1, E_2, and E_3 and the trigonometric relationship $\sin^2\theta + \cos^2\theta = 1$, Equation (72) can be shown to be equal to Equation (66). Similarly

$$E_\rho = -E_1\cos\theta_1 - E_2\cos\theta_2 - E_3\cos\theta_3 \tag{73}$$

is equal to Equation (65). Thus Equation (67) is verified and the hypothesis is proved demonstrating analytically the exact agreement between the hybrid technique and image theory.

54

To relate this tangential E-field result back to the input
impedance calculation, the case of a half-wave dipole near the infinite
ground plane was run with the endpoint separation technique incorporated
into the hybrid technique. The real and imaginary parts of the input
impedance were plotted versus dipole distance from the cylinder in
Figures 23a and b. The agreement between the image and hybrid solution
was nearly exact, which is a very significant improvement.

The hybrid technique has been described in detail. A method
for combining GTD with thin-wire theory has been demonstrated which
integrates the two so that the necessary GTD assumptions do not
hinder the results. In the next chapter the case where wire antennas
are near a curved surface will be examined.

55
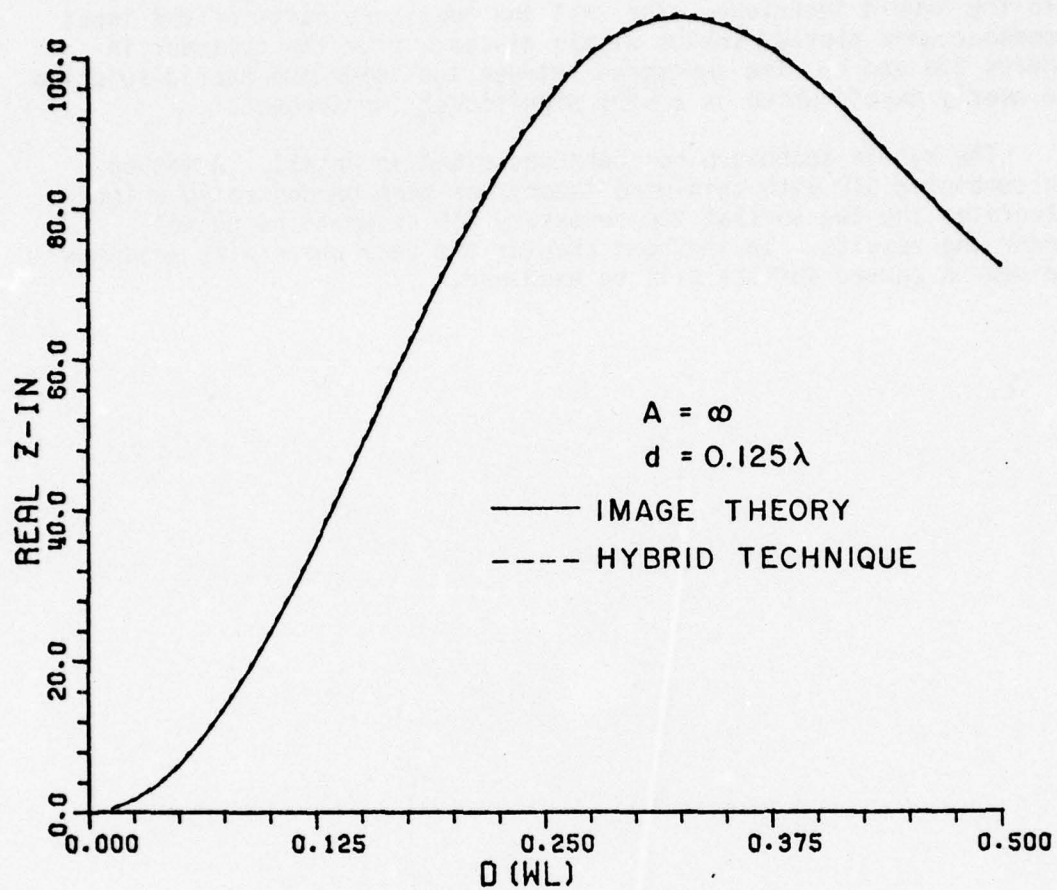
Figure 23a. Real part of axial dipole input impedance near cylinder of radius A=∞.

A = ∞
d = 0.125λ

——— IMAGE THEORY
- - - - HYBRID TECHNIQUE
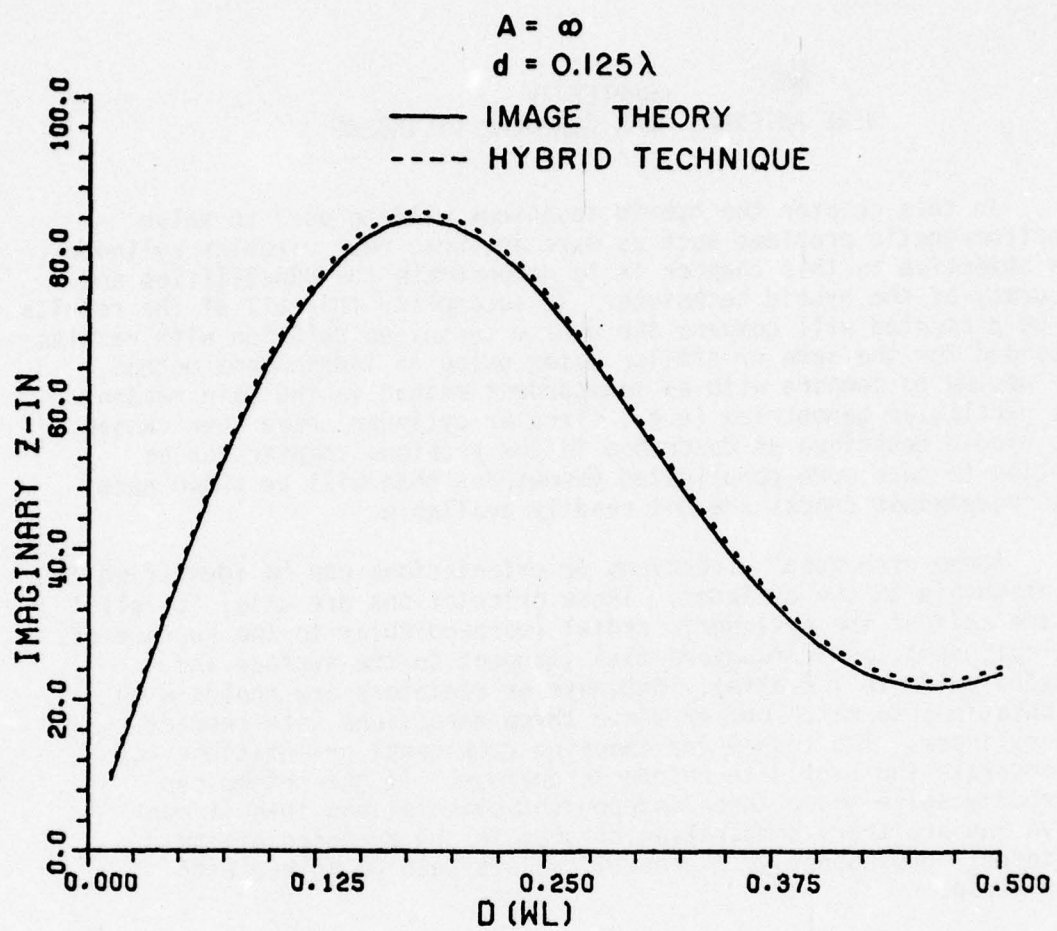
Figure 23b. Imaginary part of axial dipole input impedance
near cylinder of radius A=∞.

57

CHAPTER IV
WIRE ANTENNAS NEAR CIRCULAR CYLINDERS

In this chapter the hybrid technique will be used to solve electromagnetic problems such as wire antennas near circular cylinders. The objective in this chapter is to demonstrate the capabilities and accuracy of the hybrid technique. To accomplish this all of the results to be presented will compare the hybrid technique solution with results obtained for the same or similar cases using an independent method. The desire to compare with an independent method is the main reason the particular geometries (e.g., circular cylinder) have been chosen. The hybrid technique as described in the previous chapter can be applied to much more complicated geometries than will be shown here, but independent checks are not readily available.

Three orthogonal directions or orientations can be identified in relationship to the cylinder. These orientations are axial (parallel to the axis of the cylinder), radial (perpendicular to the surface of the cylinder), and circumferential (tangent to the surface and perpendicular to the axis). Antennas or radiators are chosen with orientations to match one of these three directions with respect to the cylinder. The reason for choosing orthogonal orientations to demonstrate the hybrid technique is obvious. If the method can correctly solve these three independent orientations then it can solve any arbitrary combination of them in the presence of the cylinder. Subsequently, a general radiator can be solved with confidence.

The electromagnetic problems solved in this chapter will all involve the calculation of input impedance of the radiator as a function of distance from the cylinder. The hybrid method is capable of solving for many other electromagnetic parameters such as near or far field, current distributions, scattering data, patterns, as well as input impedance. There are three reasons for choosing to find input impedance. To determine input impedance, the current distribution is first found. If the current distribution is known, all the other electromagnetic parameters follow easily. So finding input impedance shows that the other parameters could also have been accurately determined. The second reason is that input impedance is a measurable quantity and one which can be compared with other literature. The third reason is that the current distribution and correspondingly the input impedance of the radiators is very sensitive to the location of the nearby circular cylinder. Thus, solving for input impedance is a good test of the capabilities of the hybrid technique.

Finally, circular cylinders are picked as the curved surface whose presence is to be included for the following reason: GTD and therefore the hybrid technique is capable of solving many canonical (and combinations thereof) problems, but, the circular cylinder is one for which other solutions are available. The computer program developed using the hybrid technique of Chapter III and the theory of Chapter II is capable of solving an arbitrary radiator near an elliptic cylinder.

In developing the computer programming to solve electromagnetic problems using the hybrid technique, an effort was made to keep the expressions and possible geometries as general as possible. The objective was to develop a program capable of handling as broad a problem type as possible. To achieve this, the thin-wire program of Richmond [2,3] was chosen as the starting point for the moment method formulation of the problem. Some reasons for that choice are based on the use of piecewise sinusoidal basis functions as was discussed in Chapter II. Another reason is because of the wide familiarity, acceptance, and use this thin-wire program has. The hybrid computer program is outlined as follows: A wire model of the antenna structure geometry is inputted. The necessary specifications characterizing the curved surface are also read in. The antenna structure is sorted and the thin-wire modes are set up. The free space impedance matrix is then found. Next various appropriate subroutines are called to find the modifications to [Z] due to the curved surface starting with the GO routine. The subroutines to find the modifications use GTD programs modified from ones developed by Burnside, Marhefka, Greer, and others at the Ohio State University. The programs use expressions from a paper by Kouyoumjian and Pathak [5]. The [Z'] matrix is calculated and the current distribution is found. The hybrid program was used on a modified Datacraft computer.

Four specific geometries will be studied in this chapter. Three independent methods of solution will be used to test the hybrid solution. These methods will be discussed as they are used. The agreement between these methods and the hybrid technique, as will be shown by the results in this chapter, strongly support the statement that an accurate method for combining the moment method treatment of wire antennas with the GTD for curved surfaces has been found.

A.   Axial Dipoles

In this section the results of applying the hybrid technique to axially oriented dipoles a distance D from a perfectly conducting circular cylinder of radius A are presented. The general geometry of the problem is illustrated in Figure 24. The dipole antenna is half-wave length in extent and the diameter is .0002λ. Note that the circular cylinder is labeled infinitely long. This is rigorously true but in practice as long as the cylinder extends approximately one wavelength or more past the dipole it appears to be infinitely long as far as the dipole's current distribution is concerned. This statement
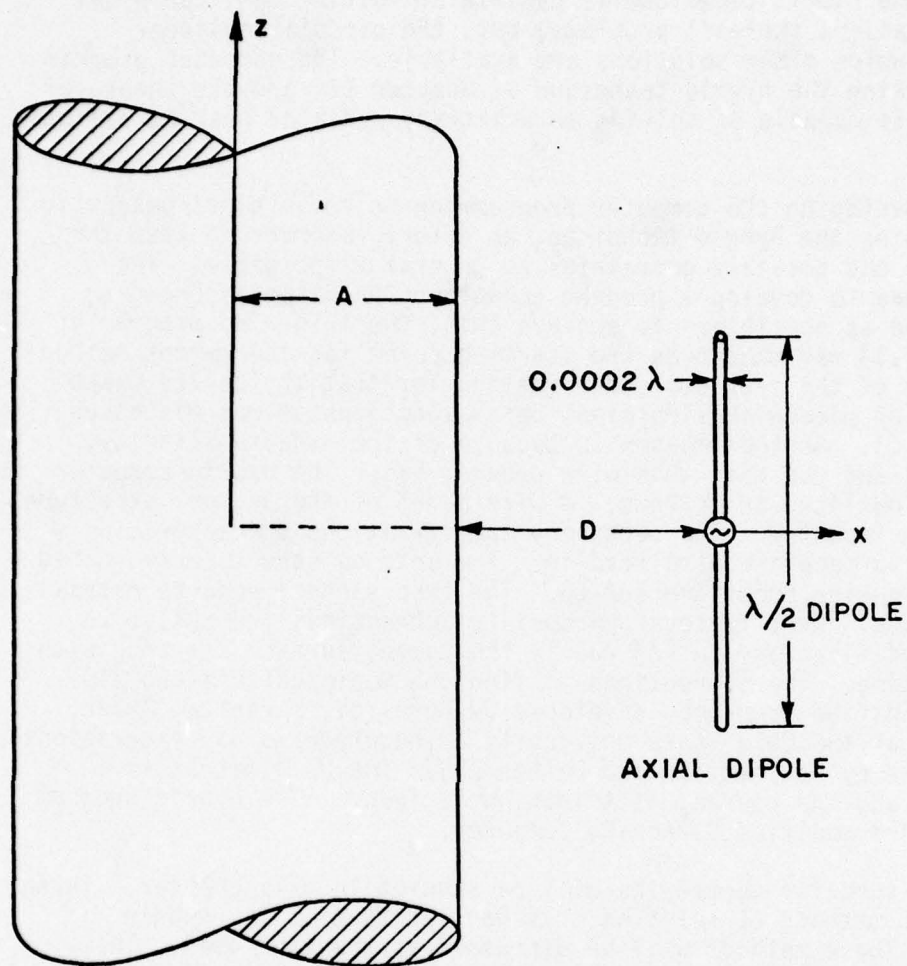
59

Figure 24. Half-wave dipole axially oriented a distance D
from a perfectly conducting circular
cylinder of radius A.

will be supported by the results in the finite cylinder section of this chapter.

As discussed in Chapter III an MM-eigenfunction solution by Ersoy and Wang [11] is available for axially oriented dipoles near an infinitely long, perfectly conducting, circular cylinder. The solution is found by summing sufficient terms to evaluate an integral expression. The integrand contains a Green's function for the circular cylinder. The dipole has a cos(kz) current distribution. This MM-eigenfunction solution can be considered exact and is a perfect independent method to check the hybrid solution against. The restriction is that in order to achieve the cos(kz) current necessary for correct comparison the hybrid technique must use only one mode or two segments to model the half-wave dipole.

The first results comparing the hybrid technique with the MM-eigenfunction solution are shown in Figures 25a and b. The real and imaginary parts of the input impedance of the dipole were plotted vs. dipole distance from the cylinder D. For this case D was varied from near 0 to onehalf wavelength and the cylinder radius was one wavelength. The vertical axis are in ohms, the solid line is the MM-eigenfunction solution, and the dotted curve is the hybrid solution. The two methods give basically the same result. The largeness parameter for the GTD, or in this case the GO, part of the hybrid solution is kA. k is the wave number equal to $2\pi/\lambda$. A is the cylinder radius given in wavelengths. GTD uses an asymptotic approximation which is good when the largeness parameter is greater than one. For the case A=1.0λ shown in Figures 25a and b the largeness parameter is about 6.3, much larger than one and the excellent agreement follows.

To demonstrate the effect of this largeness parameter on the hybrid solution three more cases are presented. Figures 26a and b show the input impedance when A=0.5λ. Figures 27a and b show the effect when A=0.25λ where kA is still greater than one. Finally Figures 28a and b show the input impedance curves calculated by the two methods when kA=.785. This last case has violated the largeness parameter constraint yet the agreement between the MM-eigenfunction and hybrid solutions is still fairly good. Comparing the amount of error in the hybrid solution for these cases as kA gets smaller it is seen that the GO breaks down gracefully. One can push the hybrid technique as far as is consistent with the desired accuracy of the particular application and not worry about sudden breakdown.

When the cylinder radius is very large the MM-eigenfunction solution needs more terms to converge. For this reason and the need to verify the accuracy of the hybrid solution when the dipole is modeled with more than one mode, the method will be compared with a ground plane image theory solution. In Chapter III the image theory method was discussed. As A goes to infinity the cylinder opens to an infinite planar conducting surface or ground plane. Richmond has adopted his
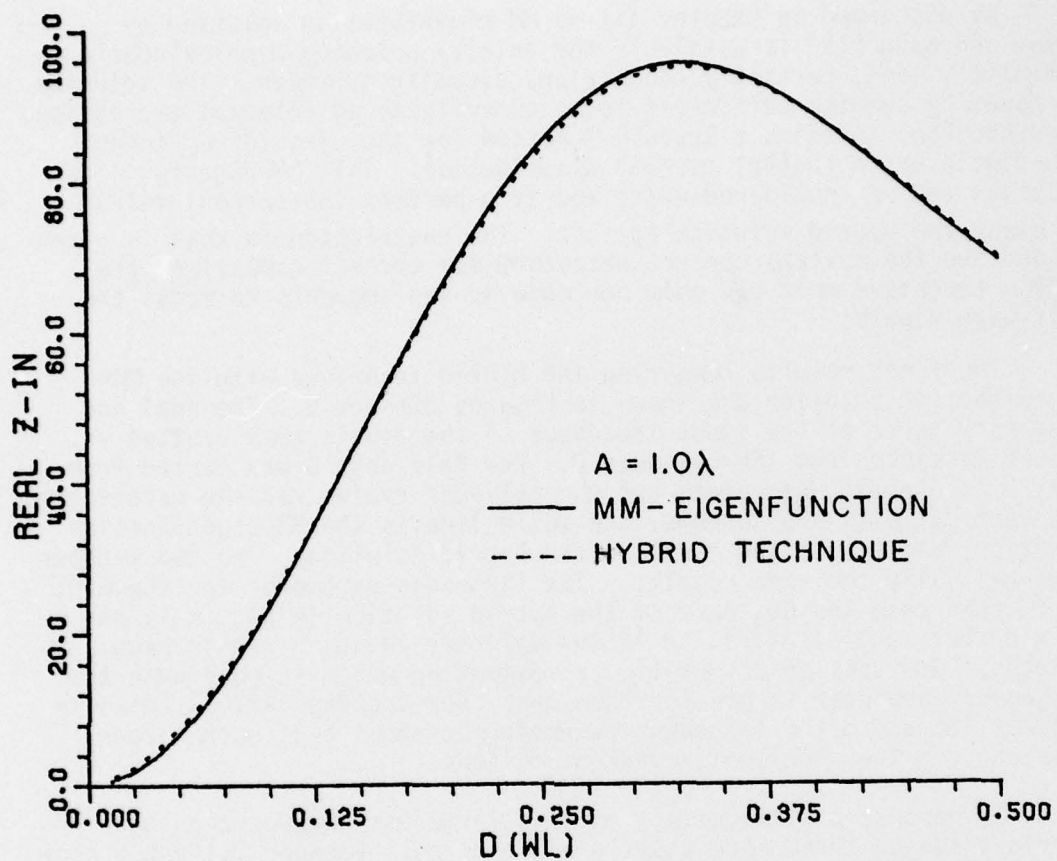
61

Figure 25a. Real part of axial dipole input impedance
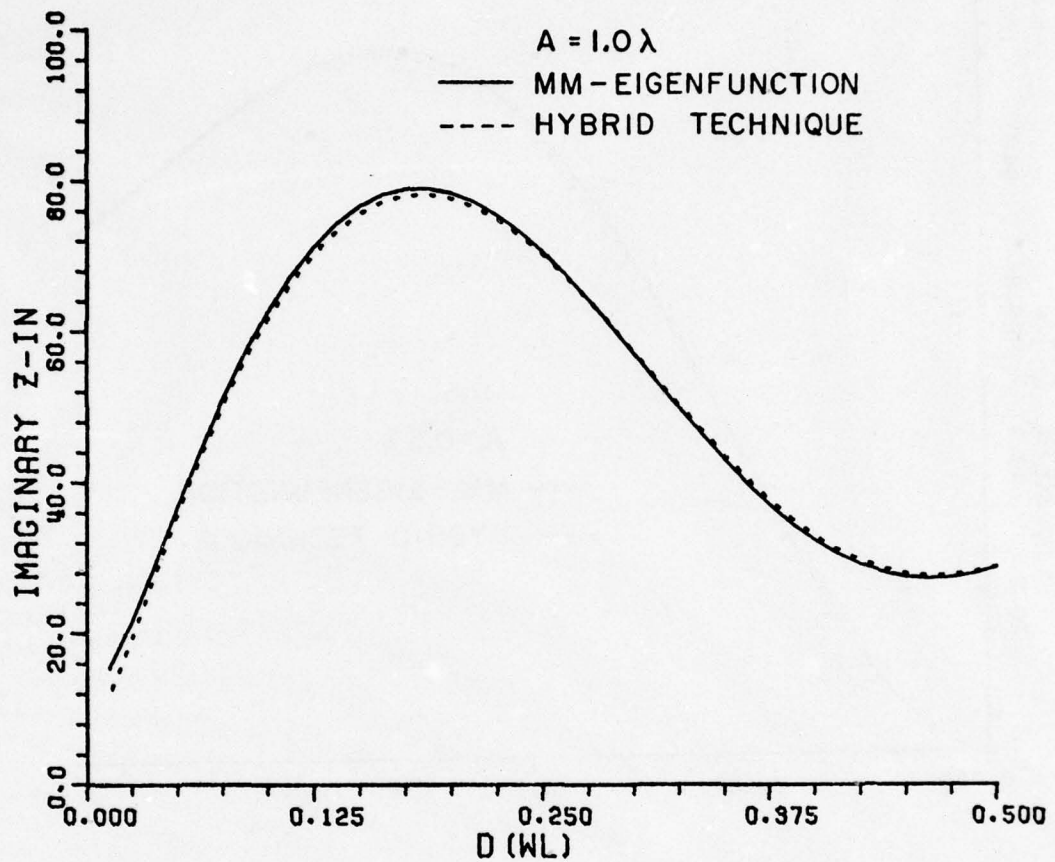near cylinder of radius A=1.0λ.

Figure 25b.   Imaginary part of axial dipole input impedance
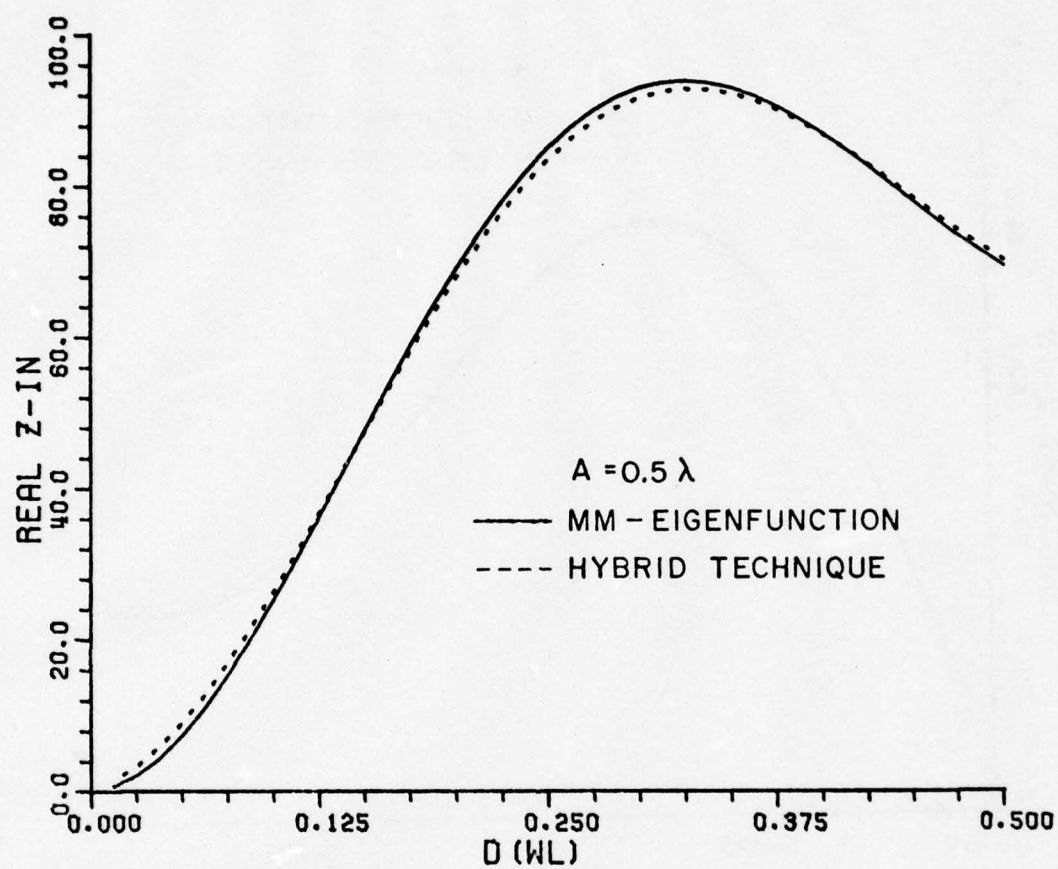near cylinder of radius A=1.0λ.

63

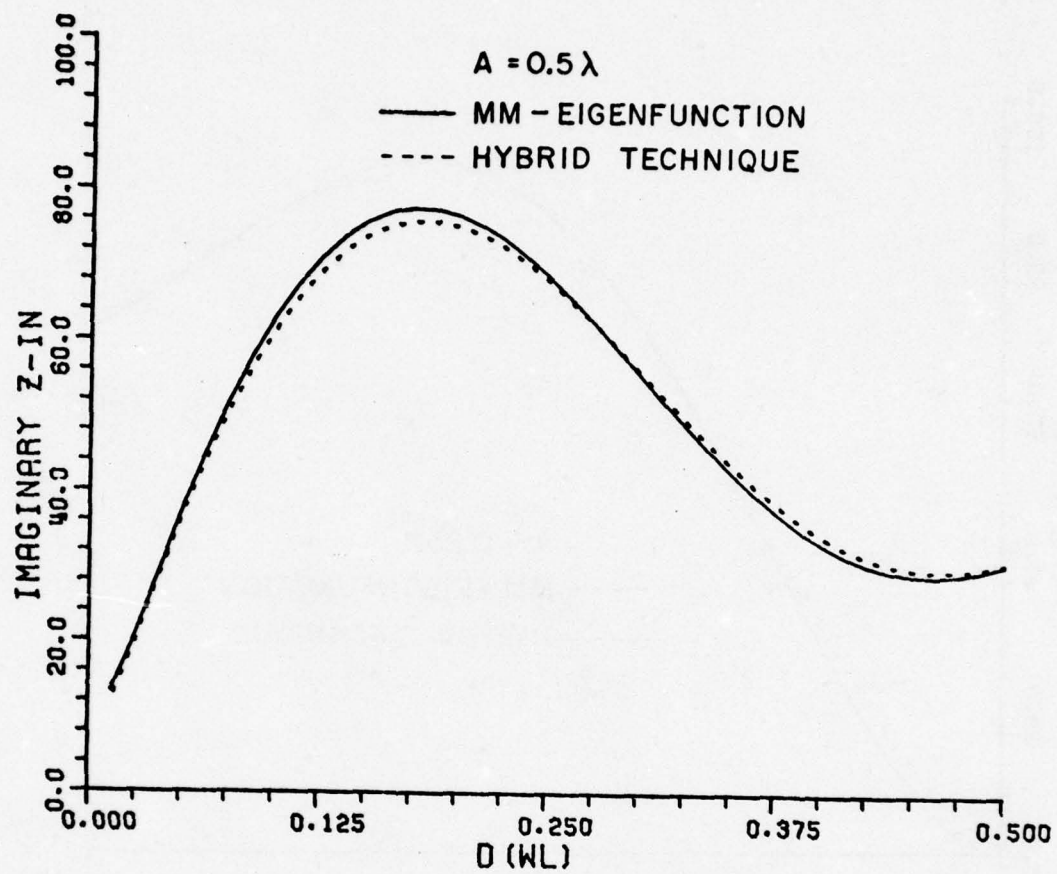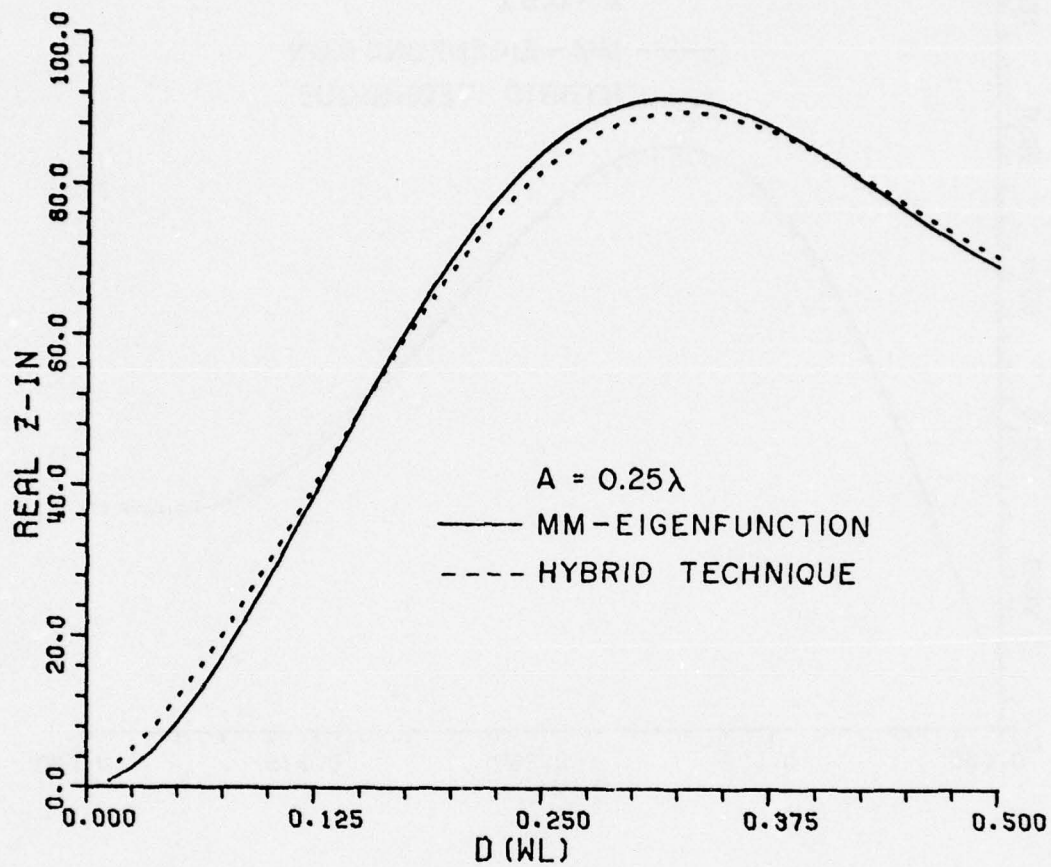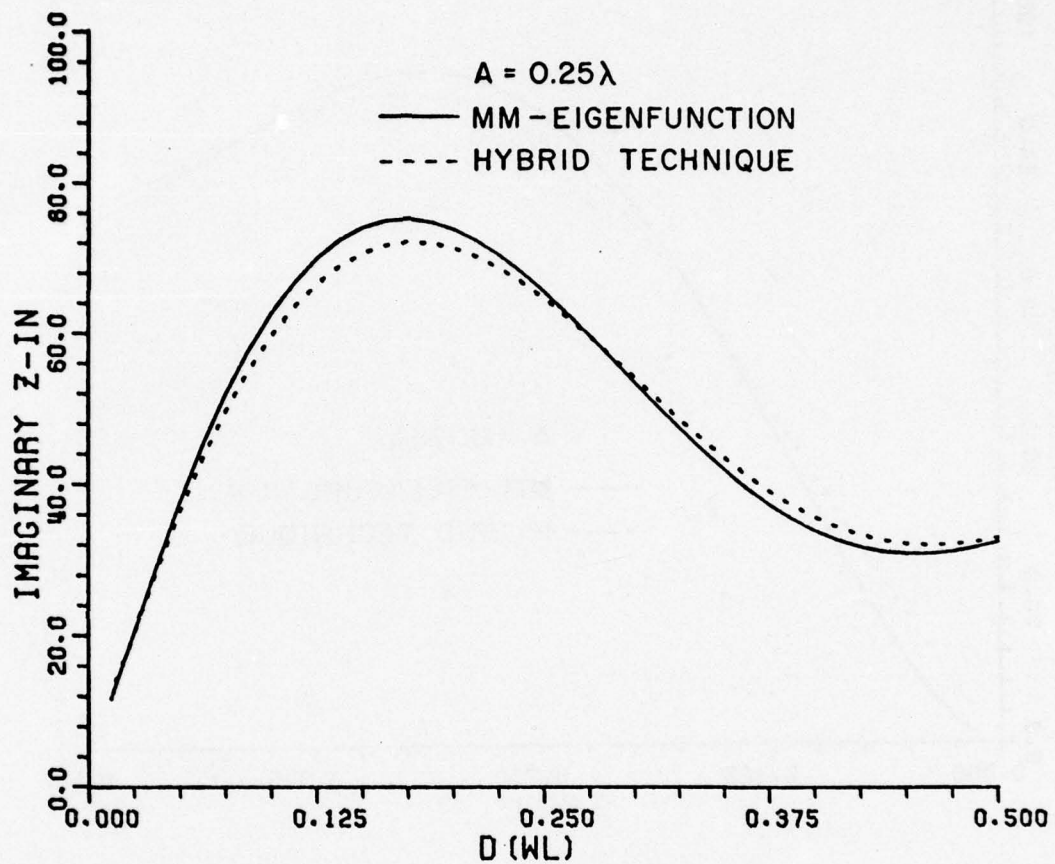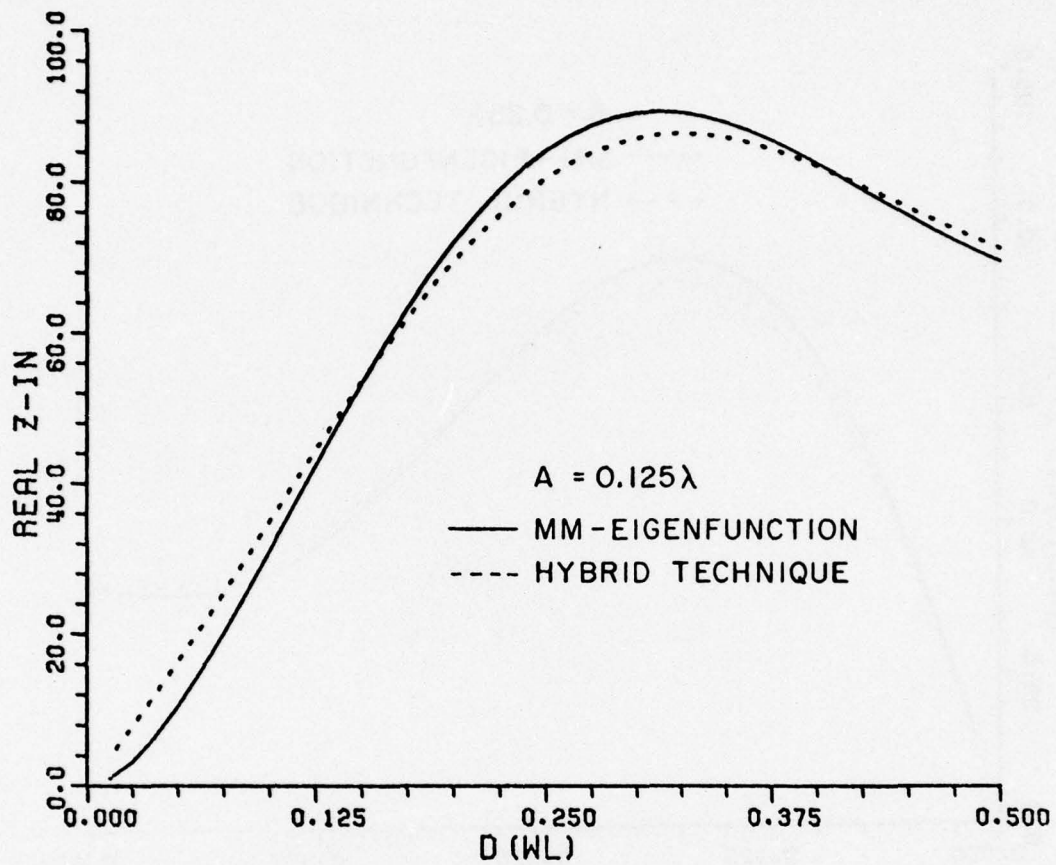Figure 26a. Real part of axial dipole input impedance
near cylinder of radius A=0.5λ.

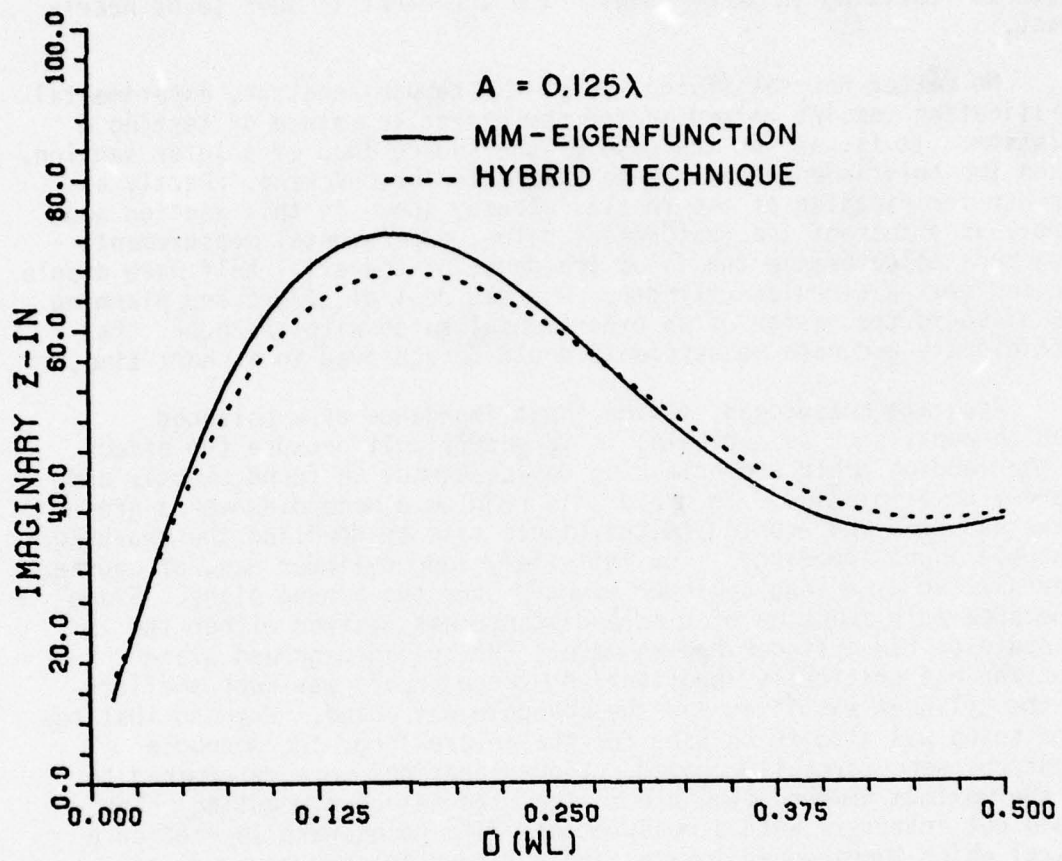Figure 26b. Imaginary part of axial dipole input impedance
near cylinder of radius A=0.5λ.

65

Figure 27a. Real part of axial dipole input impedance near cylinder of radius A=0.25λ.

Figure 27b. Imaginary part of axial dipole input impedance near cylinder of radius A=0.25λ.

67

Figure 28a. Real part of axial dipole input impedance
near cylinder of radius A=0.125λ.

Figure 28b. Imaginary part of axial dipole input impedance near cylinder of radius A=0.125λ.

69

thin-wire program to handle this geometry [12]. Solving the case
illustrated in Figure 24 when the cylinder radius was A=10.0 gave the
curves shown in Figures 29a and b. The solid curve was calculated
using ground plane image theory. Again, the dotted curve is the hybrid
solution. In each of these methods the dipole was modeled with four
segments resulting in three modes. The agreement is seen to be nearly
exact.

No matter how satisfying analytical comparisons are, experimental
verification remains an undisputed and effective method of testing a
solution. It is, as for the case of the square loop of a later section,
often the only independent method available for checking. Partly as
further verification of the results already shown in this section and
partly as a test of the measurement setup, experimental measurements
were made to determine the input impedance of the axial half wave dipole
located near a circular cylinder. A great deal of effort and planning
was given to the design of an experimental setup with the hope that
sufficiently accurate measurements could be achieved in a short time.

Accurate measurement of the input impedance of a balanced
feed antenna, such as a dipole, is very difficult because the effect
of the feeding cable and balancing device cannot be found exactly and
thereby be eliminated. To avoid this problem a monopole over a ground
plane was used and equated to the dipole case by doubling the measured
monopole input impedance. The infinitely long cylinder was, of course,
approximated by a long cylinder mounted over the ground plane. Since
impedance as a function of dipole distance was desired either the
monopole or the cylinder had to move. The cylinder-ground plane
junction was critically important and the monopole was much smaller,
so the cylinder was fixed and the monopole was moved. Knowing that the
same setup was also to be used for the square loop, the monopole
locations were carefully chosen. Eight locations were determined to
be the maximum number allowable so that the adjacent mounting holes
would not interfere with a measurement. The holes were located on a
spiral which tappered in towards the cylinder in such a way as to
result in equal clearance angles between the square loop locations.

The size of the various components of the setup as well as the
selected frequency of operation were dictated by the available material,
practical mechanical and electrical sizes, and the available test
equipment. The four foot by four foot ground plane sets a lower limit
on the frequency since the plane had to be about two wavelengths or
more to appear infinite. A five inch diameter cylinder was the
largest diameter available and since a sufficiently large kA was
desired, the five inches was picked to be one-half wavelength.

A high frequency limit of the experimental setup was the diameter
of the monopole. The N-type connector used to attach the monopole to
the ground plane had a center wire diameter of one-eigth inch. To
avoid a discontinuity right at the feed point the monopole diameter
was chosen also to be one-eighth inch. Thin-wire theory as used in
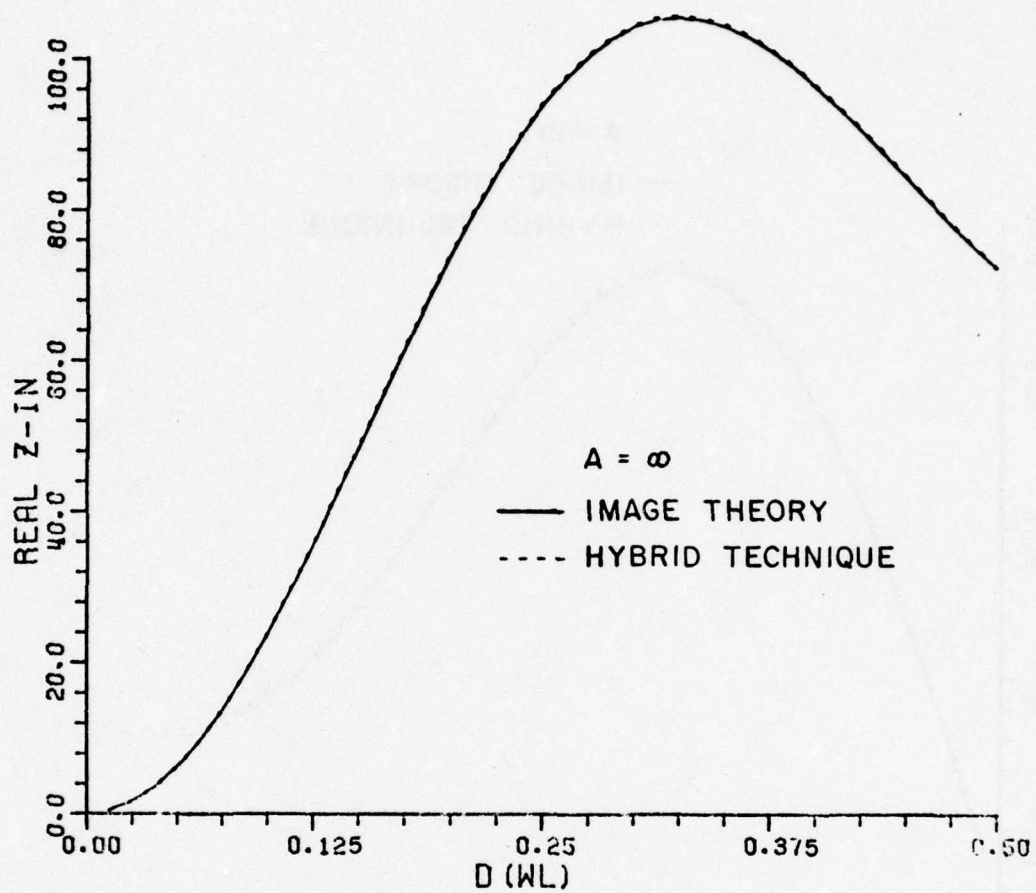the hybrid technique restricts wire radii to be less than about .007λ.

Figure 29a. Real part of axial dipole input impedance
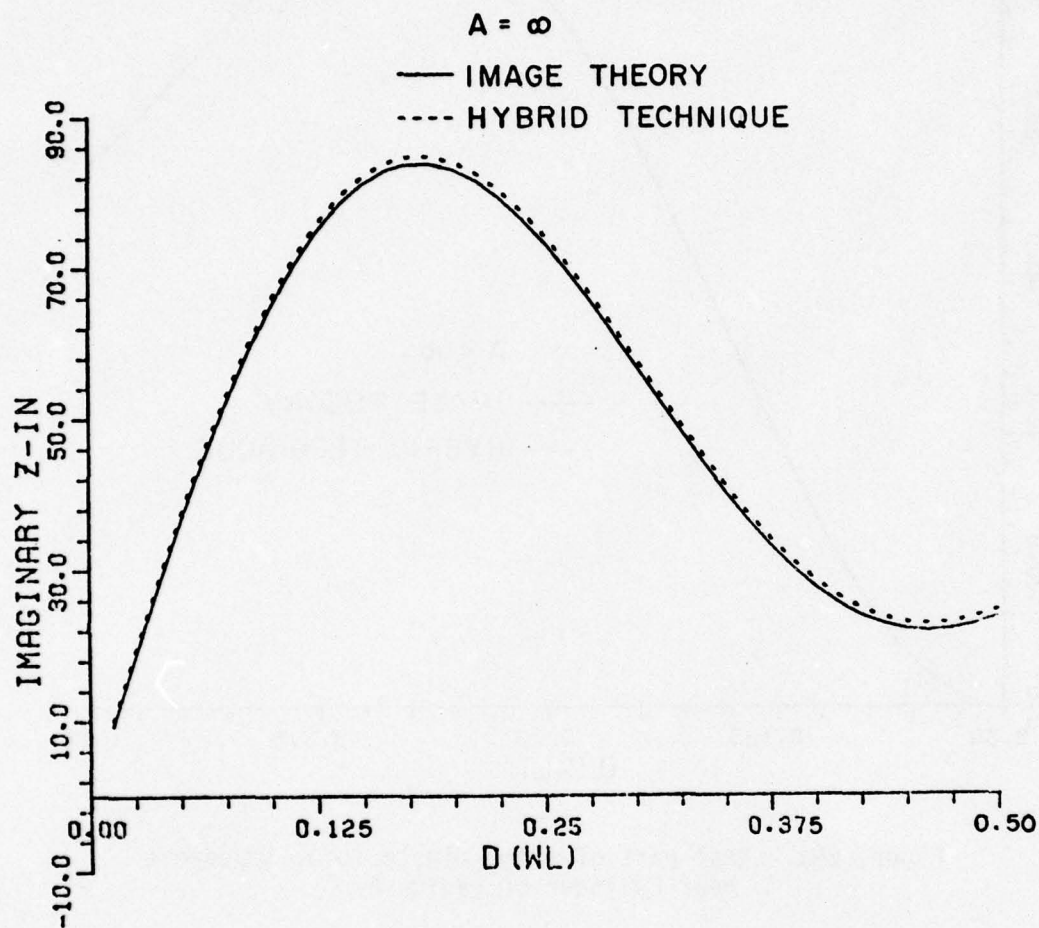near cylinder of radius A=∞.

71

Figure 29b.   Imaginary part of axial dipole input impedance
near cylinder of radius A=∞.

72

The frequency of operation to make the five inch cylinder one-half wave-length is 1.1811 GHz. At this frequency the monopole diameter is .00635λ. Thus the dimensions and frequency are fixed. In order to be equivalent to the half-wavelength dipole, the monopole was cut to one-quarter wavelength or 2.5 inches. All of the above components were carefully machined to the specified sizes and assembled to make good, smooth electrical contact which was necessary because of the high operating frequency. The cylinder and ground plane were aluminum and the monopole was brass. The conductivity of these materials was high enough to be assumed perfect.

Measurement of input impedance was accomplished indirectly by equipment used to accurately measure the reflection coefficient at the monopole port. Figure 30 shows a schematic of the equipment used in the measurement setup. Figure 31 shows a picture of the actual equipment as set up during a measurement. Note that the equipment is located under the ground plane so that it cannot interfere electrically with the measurement. Figure 32 shows the various radiators, which were used located about the cylinder.

Again input impedance was found by measuring the complex reflection coefficient referenced to a short on the surface of the ground plane. The signal source was a sweep frequency generator with circuitry to lock the signal level over a frequency band. The generator fed an s-parameter device which contained a line strecher to match the test line with a reference line over a frequency band. The s-parameter device had an attached coupler which compared the test and reference signals and sent a complex voltage proportional to their difference to a signal analyzer with display units. The display unit then allowed the signal to be pictured on a CRT magnitude and phase plot or to be read accurately in dB on a magnitude and phase meter.

The measurement procedure went as follows: the antenna and cylinder were secured in the position for the measurement. A sweep frequency signal from 1.0 to 1.4 GHz was fed to the antenna through the s-parameter device. Using the CRT display, the line stretcher was adjusted so that a short at the antenna port appeared as a single point at 1.0/180°. The short was then removed and the reflection coefficient was observed on the CRT over the frequency band to insure that no problems (i.e., glitches or discontinuities) existed in a frequency range about the frequency of interest, 1.1811 GHz. The generator was then adjusted with a frequency counter for the CW signal. The display meter replaced the CRT and the reference levels were adjusted while measuring the short. With the short removed the reflection coefficient was measured accurately on the most sensitive scale settings. Environmental effects such as unwanted reflections were checked using a reflecting disk. The measurements made using this procedure and equipment proved to be very stable and repeatable.
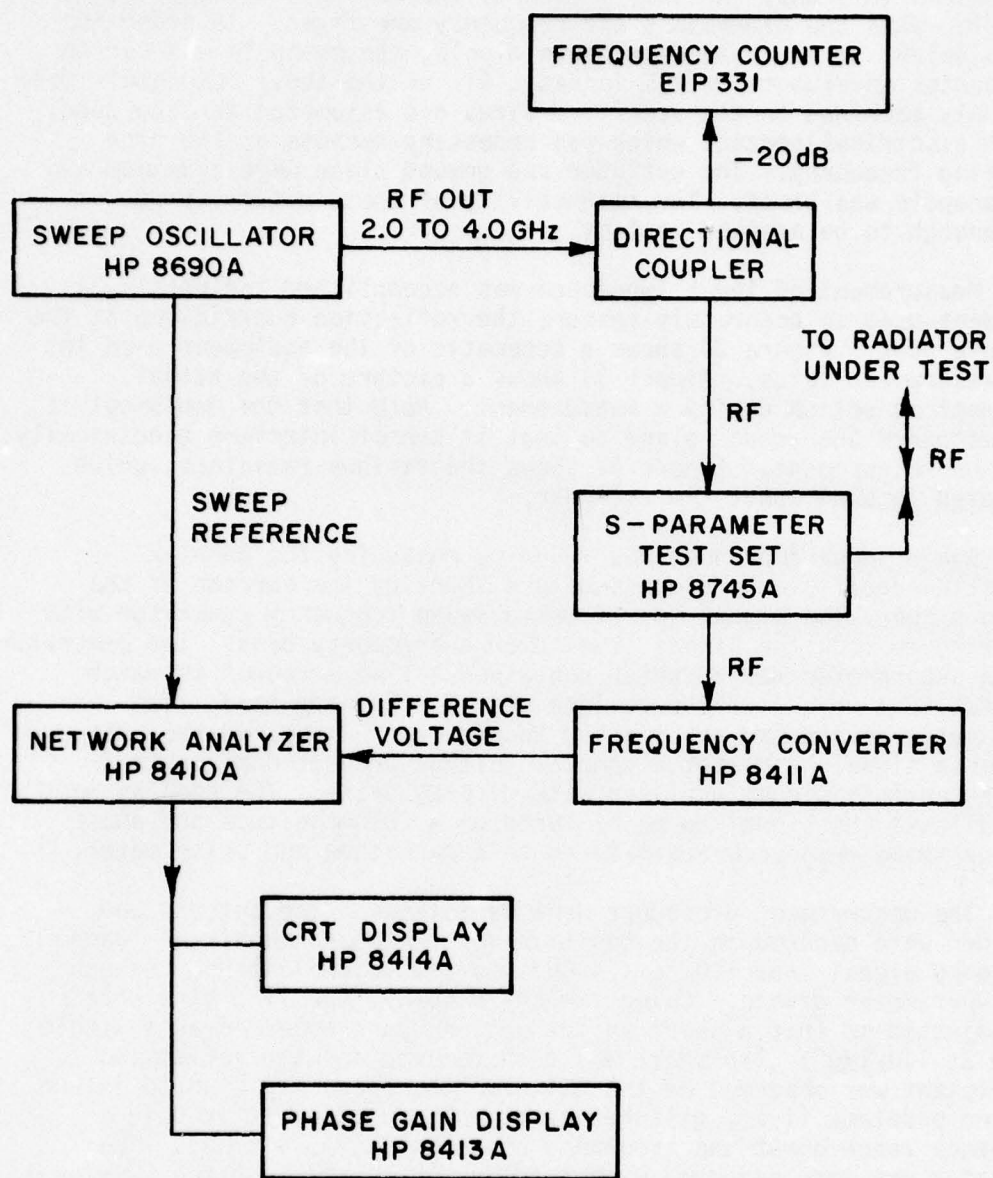
73

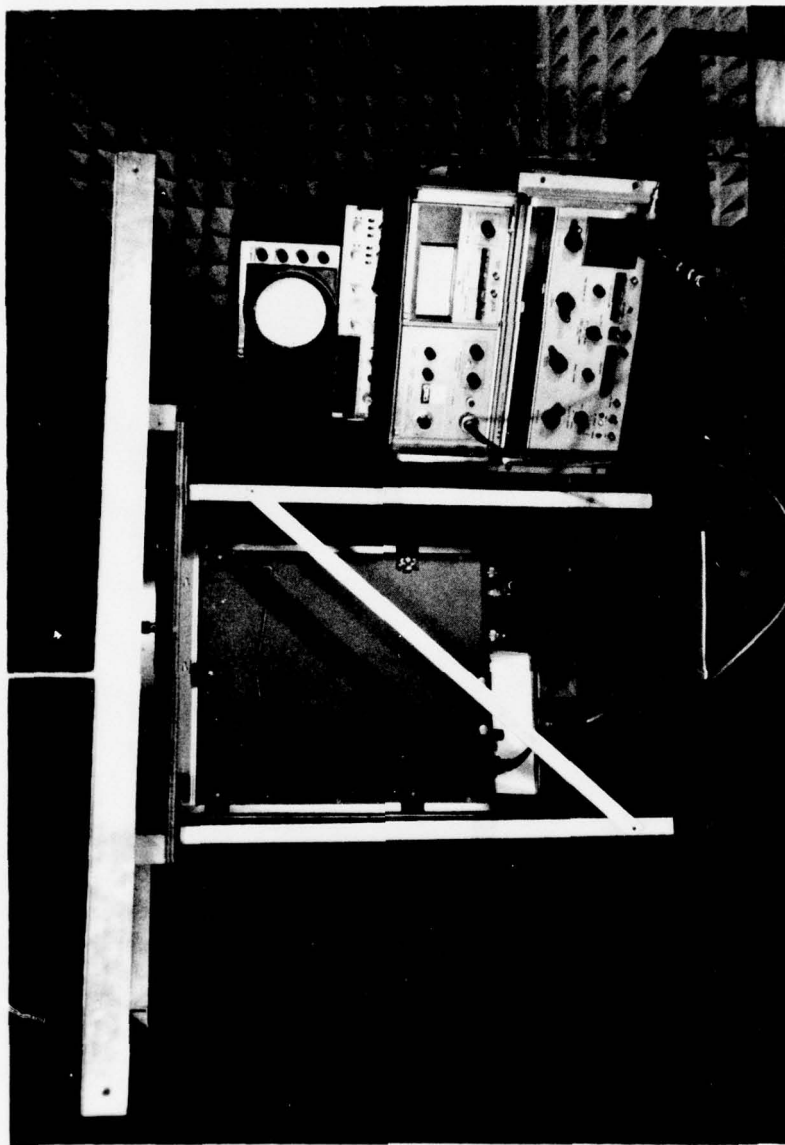Figure 30. Block diagram of experimental measurement setup.

74

Figure 31. Experimental setup showing ground plane mounted over test equipment.
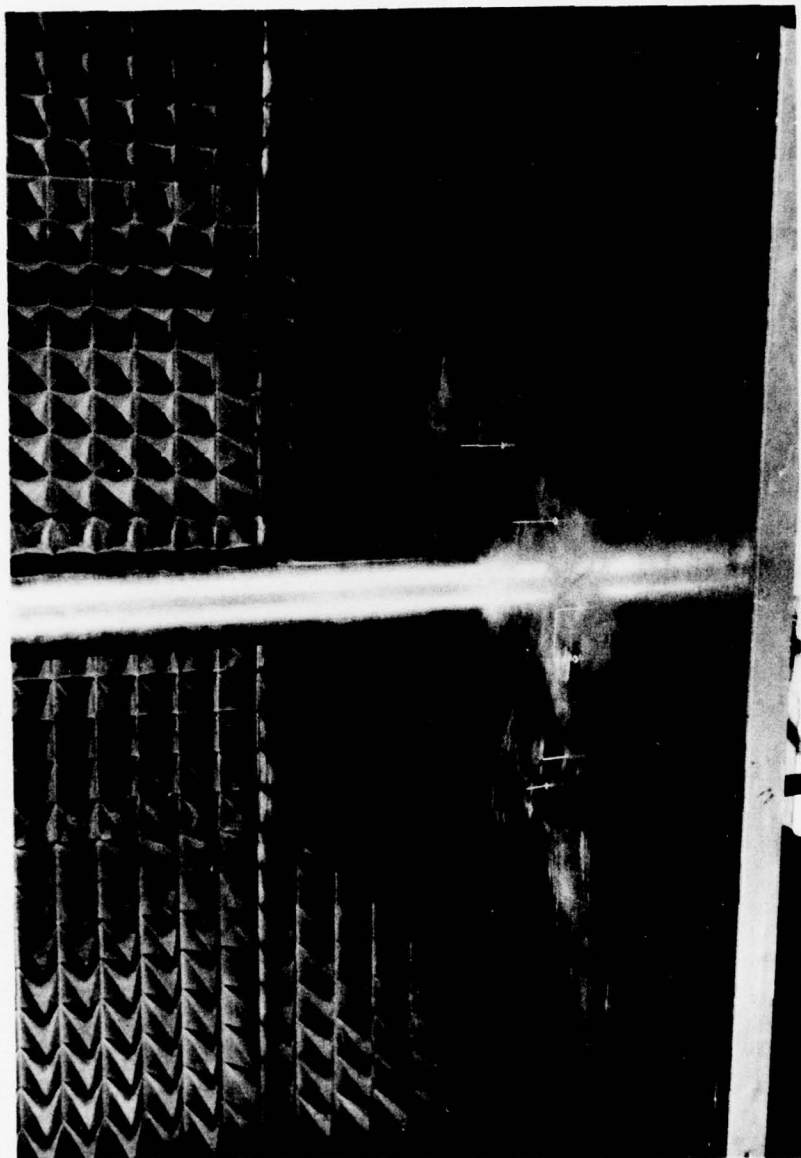
Figure 32. Various antenna measured mounted over ground plane around the cylinder.

76

To convert the reflection coefficient R to the input impedance, the following formula was used:

$$Z_{in} = Z_o \frac{1 + R}{1 - R} \tag{74}$$

where Z_o is the characteristic impedance of the connectors and cables attaching the signal source to the monopole ($Z_o=50\Omega$).

To compare with experimental measurements several adjustments to the dipole data inputted to the hybrid technique are necessary. There are no modes in the physical setup but the number of modes used in the hybrid technique has a significant effect on the input impedance. To determine the number of modes necessary to get a converged number, the input impedance of the dipole was calculated with D fixed at approximately 0.625λ and the number of modes was varied from one to twenty five. The resulting plots for real and imaginary part of Z_{in} are shown in Figures 33a and b. Note that the vertical scales have been greatly magnified to exaggerate the effect. Choosing 9 modes to model the dipole will result in the real part being only 0.7% below the 25 mode value while the imaginary part will be within 3.0%. The choice of 9 modes is thus justified.

Another adjustment which must be made is the diameter of the dipole to 0.0125λ. This results in a length to radius ratio of 40 for the dipole. This is small enough to be considered moderately thick. Two effects may be significant for a thick dipole. E-field fringing is one which thin-wire theory correctly handles if sufficient modes are used. End capacitance is the second effect due to charges on the ends. However, one of the thin-wire assumptions is that the current goes to zero at the ends of the dipoles. Forcing the current to zero at the end incorrectly eliminates the end charge effect. A reasonable approximation to improve the model to more closely fit the physical conditions which lets the current be non-zero at the ends is made. The current is allowed to spill over the edge of the end and go to zero at the center. To approximate this with the thin-wire part of the hybrid program, the antenna length is extended by the amount of one radius at each end.

The experimental measurements are now compared with the hybrid technique solution. Figures 34a and b are the resulting plots. The agreement between the measurement and the theory are quite remarkable.

Without discussing why at this point, measurements were made on a monopole with a radius four times smaller. This monopole would be considered thin but the above presented length adjustment was made regardless. Its effect was much smaller as expected. The plots comparing the hybrid technique with measurements for this thin dipole are shown in Figures 35a and b. Again, the agreement is very good with the absolute values almost matching as well as the variations matching quite well.
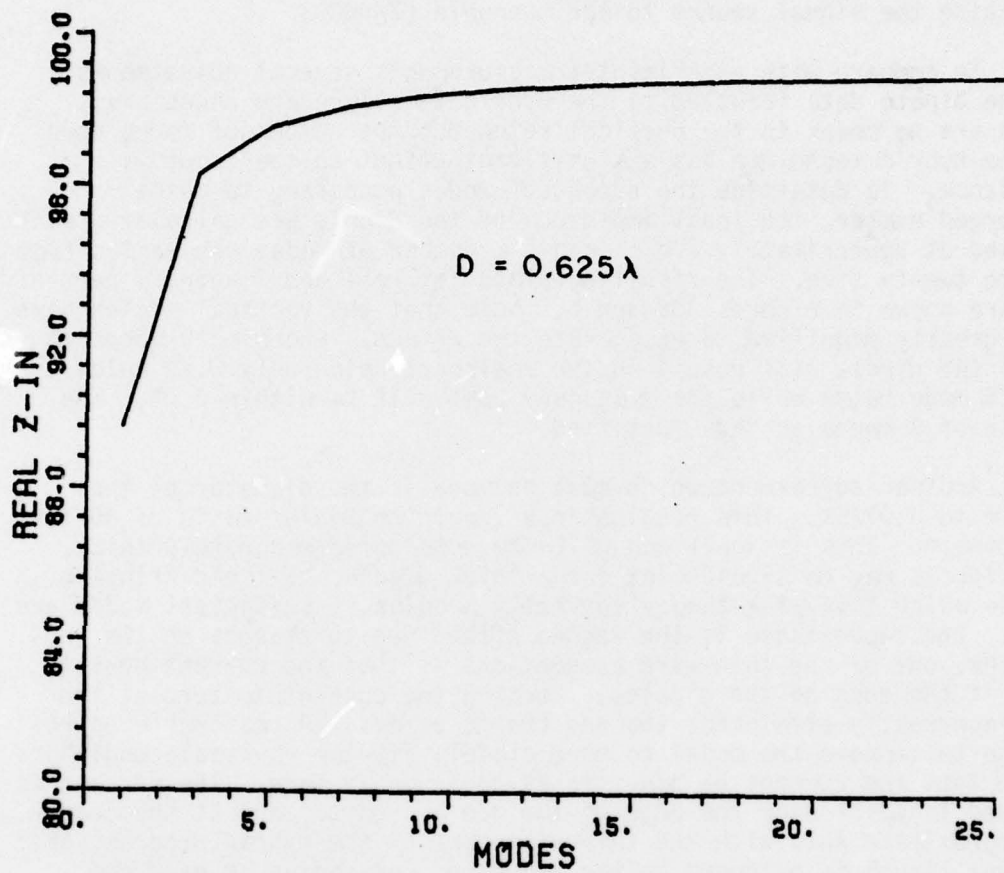
77

Figure 33a.   Real part of axial dipole input impedance as
a function of the number of modes used
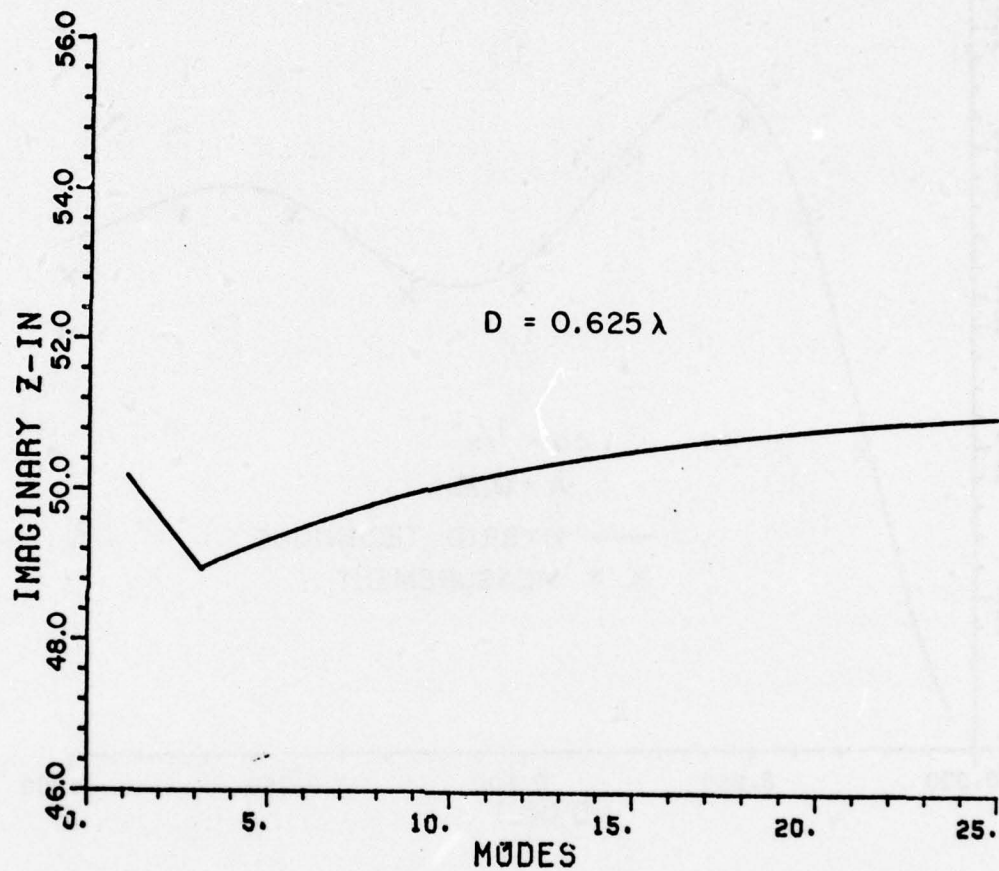to model the dipole.

78

Figure 33b. Imaginary part of axial dipole input impedance as a function of the number of modes used to model the dipole.
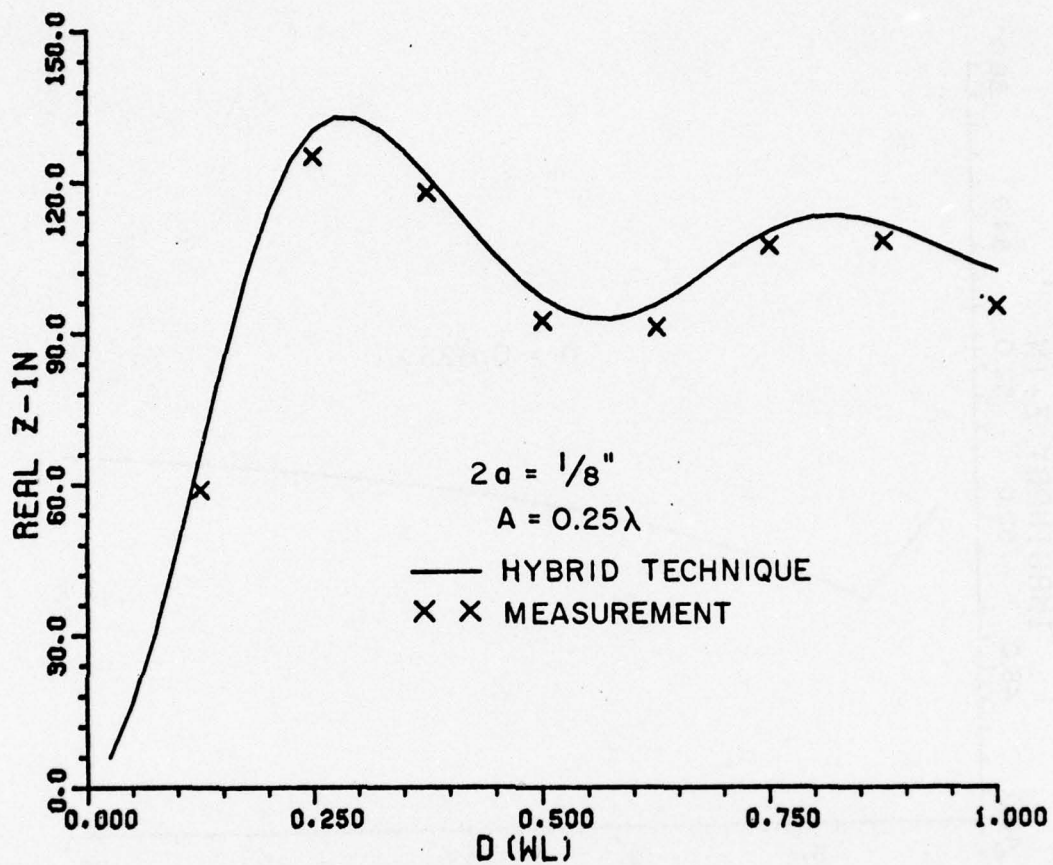
79

Figure 34a.   Real part of axial dipole input impedance
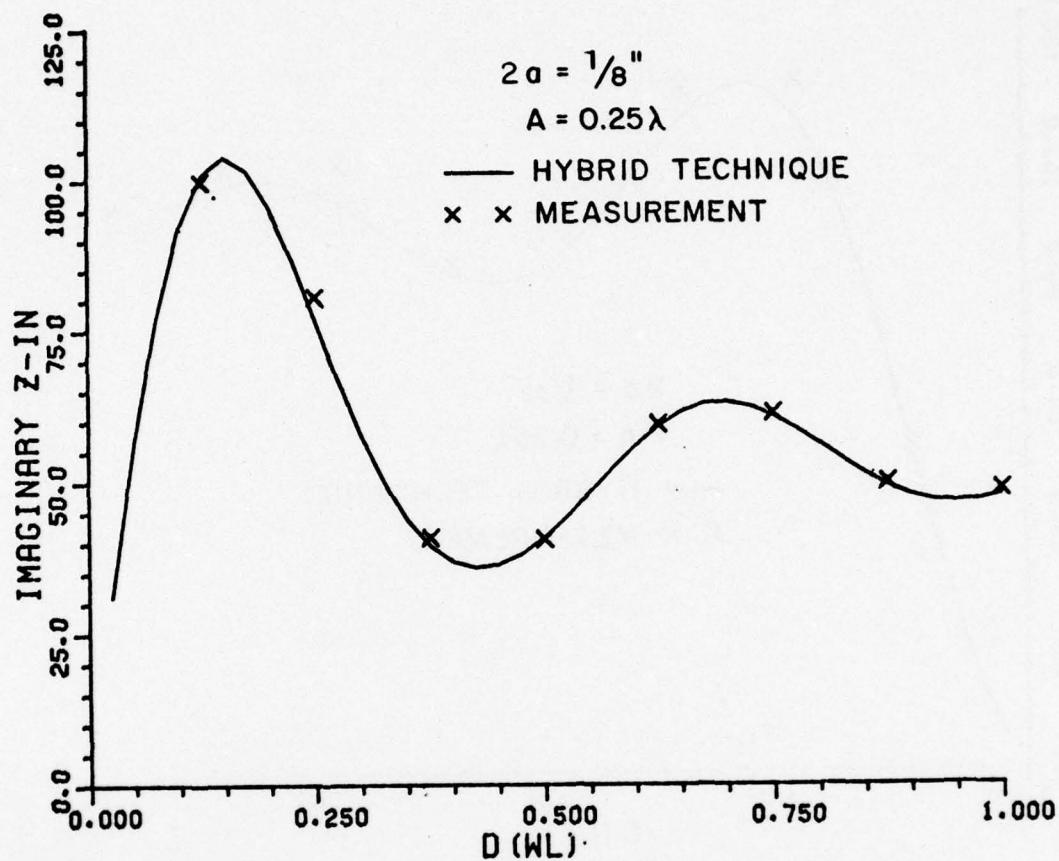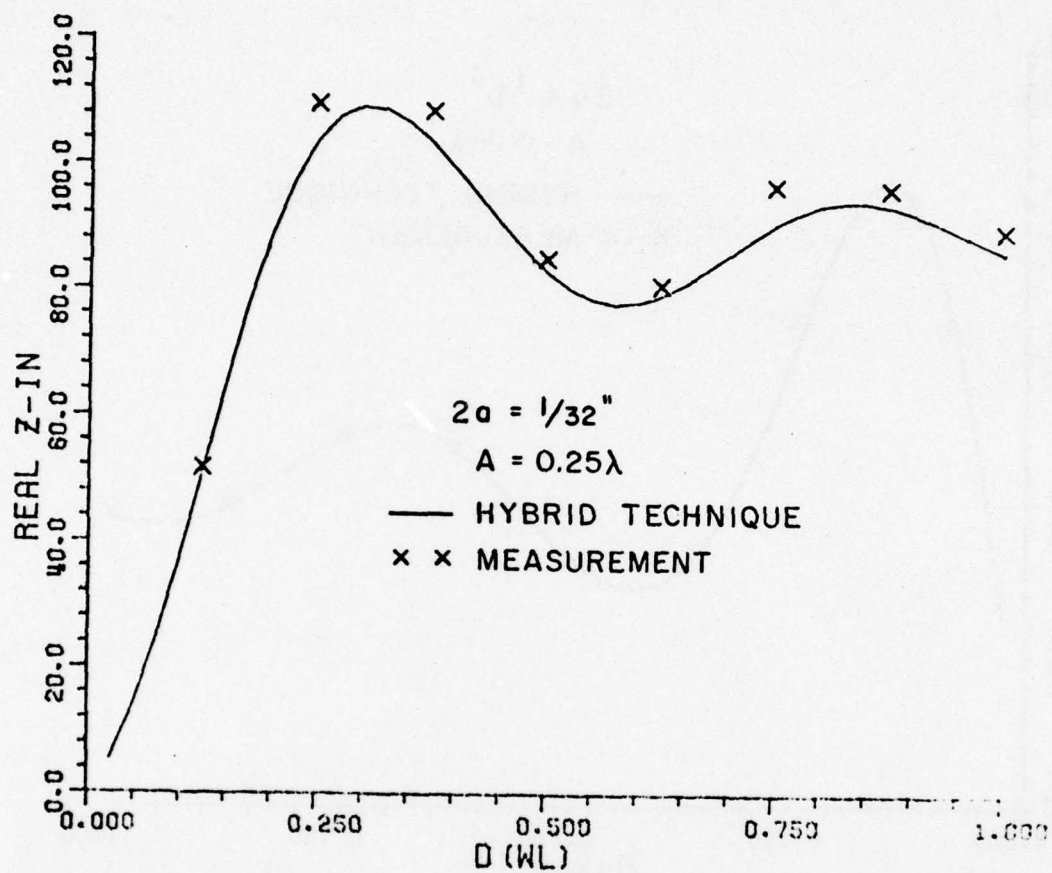near cylinder of radius A=0.25λ.

Figure 34b. Imaginary part of axial dipole input impedance
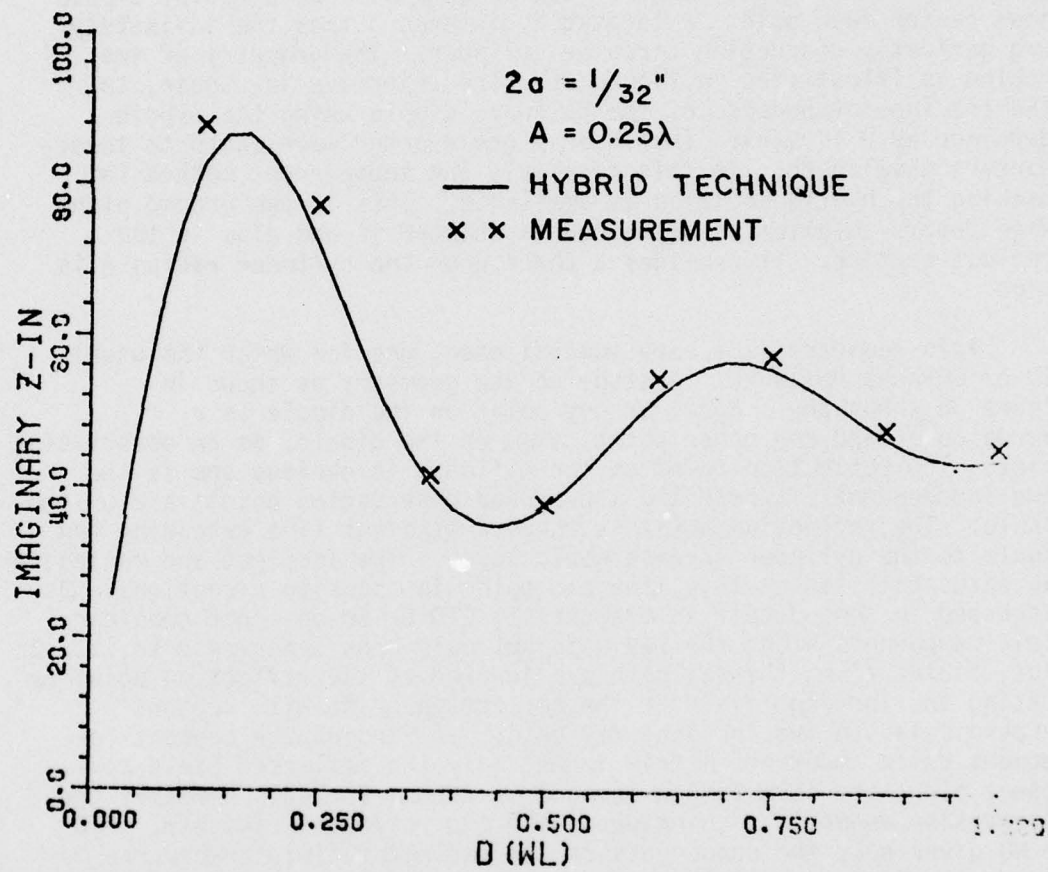near cylinder of radius A=0.25λ.

81

Figure 35a. Real part of axial dipole input impedance
near cylinder of radius A=0.25λ.

$2a = \frac{1}{32}''$

$A = 0.25\lambda$

—— HYBRID TECHNIQUE

x x MEASUREMENT

Figure 35b.   Imaginary part of axial dipole input impedance
near cylinder of radius $A=0.25\lambda$.

83

In this section then, the hybrid technique has been shown to give excellent results for an axially oriented antenna near a circular cylinder. The results were checked with three independent solutions. The method was found to be quite accurate with cylinders of radii from extremely large values down to only 0.125λ.

B. Radial Dipoles

The second radiator orientation which will be considered is the one radial to the cylinder. The antenna will be a radial dipole whose center feed point is located a distance D from the infinitely long perfectly conducting circular cylinder. The geometry of the problem is illustrated in Figure 36. The objective is, again, to find the input impedance of the halfwave dipole using the hybrid technique as D is varied from nearly one-quarter wavelength to three-quarters wavelength. In this case only one independent method for checking the hybrid solution is available. This is the ground plane image theory solution as described in Chapter II and also in the previous section. It provides a check when the cylinder radius A is large.

This geometry is a very special case, one for which the usual GTD or GO does not work. A study of the geometry as shown in Figure 36 shows why. Consider any point on the dipole as a source point and any other point, also on the dipole, as an observation point. The reflection point on the cylinder is obvious and is the same independent of where the source and observation points are on the dipole. The reflection point is where a straight line extending the dipole to the cylinder surface would touch. The incident and reflected ray paths both lie on this line and point in opposite directions. As discussed in some detail in Chapter II, GTD or GO does not consider field components along the ray path but only ones transverse to it. In fact, fields along the ray path are ignored at the reflection point by dotting the incident field at the reflection point with vectors perpendicular to the incident ray path. In finding the segment-to-segment delta impedance matrix terms, only the reflected field component along the observation segment is used. For this geometry the observation segment is coincident with the reflected ray path. GTD or GO gives only the components of the reflected field transverse to the observation segment thus giving all zero delta impedance matrix terms. The overall effect is that the hybrid technique using the GO as described thus far will predict no change in input impedance due to the presence of the circular cylinder. This is, of course, wrong.

To demonstrate the problem discussed above, the input impedance of the radial dipole was calculated and plotted as D varied. The results are shown in Figures 37a and b where the solid line is the image theory solution and the dotted line is the hybrid technique solution.
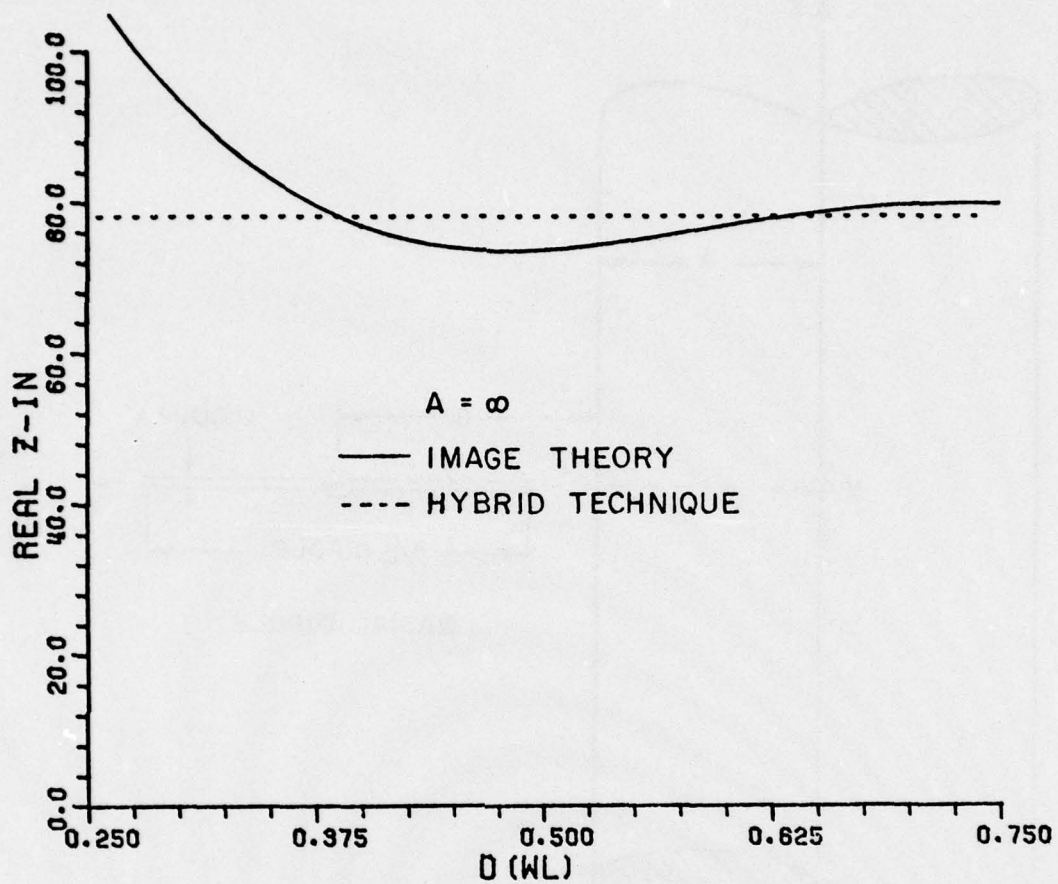
84

Figure 36. Half-wave dipole radially oriented a distance D
from a perfectly conducting circular
cylinder of radius A.

85

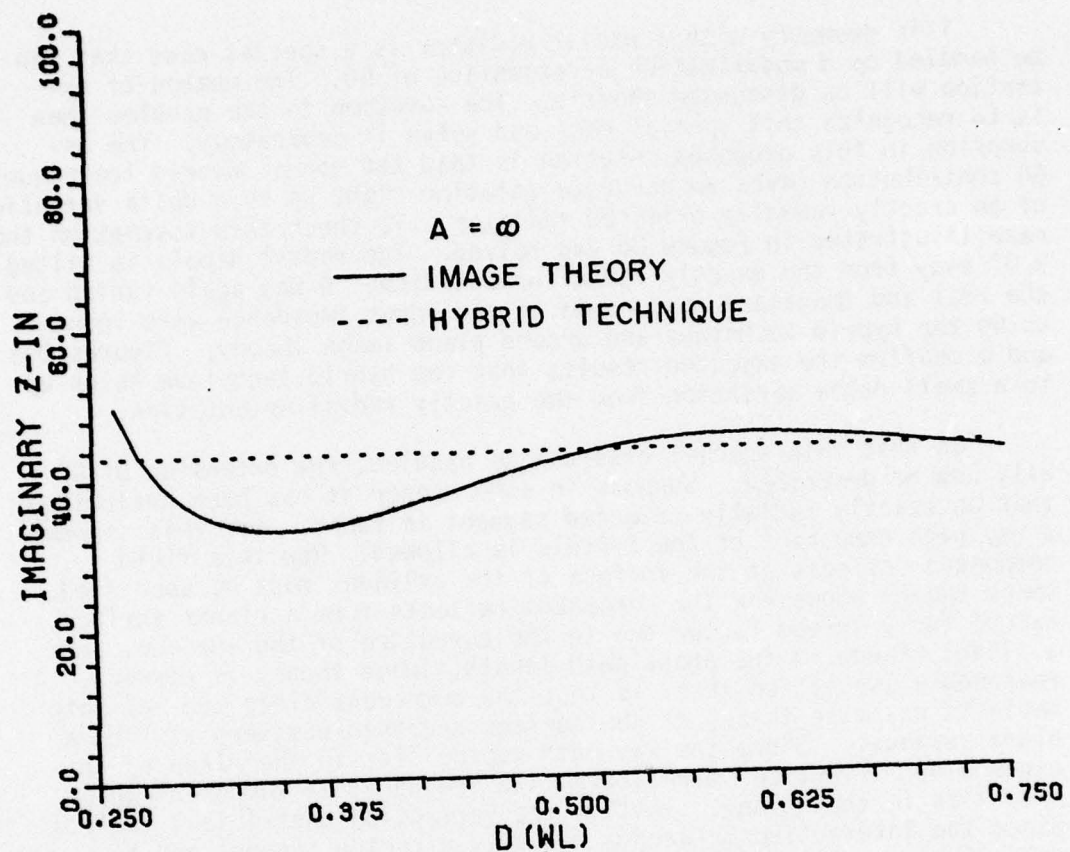Figure 37a.   Real part of radial dipole input impedance
near cylinder of radius A=∞.

Figure 37b. Imaginary part of radial dipole input impedance
near cylinder of radius A=∞.

As predicted, the hybrid solution incorrectly gives no effect from the cylinder and the components of the input impedance remain constant at their free space values as the dipole moves.

This geometry with a radial radiator is a special case that can be handled by a modification or extention of GO. The method of extention will be discussed shortly. The solution to the problem then is to recognize this special case and solve it separately. The assumption in this proposed solution is that the normal hybrid technique GO contribution gives an accurate solution right up to a delta variation of an exactly radially oriented radiator. To check this assumption the case illustrated in Figure 38 was solved. The radial dipole is tilted 5.0° away from the exactly radial orientation. D was again varied and the real and imaginary components of the input impedance were found using the hybrid technique and ground plane image theory. Figures 39a and b confirm the expected results that the hybrid technique holds up to a small delta variation from the exactly radial orientation.

So that this special case can be handled, the extension of GO will now be described. Suppose in some manner it has been determined that an exactly radially oriented segment is found. For this segment a ray path component of the E-field is allowed. How this field component reflects at the surface of the cylinder must be specified. Image theory shows how the component reflects from a planar surface. Except for a spread factor due to the curvature of the surface, and a slight change in the phase path length, image theory is correct. A reasonable assumption then, is that the component along the ray path reflects as image theory at the surface and then scatters as from a plane surface. Since the ray path vector lies in the plane of incidence or reflection it reflects like the parallel component which also lies in that plane. That is the reflection coefficient is +1.0. Since the interaction between a radially directed segment and the cylinder is small the image theory extension of GO should be quite good for large diameter cylinders, and become less accurate for small diameter cylinders.

To confirm the accuracy of this extended GO method the first problem considered in this section was again solved. Since all of the segments have exactly a radial orientation so that the segments are colinear with the ray path, the special geometry is recognized. Ray path components of the E-fields are then included in the hybrid program like parallel components as described above. The new solutions are shown in Figures 40a and b. The good agreement demonstrates the validity of the method of extending GO at least for large A.

A second method for extending GO or handling this special case where GO does not give answers is also possible. Again, assuming the special case has been recognized, the problem segment could be perturbed in orientation to be slightly off the ray path
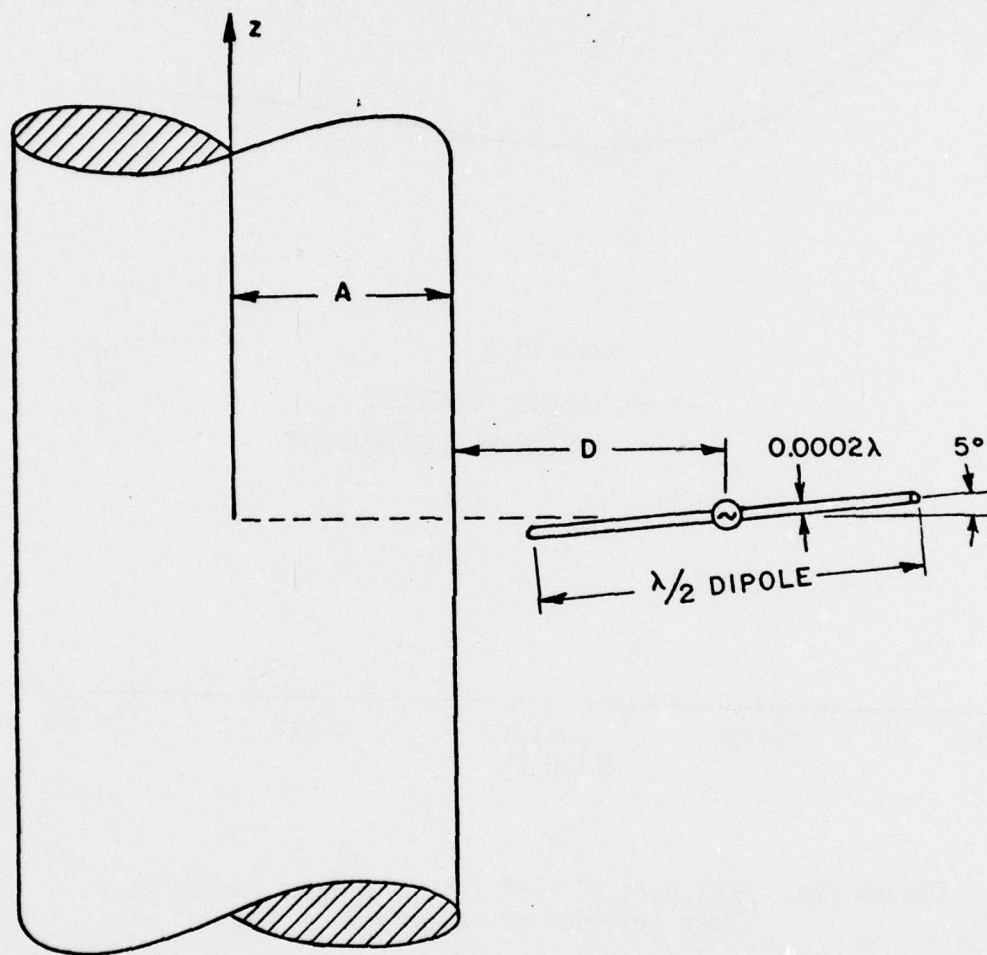
88

Figure 38. Geometry for a radial dipole tilted 5°.

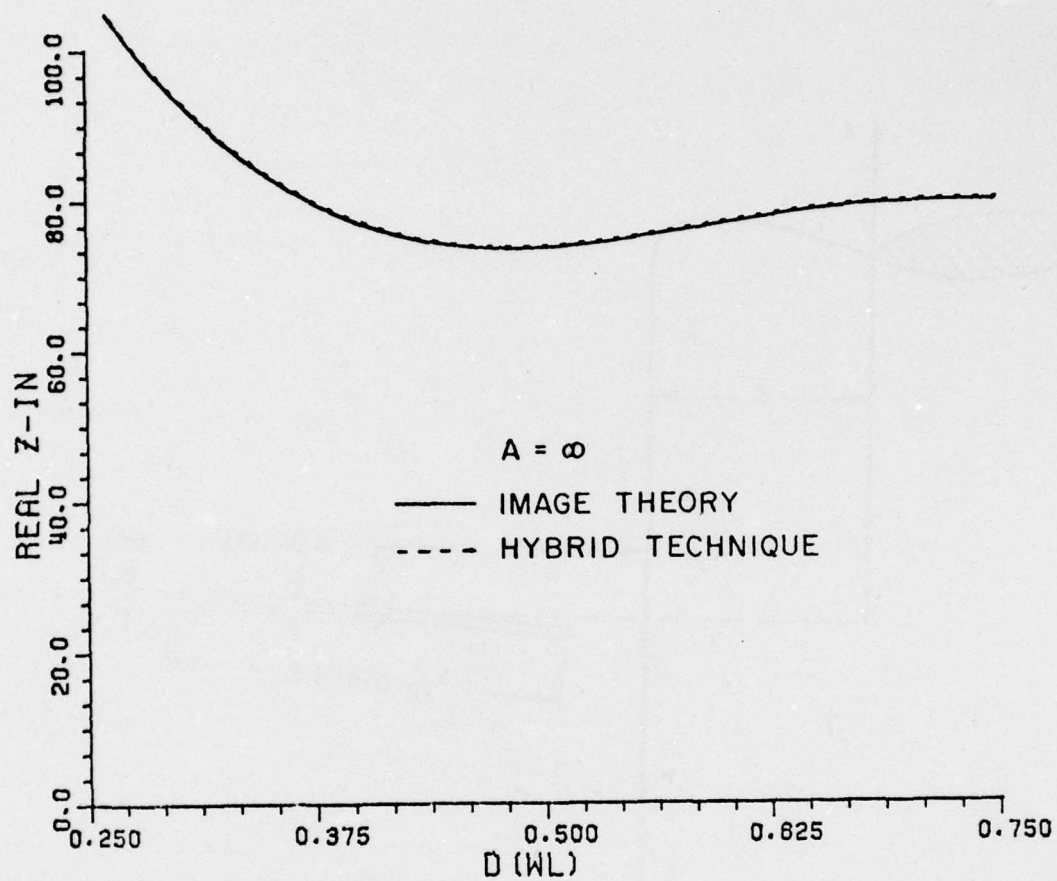Figure 39a. Real part of radial dipole input impedance
near cylinder of radius A=∞.

90
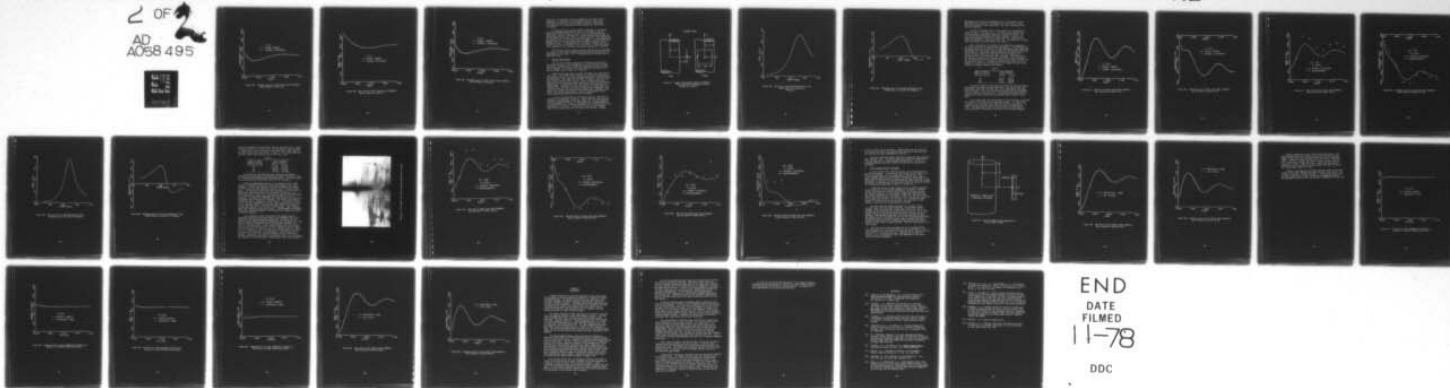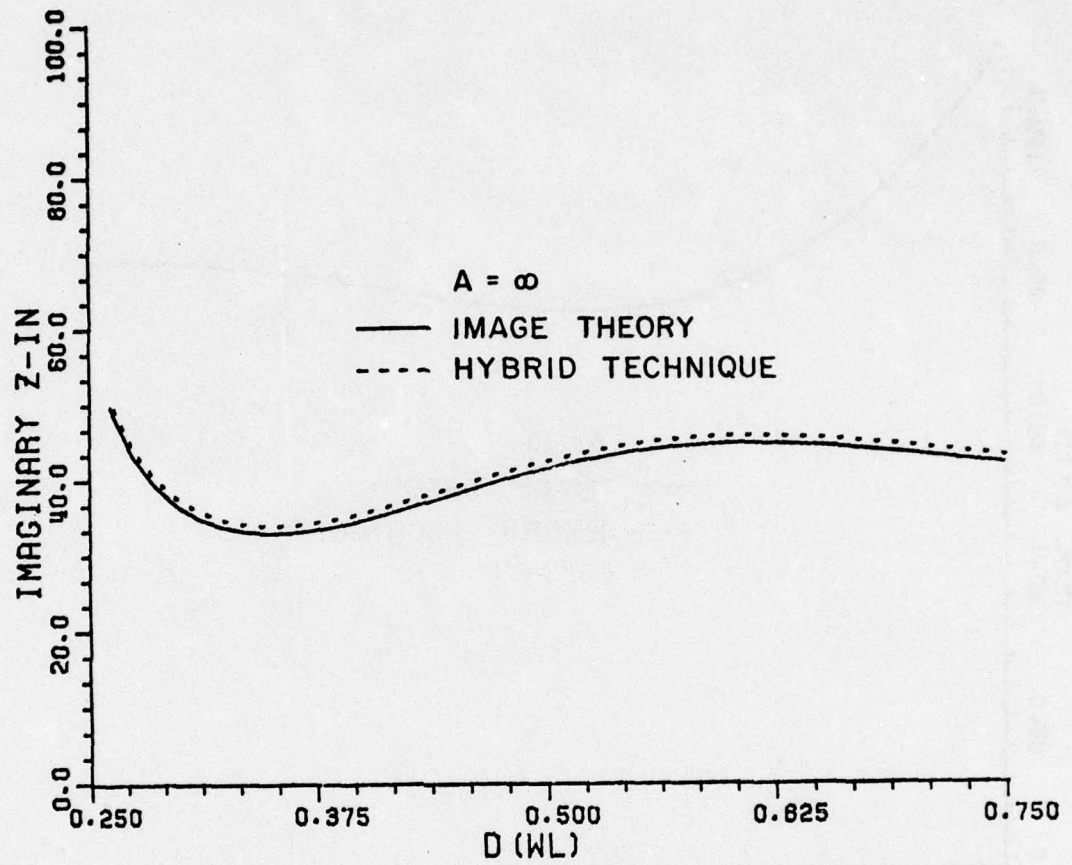
Figure 39b.   Imaginary part of radial dipole input impedance near cylinder of radius A≈∞.
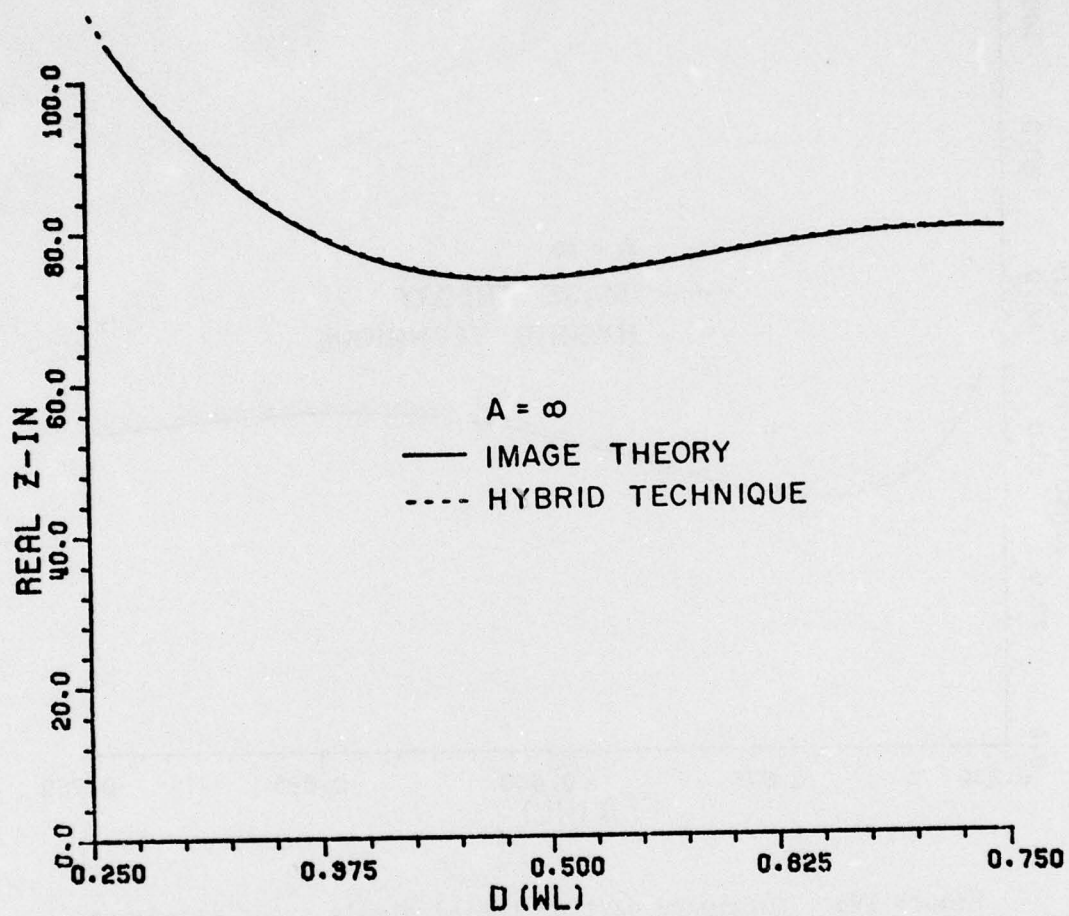
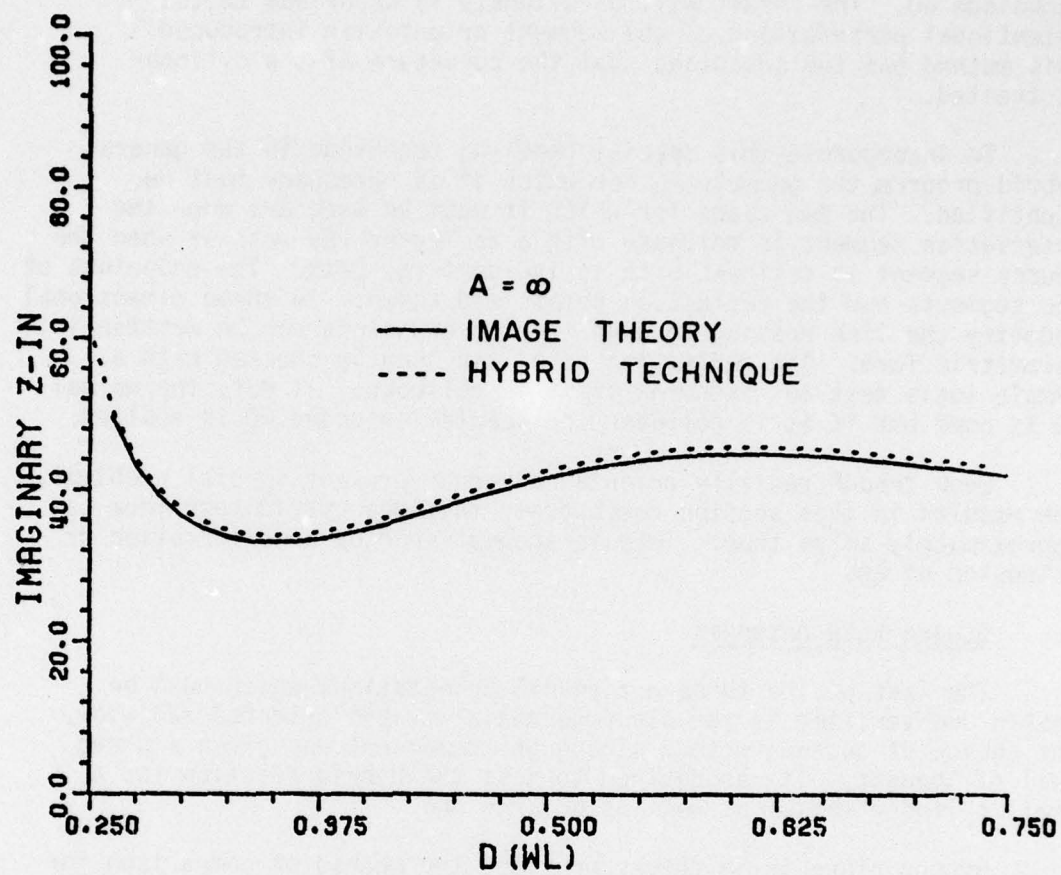Figure 40a. Real part of radial dipole input impedance
near cylinder of radius A=∞.

92

Figure 40b. Imaginary part of radial dipole input impedance near cylinder of radius A=∞.

93

direction. The geometry can now be handled by the normal hybrid technique GO. The result will be slightly in error due to the intentional perturbation of the segment orientation introduced. This method has the advantage that the curvature of the cylinder is treated.

To incorporate this special handling technique in the general hybrid program, the geometries for which it is necessary must be identified. The two cases for which it must be used are when the observation segment is colinear with a reflected ray path or when the source segment is colinear with an incident ray path. The endpoints of the segments and the reflection points are known. In three dimensional geometry the line passing through the two endpoints can be written in parametric form. The reflection point can then be checked with a simple logic test to determine if it is colinear. If not, the normal GO is used but if it is colinear the special extended GO is applied.

Even though radially oriented antennas present special problems, the results in this section demonstrate that the hybrid technique can approximately solve them. This is accomplished by a modification or extension of GO.

C. Square Loop Antennas

The last of the three orthogonal orientations which must be tested and verified is the circumferential or phi oriented radiator. The choice of antenna with a strong phi component was given a great deal of thought. It was desired to test the hybrid solution for a small cylinder radius as well as a large one.

Ground plane image theory provides the method of comparison for large radii. No antenna with an analytical solution was found when the radius was small. One which allowed experimental verification was then desirable. The square loop oriented as shown in Figure 41 near the circular cylinder fits the bill. The x-y plane cutting the geometry gives the necessary image symmetry to eliminate the balanced feed problem. A square half-loop and cylinder can be mounted on a ground plane. The square loop has one half of its extent almost phi oriented giving the required strong circumferential components. The square loop antenna was examined quite extensively by Richards [14]. Some of his results were used as a check on the programs of this section before the cylinder effects were included.

A look at the admittance of the square loop as a function of frequency in wavelengths is useful. Figures 42a and b show the conductance and susceptance of the square loop for a varying frequency. The wire diameter of the loop is one-eighth inch in anticipation of the experimental loop. The loop perimeter was 10 inches making it one wavelength at 1.1811 GHz. The vertical scales are in mill-mhos. These curves agree quite well with results by Richards. Maximum
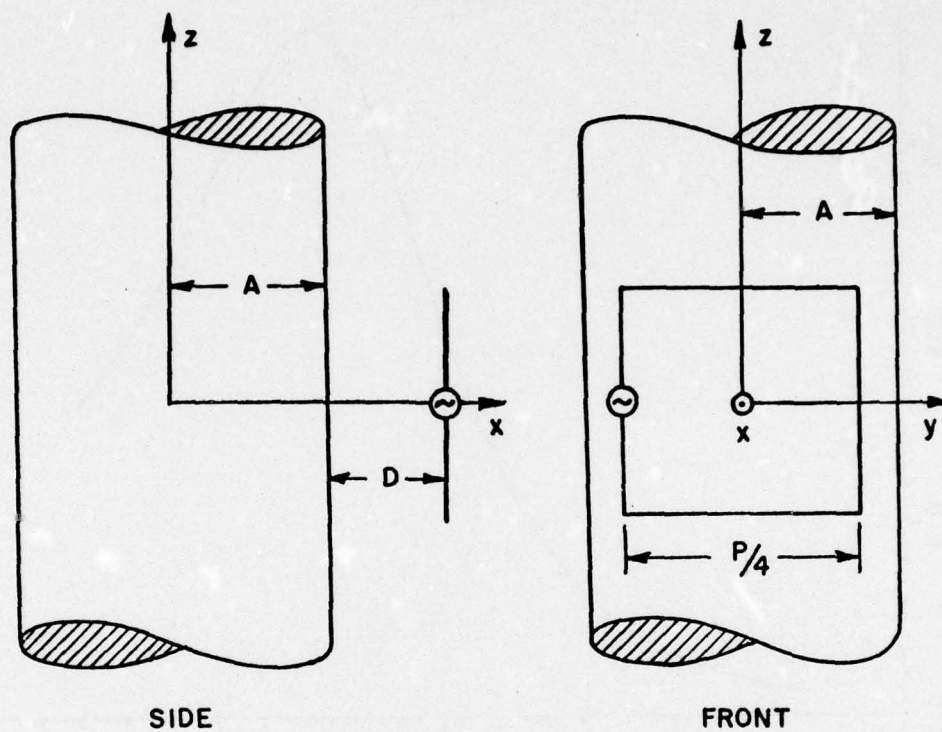
94

SQUARE LOOP

SIDE   FRONT

Figure 41. Square loop antenna located a distance D
from a perfectly conducting circular
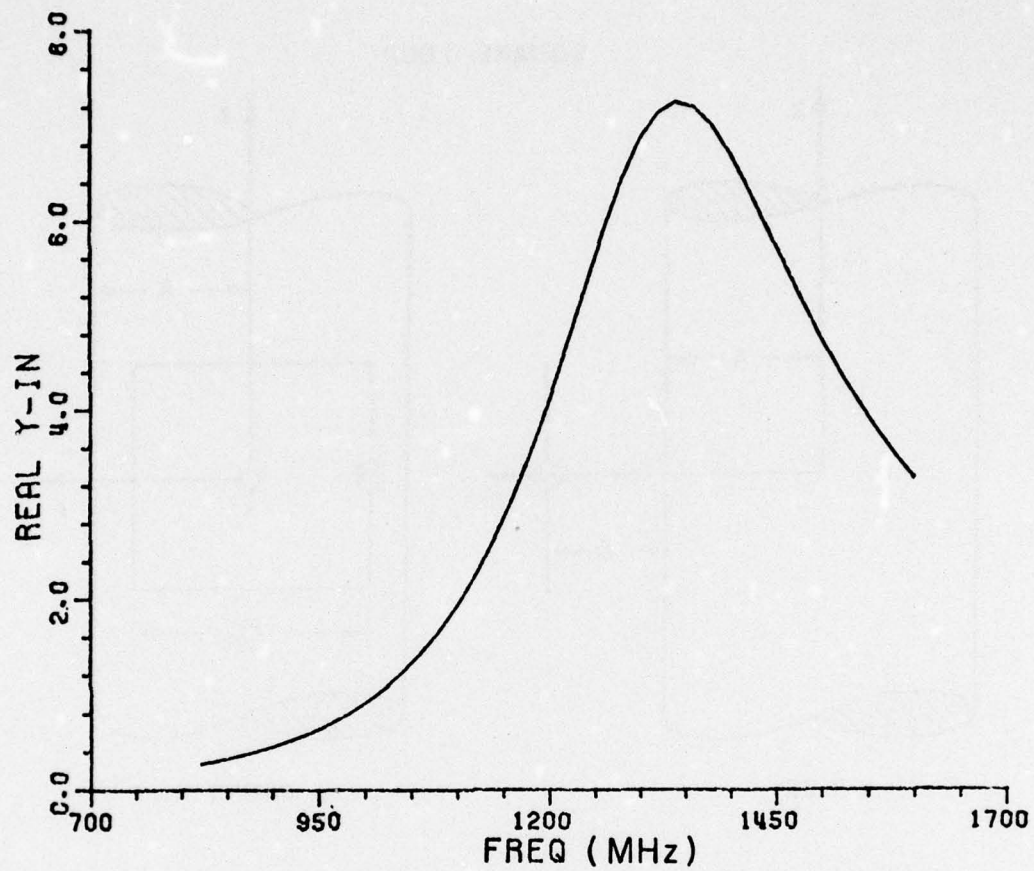cylinder of radius A.

95

Figure 42a. Real part of the input admittance of the
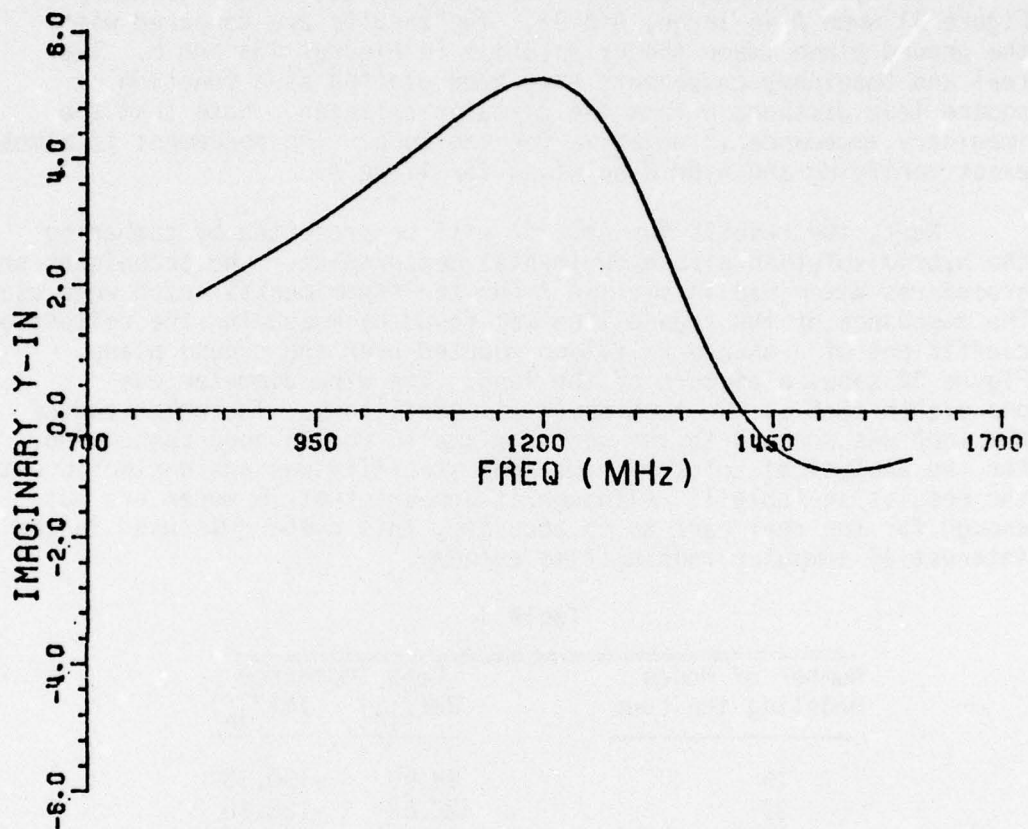square loop as a function of
frequency.

96

Figure 42b.   Imaginary part of the input admittance of the
square loop as a function of frequency.

97

admittance will give minimum impedance which is desirable so that the antenna will radiate. The frequency of 1.1811 GHz is chosen where the perimeter is one wavelength. The loop's dimensions have now been specified.

The hybrid technique will first be applied to the geometry of Figure 41 when A is large, $A=5.0\lambda$. The results are compared with the ground plane image theory solution in Figures 43a and b. The real and imaginary components have been plotted as a function of square loop distance D from the circular cylinder. Note that the imaginary impedance is negative for the loop. The agreement is almost exact verifying the hybrid solution for large A.

Next, the results for $A=0.25\lambda$ will be presented by comparing the hybrid solution with experimental measurement. The techniques and procedures described in section A for the experimental setup were used. The impedance of the square loop was found by measuring the reflection coefficient of a square half-loop mounted over the ground plane. Figure 32 shows a picture of the loop. The wire diameter was one-eighth inch so the feed point was continuous. The other end of the loop was screwed to the ground plane to make a good connection. For the analytical solution, the mode stability was again studied with the results in Table 1. Although it appears that 16 modes are not enough for the real part to be accurate, this number was used in the interest of computer running time economy.

Table 1

Number of Modes Modeling the Loop	Loop Impedance	
	$Re(Z_{in})$	$Im(Z_{in})$
16	88.93	-130.35
32	82.62	-128.66
48	77.41	-128.09

The results comparing the hybrid technique with the experimental measurements are shown in Figures 44a and b. The curves track the measurements quite well but the levels are shifted making the number values disagree. This level shift was disturbing when the remarkable results of Section A were recalled. No equivalent reasoning such as adjusting the dipole length for end effects could be found for the loop.

It was postulated that the thickness of the wire might be causing the corners of the loop to be inadequately modeled. To check this, a loop with wire thickness four times smaller was investigated. All dimensions were the same except the thin loops wire diameter was 1/32". The admittance curves for the thin loop case are shown in Figures 45a and b. Note that 1.1811 GHz is still a good frequency
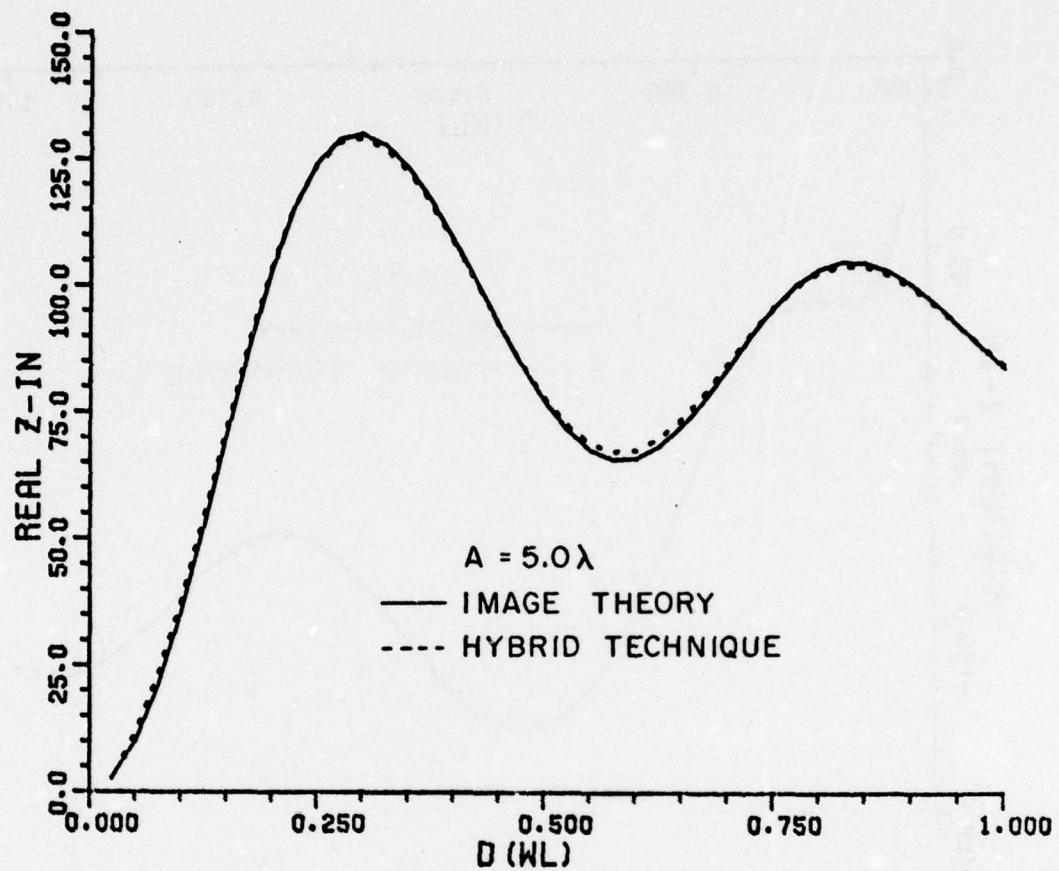
98

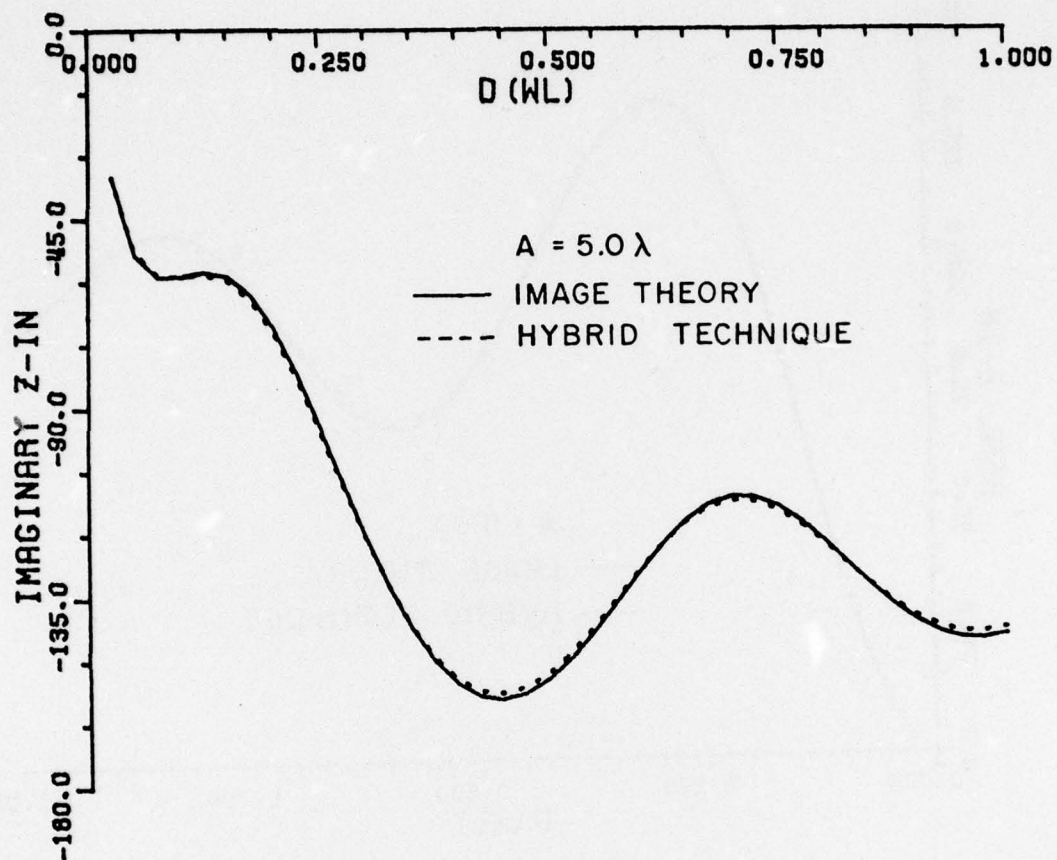Figure 43a.   Real part of square loop input impedance
near cylinder of radius A=5.0λ.

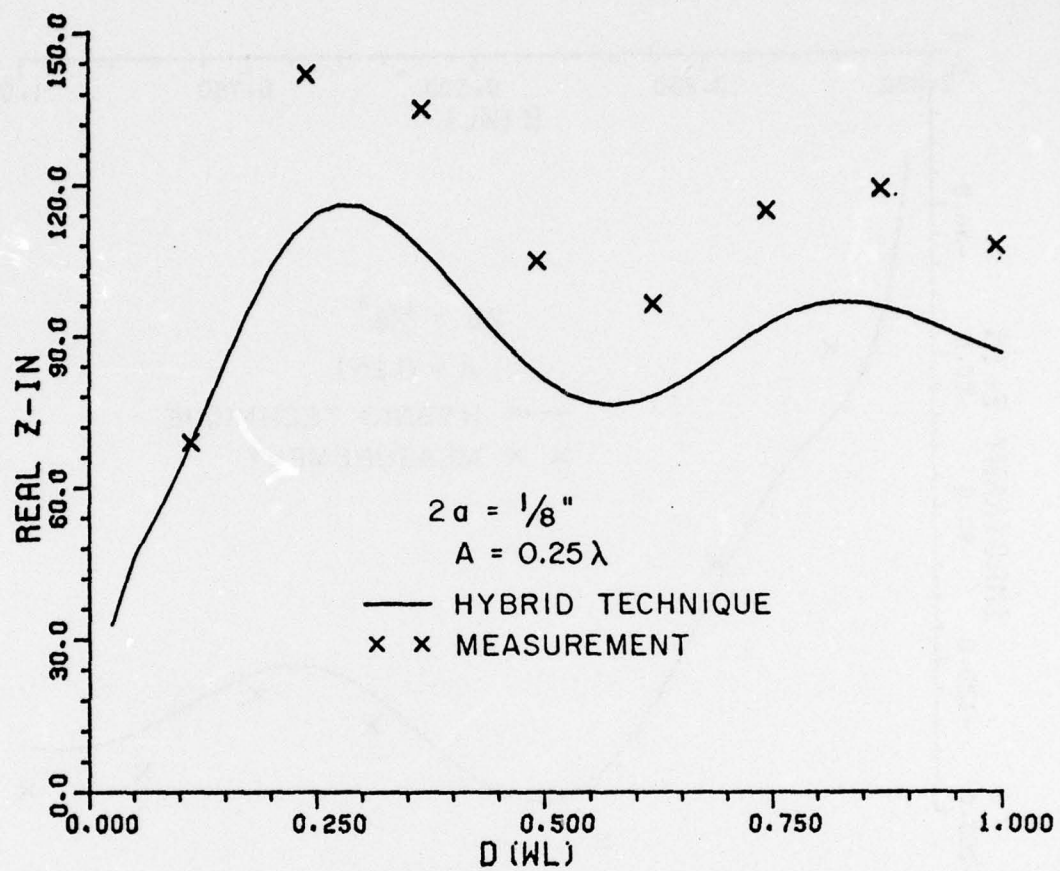Figure 43b. Imaginary part of square loop input impedance near cylinder of radius A=5.0λ.

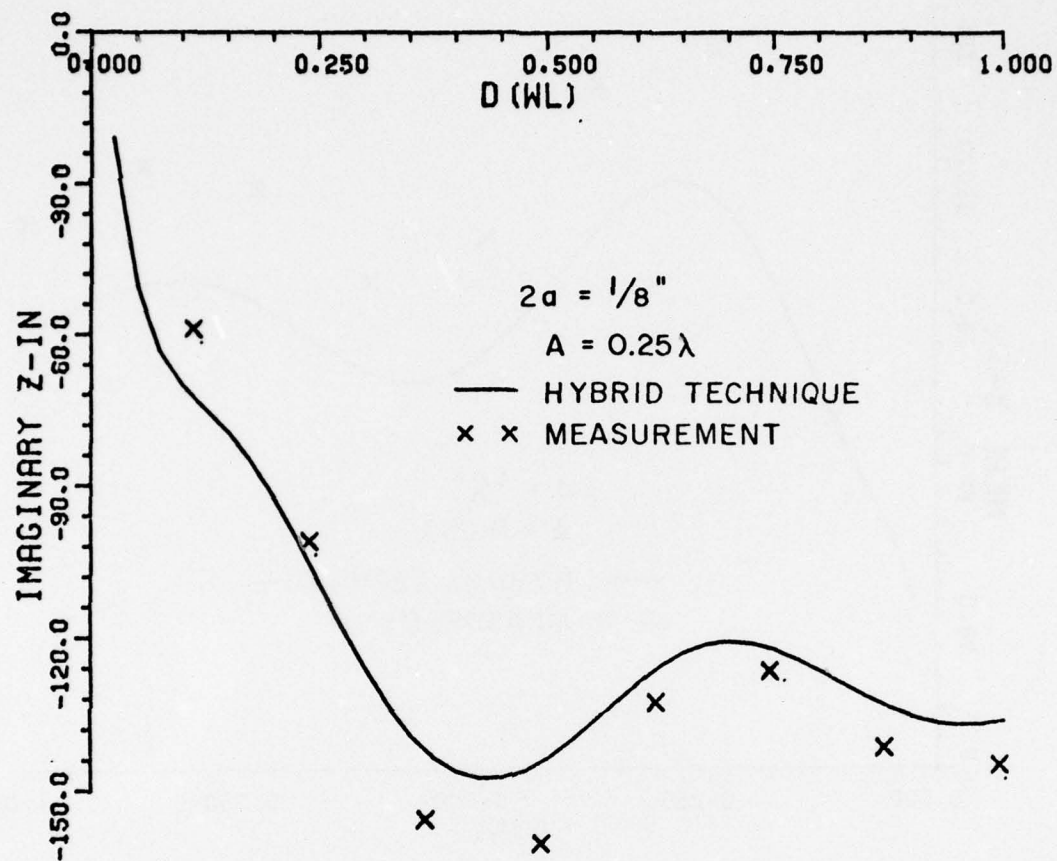Figure 44a. Real part of square loop input impedance near cylinder of radius A=0.25λ.

101

Figure 44b. Imaginary part of square loop input impedance near cylinder of radius A=0.25λ.
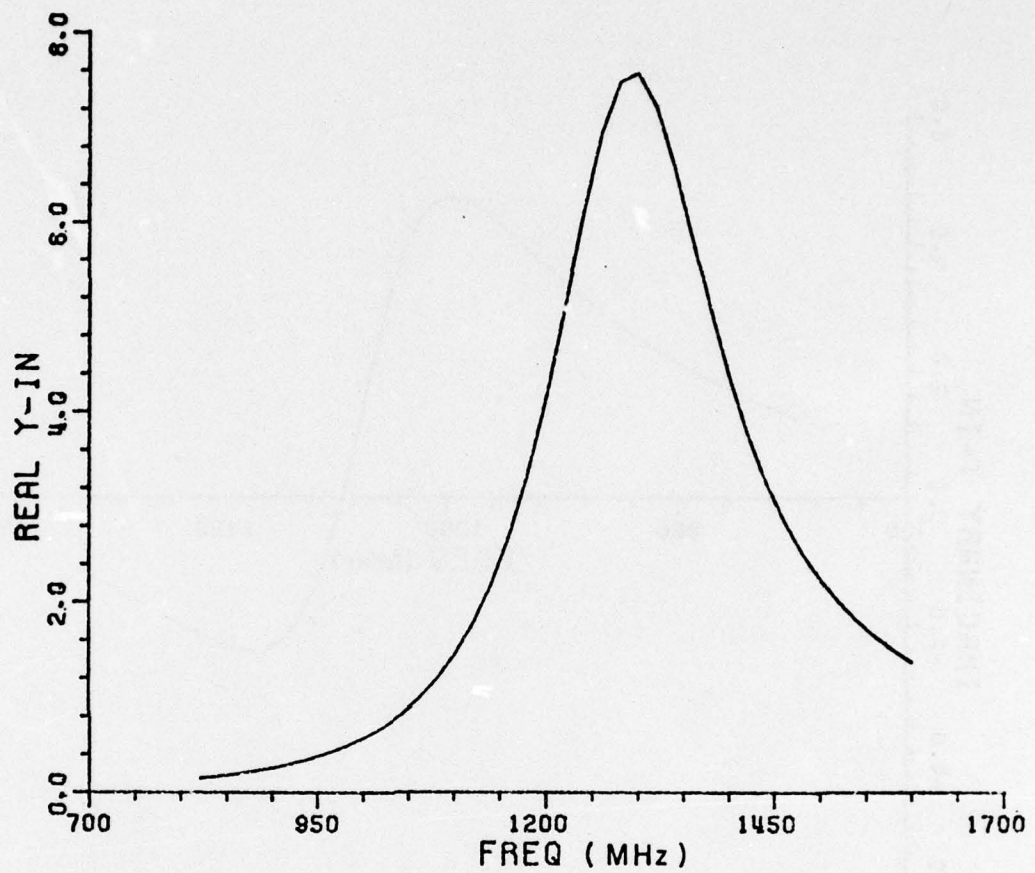
Figure 45a. Real part of the input admittance of the
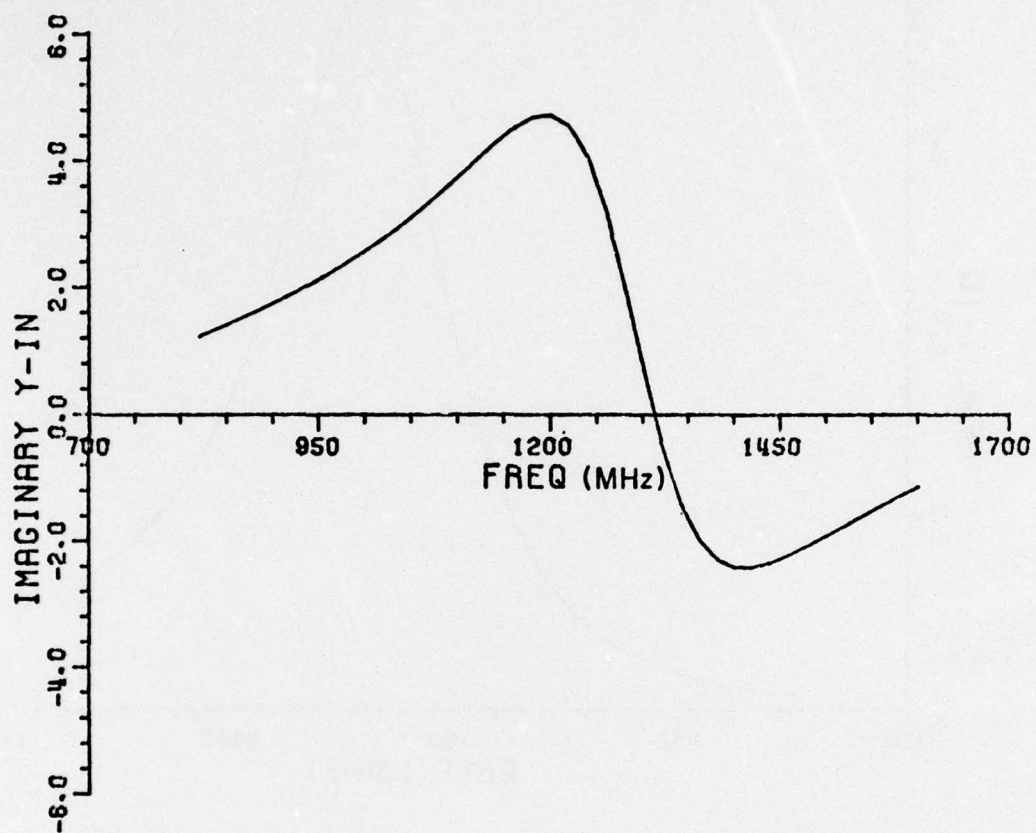square loop as a function of frequency.

103

Figure 45b. Imaginary part of the input admittance of the square loop as a function of frequency.

104

choice and resonance is much sharper than for the thick loop. Figure 46 shows a picture of the thin loop. The end opposite the feed point is soldered to a brass screw set in the ground plane. Mode stability was again studied with the results in Table 2. The sixteen modes for the thin loop is more accurate than for the thick loop.

Table 2

Number of Modes Modeling the Loop	Input Impedance	
	$Re(Z_{in})$	$Im(Z_{in})$
16	101.255	-139.802
32	99.379	-139.315
48	98.454	-139.199

The results for the thin loop case, comparing the hybrid technique with experimental measurements are shown in Figures 47a and b. The postulated improvement did not materialize. The curves, again, track the points well but a level shift is still apparent.

During the measurement process it was observed that a slight change in frequency resulted in a significant change in the input impedance. This follows logically from the admittance curves where it can be seen that the operating frequency is at a rapidly varying point. The inability to get exact level agreement is at least partly explained by the sensitivity at the frequency of operation. An attempt was made to avoid this problem by carrying out the measurements at a frequency low enough to be away from the sensitivities of resonance. A frequency of 885.8 MHz was chosen which can be seen from Figures 45a and b to be well off resonance. The results are shown in Figures 48a and b. Agreement is quite erratic. The problem is that Z_{in} for this off resonance case is very large compared with the $Z_0 = 50\Omega$ of the connecting cable. The mismatch causes much of the energy to reflect back down the line and very little radiates. Small radiation means weak interaction with the cylinder. The measurement environment is too noisy and the equipment is too inaccurate to measure this weak interaction properly.

In an attempt to further investigate the problems around resonance by measuring free space loop's input impedance over a frequency band the real problem was discovered. The section of line connecting the antenna to the s-parameter device is assumed to be ideal. Only its length is compensated for by setting the reference to a short at the antenna port. It was found, however, that this section of line which was constructed of a group of connectors was not ideal. Different connectors of the same type gave different amounts of phase shift. The amount of change in phase was also dependent on how much the antenna was radiating. Correspondingly, it was frequency dependent. Physically, the difference probably resulted from the discontinuities where the connectors touched being unique to each connector. The solution of the problem would involve using a more ideal connector
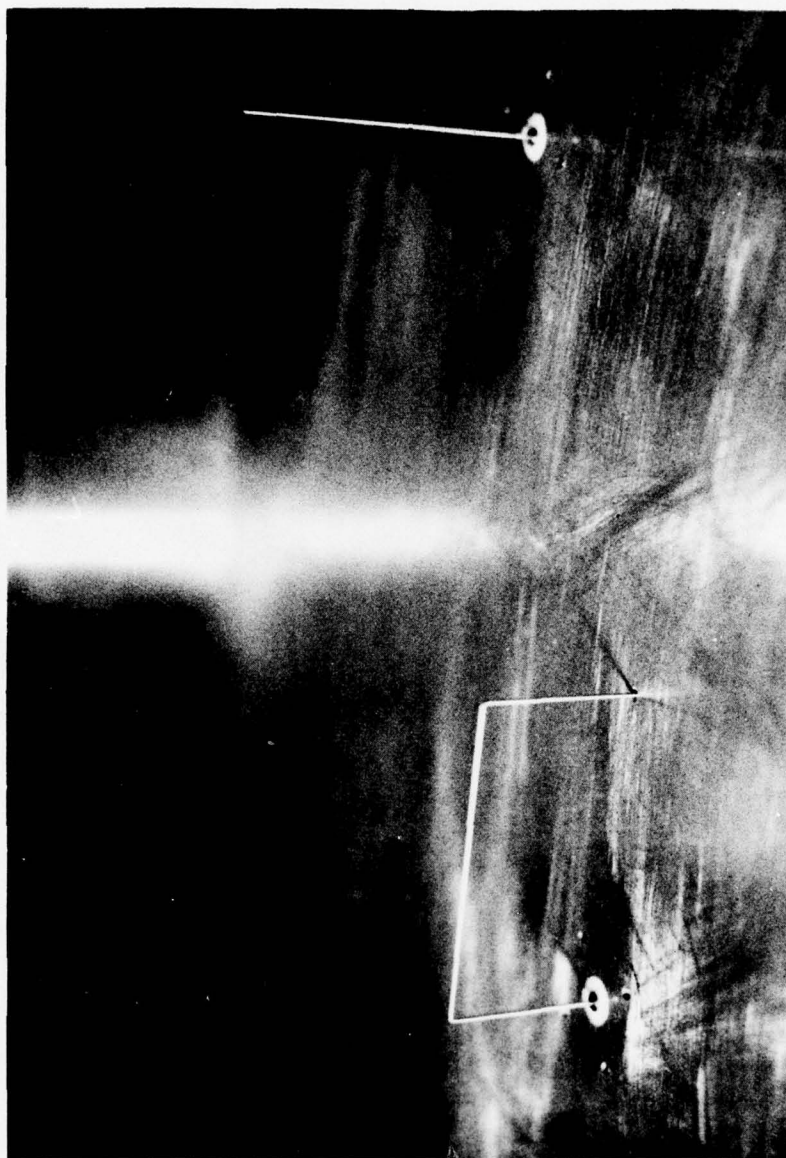
105

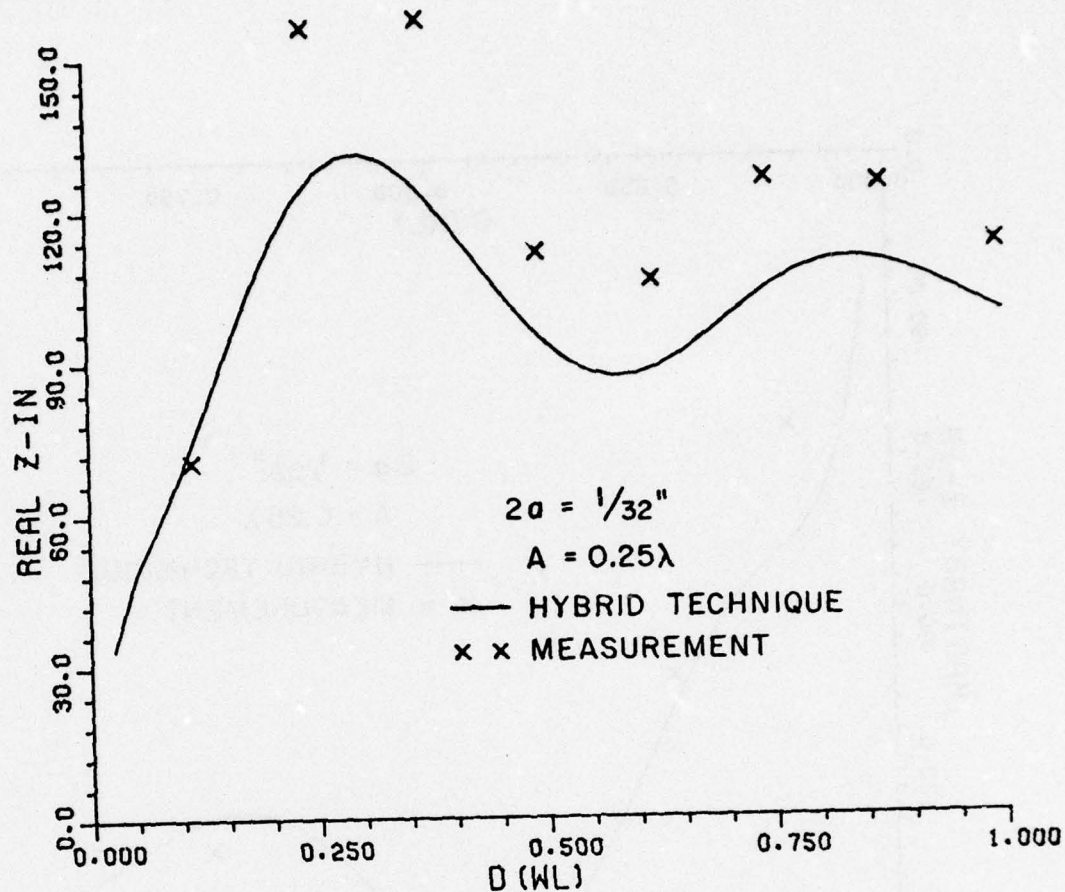Figure 46. Thin square half-loop on ground plane near cylinder.

106

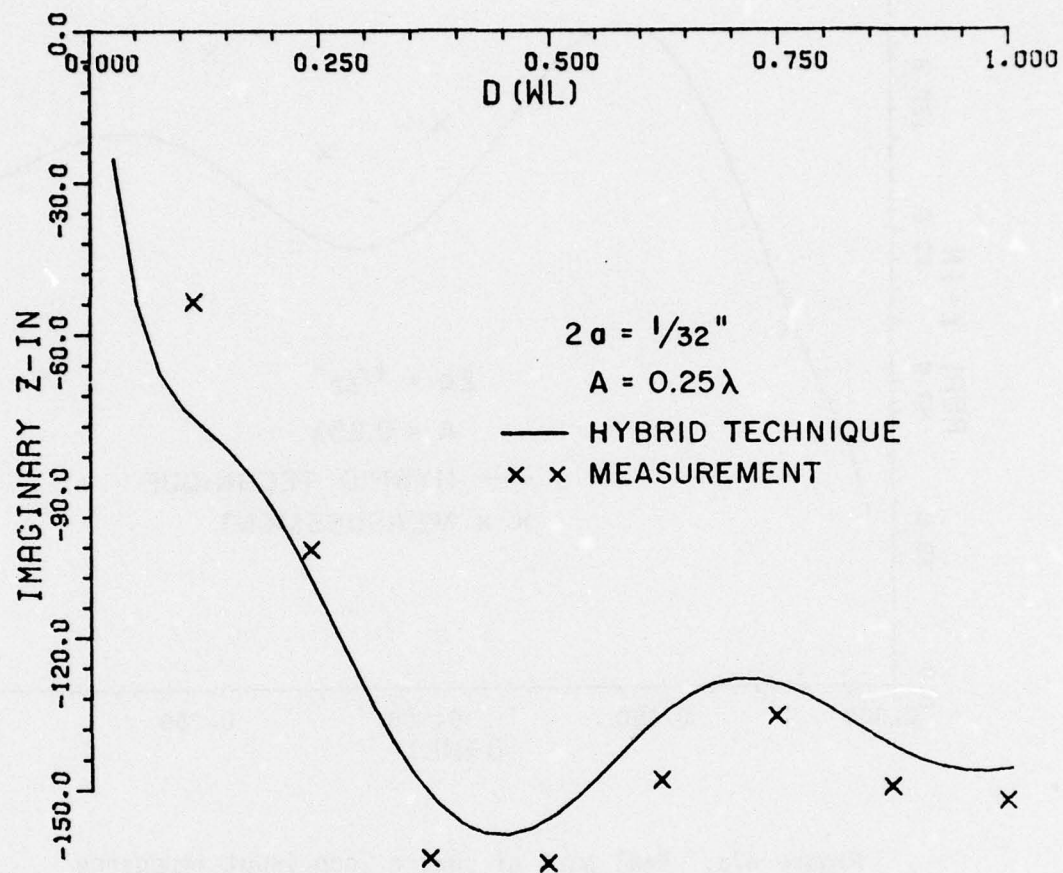Figure 47a. Real part of square loop input impedance near cylinder of radius A=0.25λ.

Figure 47b.   Imaginary part of square loop input impedance
near cylinder of radius A=0.25λ.

108

REAL Z-IN

150.0

120.0

90.0

60.0

30.0

0.0

0.000   0.188   0.375   0.563   0.750

D (WL)

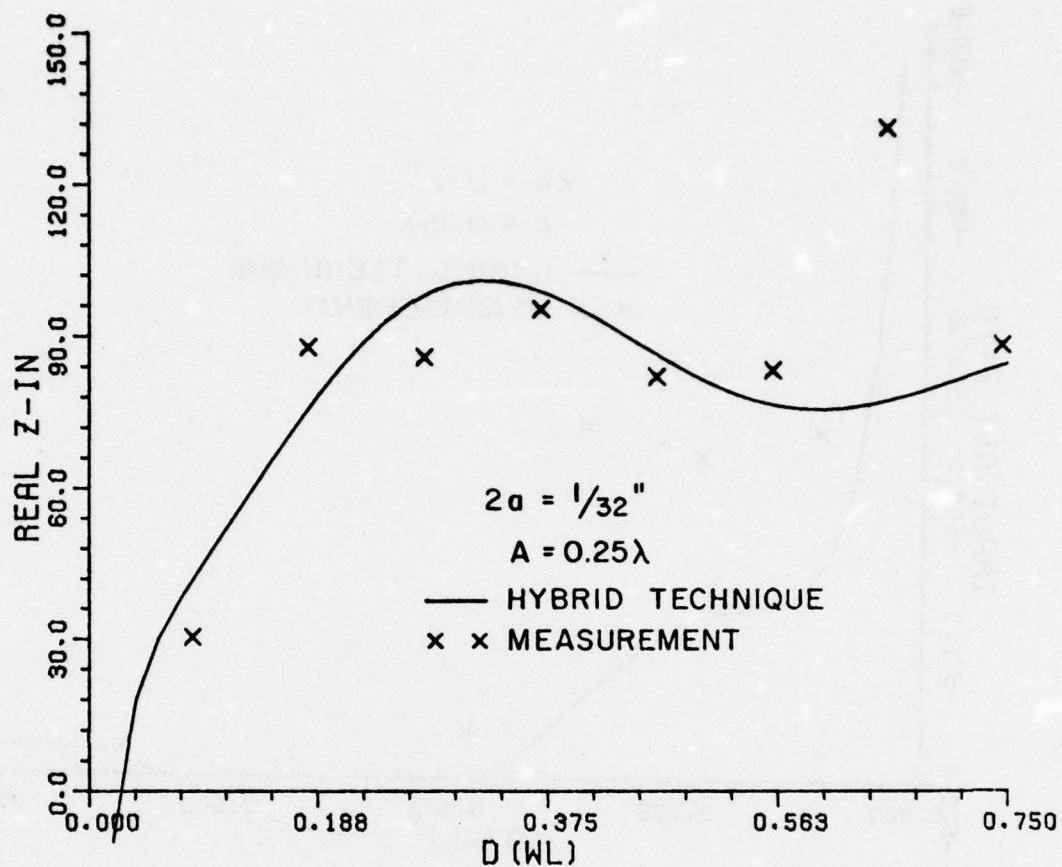2a = ¹/₃₂"

A = 0.25λ

—— HYBRID TECHNIQUE

× × MEASUREMENT

Figure 48a.   Real part of square loop input impedance
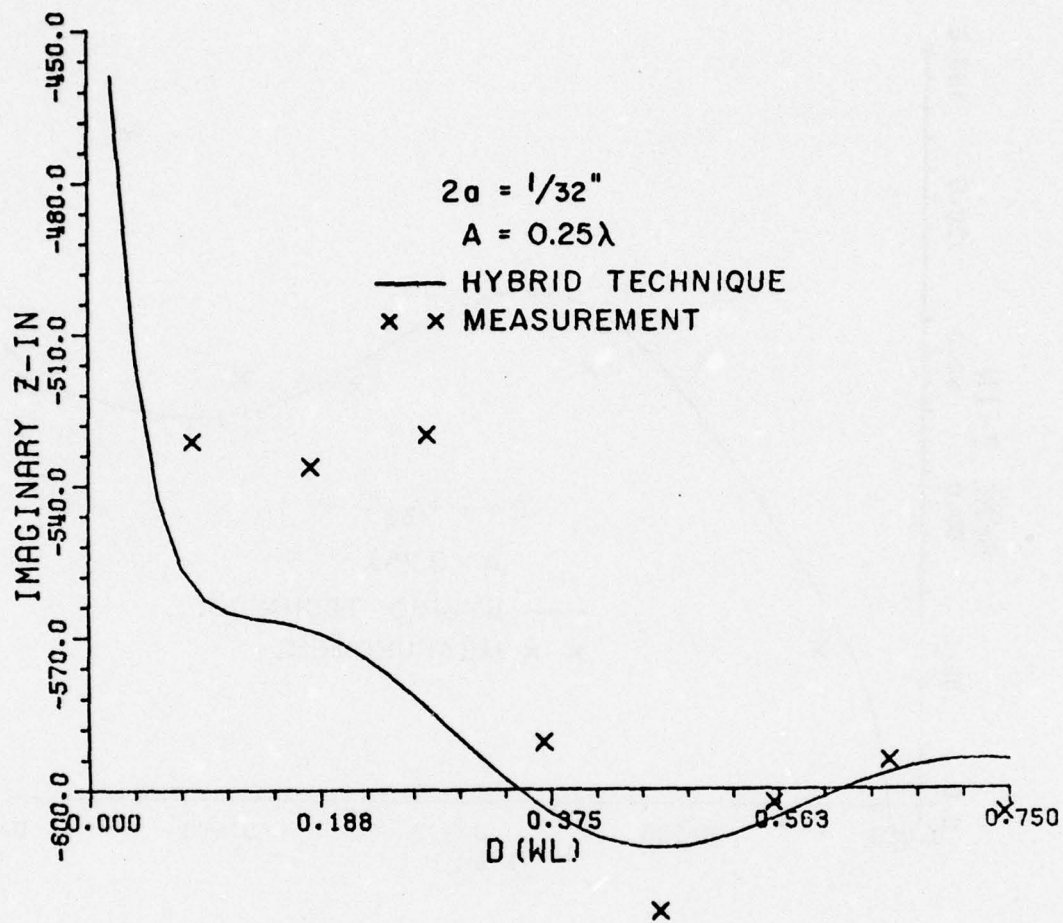near cylinder of radius A=0.25λ.

109

Figure 48b.   Imaginary part of square loop input impedance
near cylinder of radius A=0.25λ.

110

in this critical part of the setup. Remeasurement was not necessary here because the results already show that the hybrid technique works very well and has been experimentally verified.

Thus, phi oriented radiators have been checked for both large and small cylinder radii. The hybrid technique has now been demonstrated to be accurate for all three orthogonal orientations. Its use on arbitrary radiators near the circular cylinder can now proceed with confidence.

D.   Finite Length Circular Cylinders

In this section finite length cylinders will be handled using the hybrid technique. To account for the finite cylinder length, the GTD for curved edges is used as described in Chapter II to find delta impedance matrices as described in Chapter III which properly modify the free space matrix to include the cylinder end effects. The formulation of the part of the hybrid technique which finds the cylinder end effects is modeled after the part which finds the reflection effect. The formulation was described in detail in Chapter III.

To test the finite cylinder capability of the hybrid technique, it was applied to find the input impedance of an axially oriented dipole. One reason for picking this radiator orientation was that the diffraction points on the cylinder's edges were known directly. The problem's geometry is illustrated in Figure 49. The diffraction points are on the cylinder's end edges in the x-z plane with x positive. The cylinder half height is CH, its radius is A, and the half-wave dipole is a distance D from the cylinder. For the cases in this section, A will be fixed at one-quarter wavelength.

The only analytical method available for solving a finite cylinder, other than the hybrid technique, is the moment method. Computer limits on storage and running time prohibit its use on a cylinder as electrically large as the case to be solved. So no independent method is available to check the hybrid solution for this geometry. Experimental measurement will prove impossible because the effects of the finite ends will be too small to measure accurately. The method chosen to verify the results was to compare the hybrid method solution of the finite length cylinder case with the hybrid solution of the infinite length cylinder. Intuitive observations will then be made.

The first results to be presented are for a cylinder height CH=0.375λ where D is varied from near zero to one wavelength. The input impedance plots are given in Figures 50a and b. The solid curves are for an infinite length cylinder. Chopping the cylinder off creates a small perturbation in the input impedance of the dipole. This result seems reasonable.
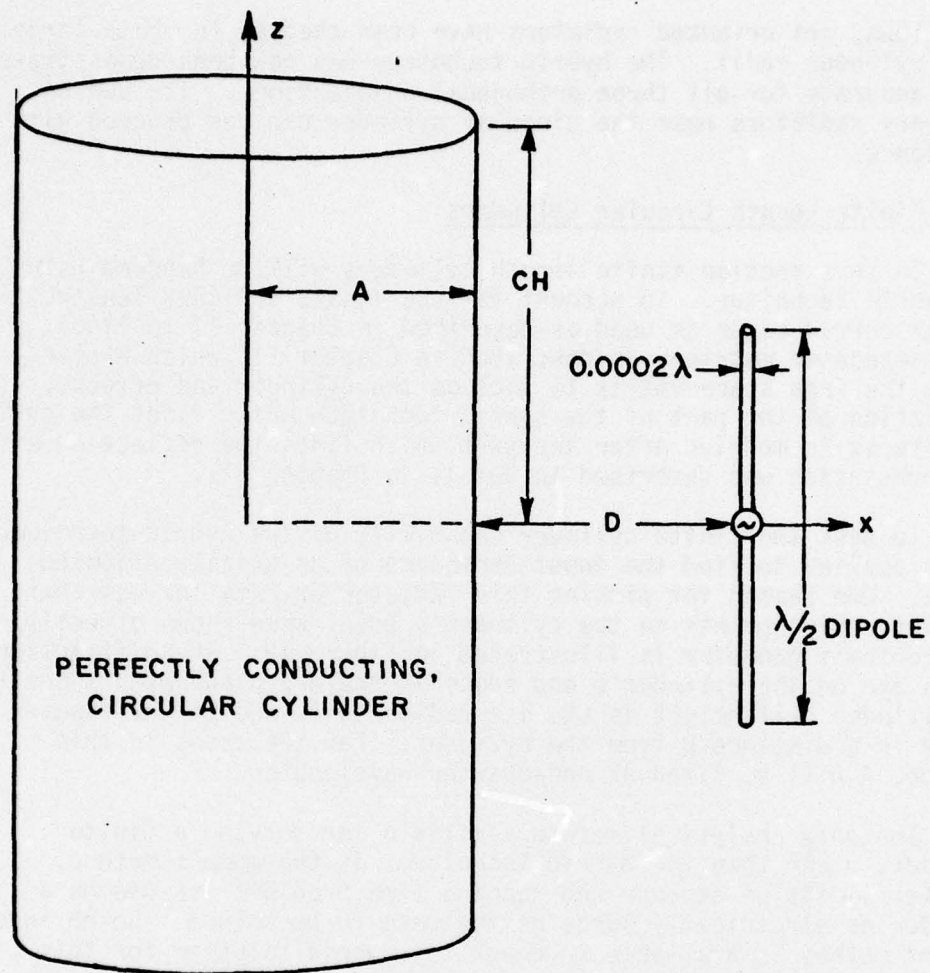
111

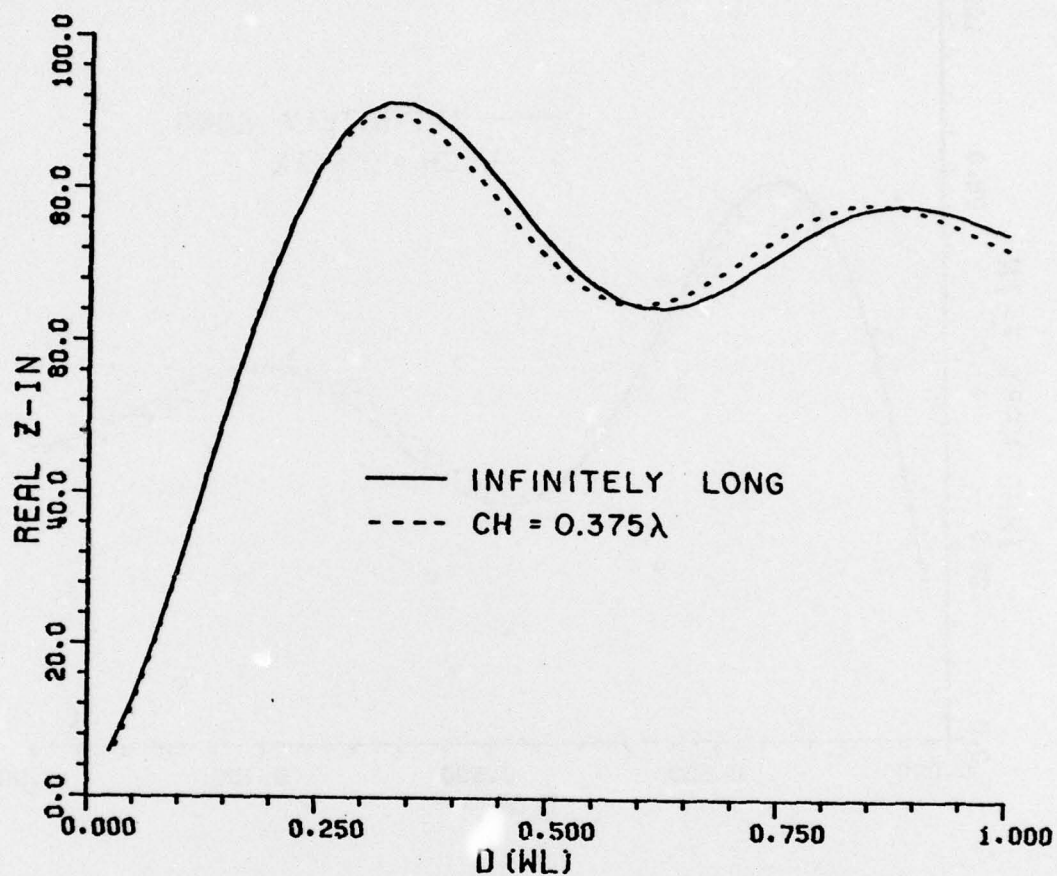Figure 49. Axial half-wave dipole located near a
finite length cylinder.

Figure 50a. Real part of axial dipole input impedance
near cylinder of radius A=0.25λ.

113

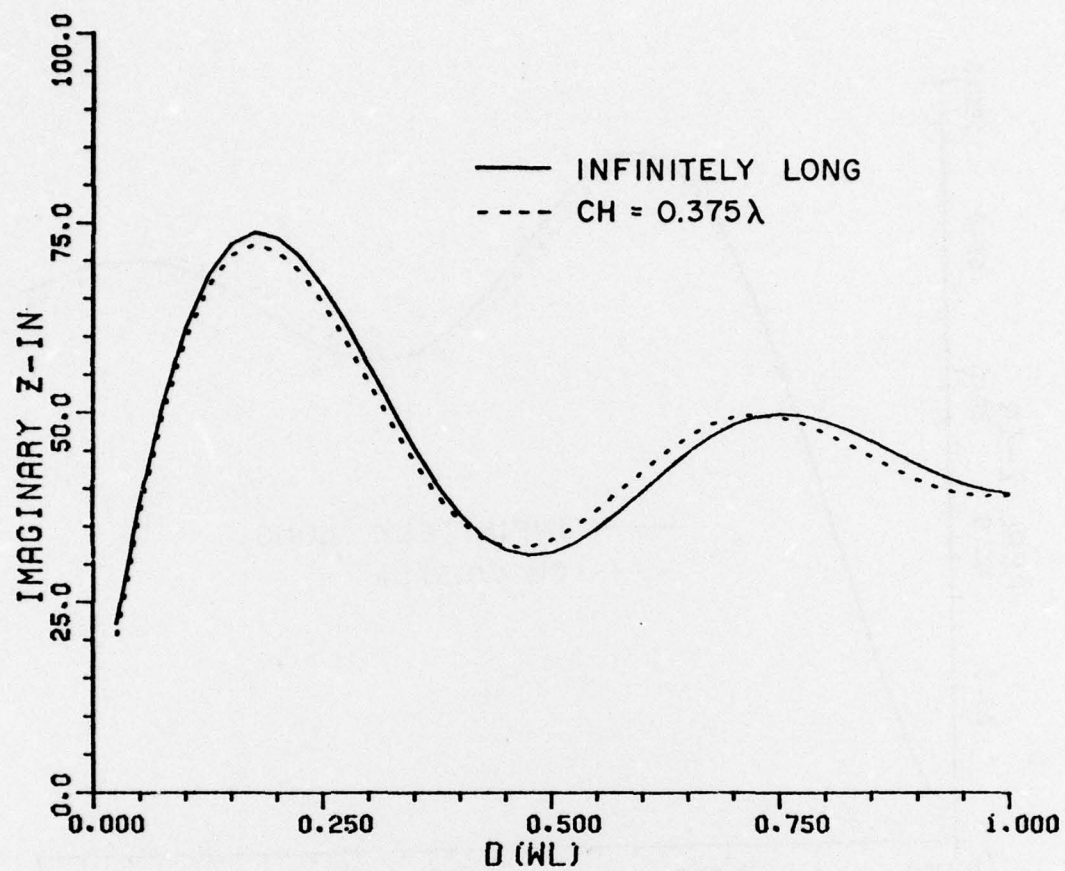Figure 50b. Imaginary part of axial dipole input impedance
near cylinder of radius A=0.25λ.

114

Another approach was tried to help verify the results. The dipole distance from the cylinder was held fixed and the cylinder height CH was varied from just above the dipole to one wavelength higher. Figures 51a and b show the results for D=0.3λ. The solid line is the finite cylinder case here. Figures 52a and b show the case D=0.6λ results. These two sets of figures are particularly convincing in that the effects of the cylinder ends fade to zero as the cylinder gets longer as it must.

Finally, from those curves another cylinder height CH=.45λ was picked and the input impedance was again found as D was varied. The results are plotted in Figures 53a and b. Although the hybrid finite cylinder solution has not been verified by an independent method, the reasonable results of this section lend confidence to the solution.

Figure 51a. Real part of input impedance of dipole as a
function of cylinder height above dipole.

116

Figure 51b. Imaginary part of input impedance of dipole as a
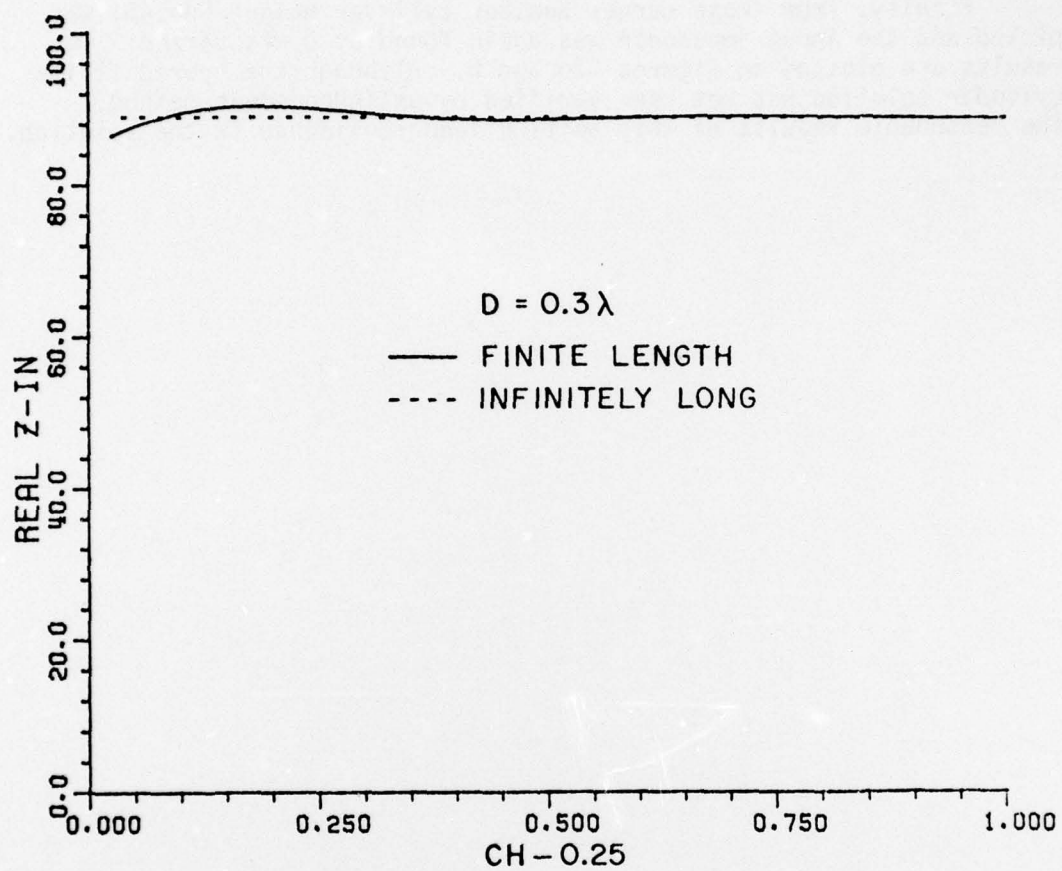function of cylinder height above dipole.

117

Figure 52a. Real part of input impedance of dipole as a
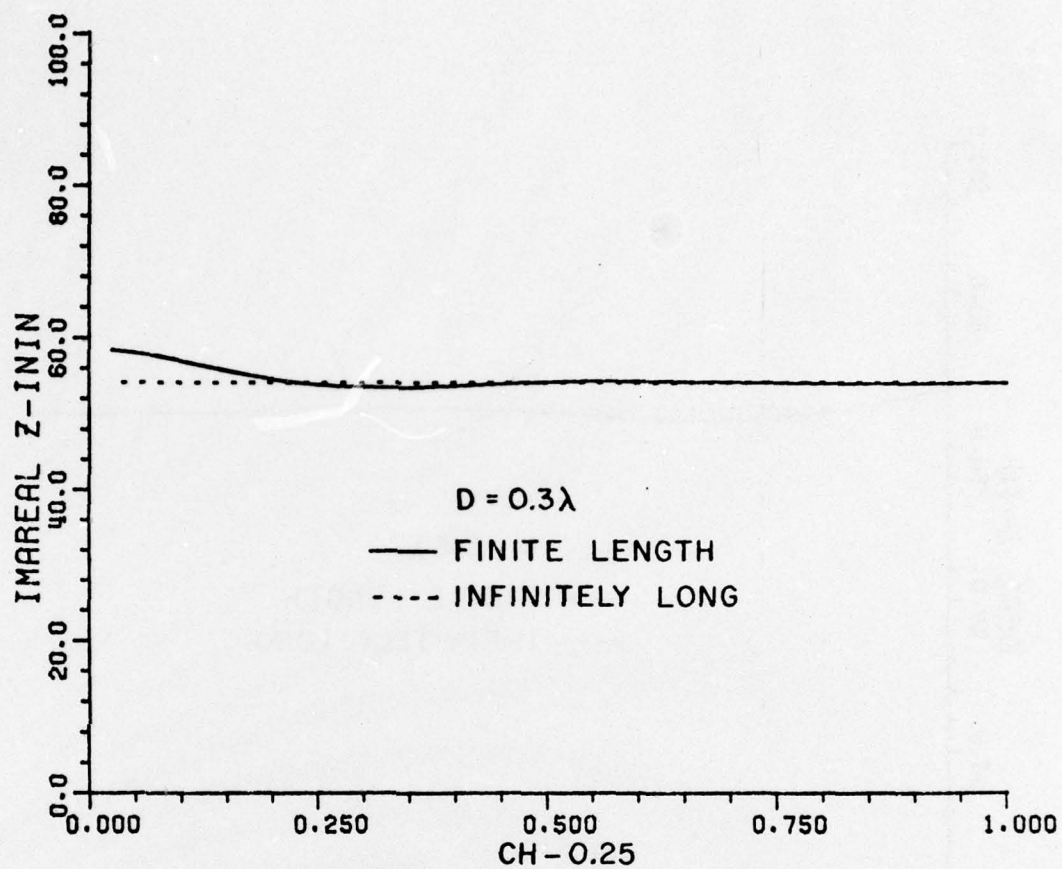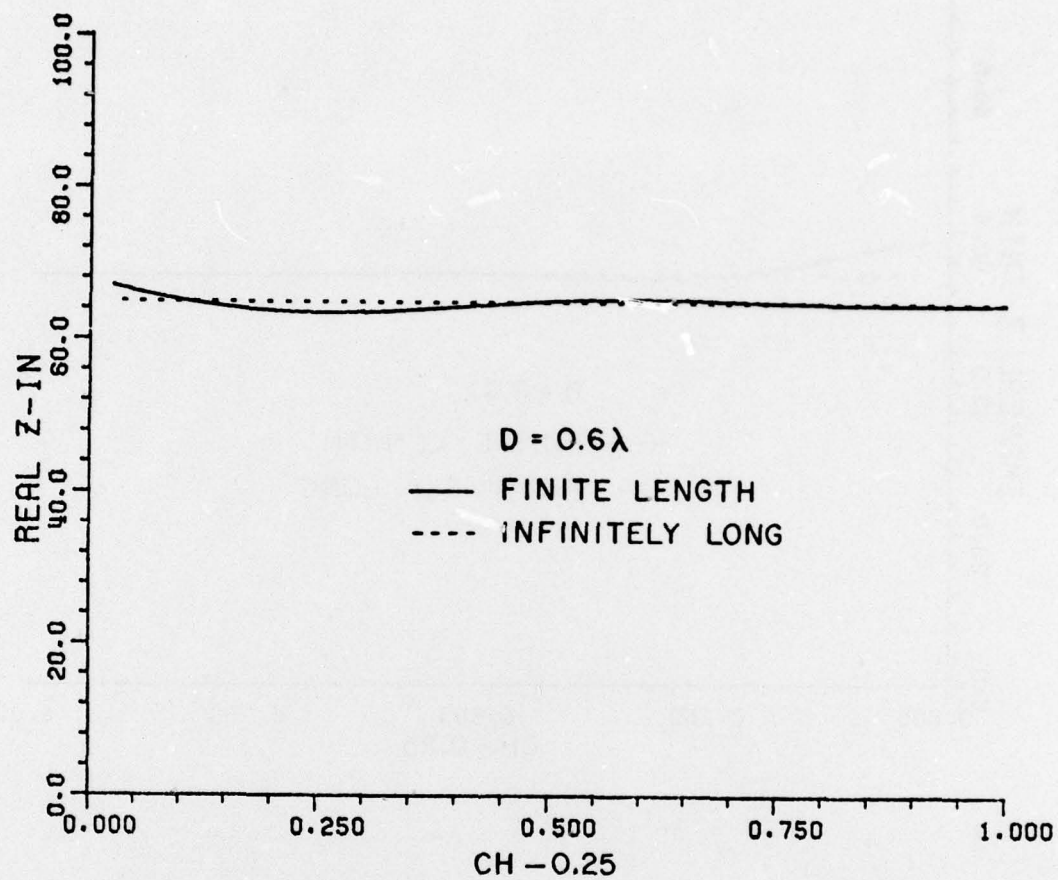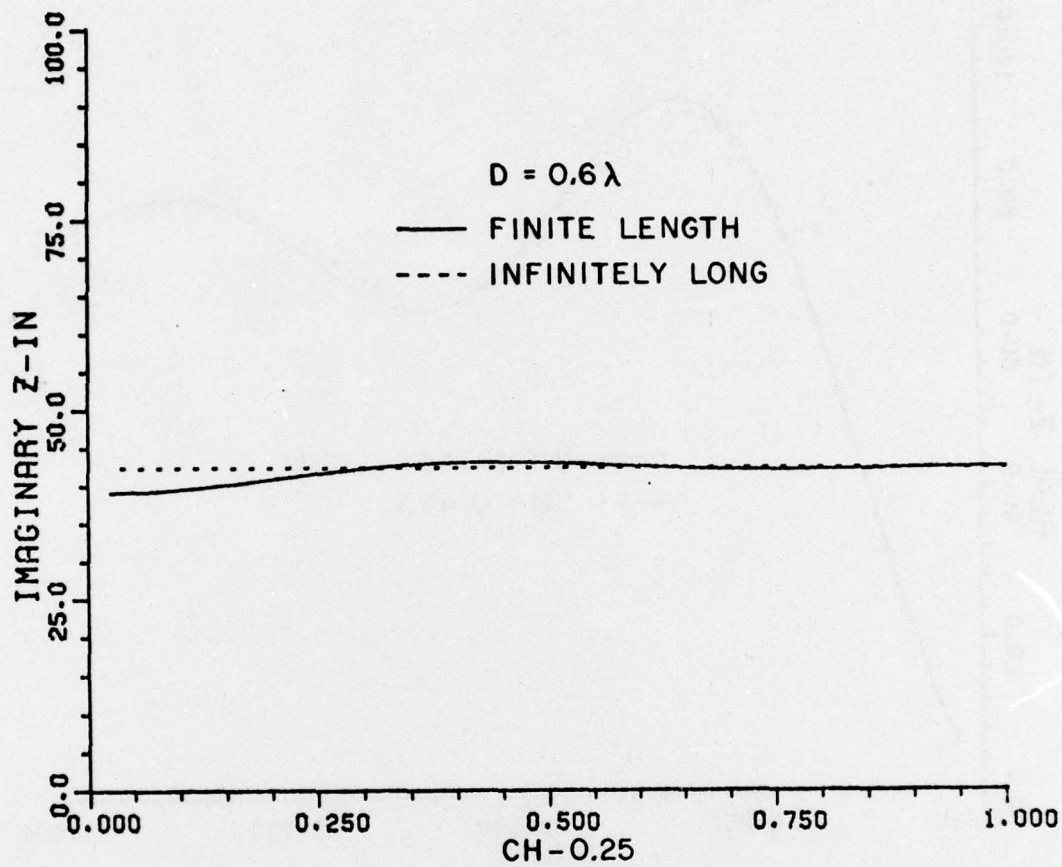function of cylinder height above dipole.

118

Figure 52b. Imaginary part of input impedance of dipole as a
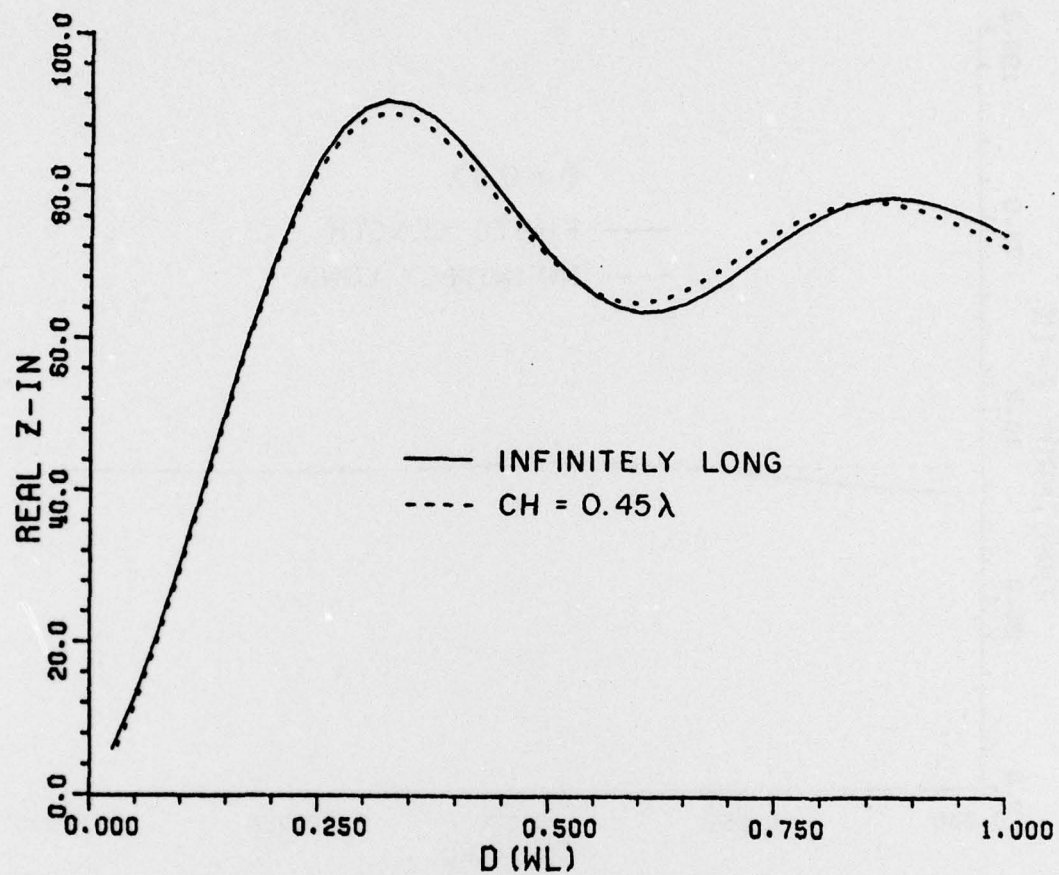function of cylinder height above dipole.

119

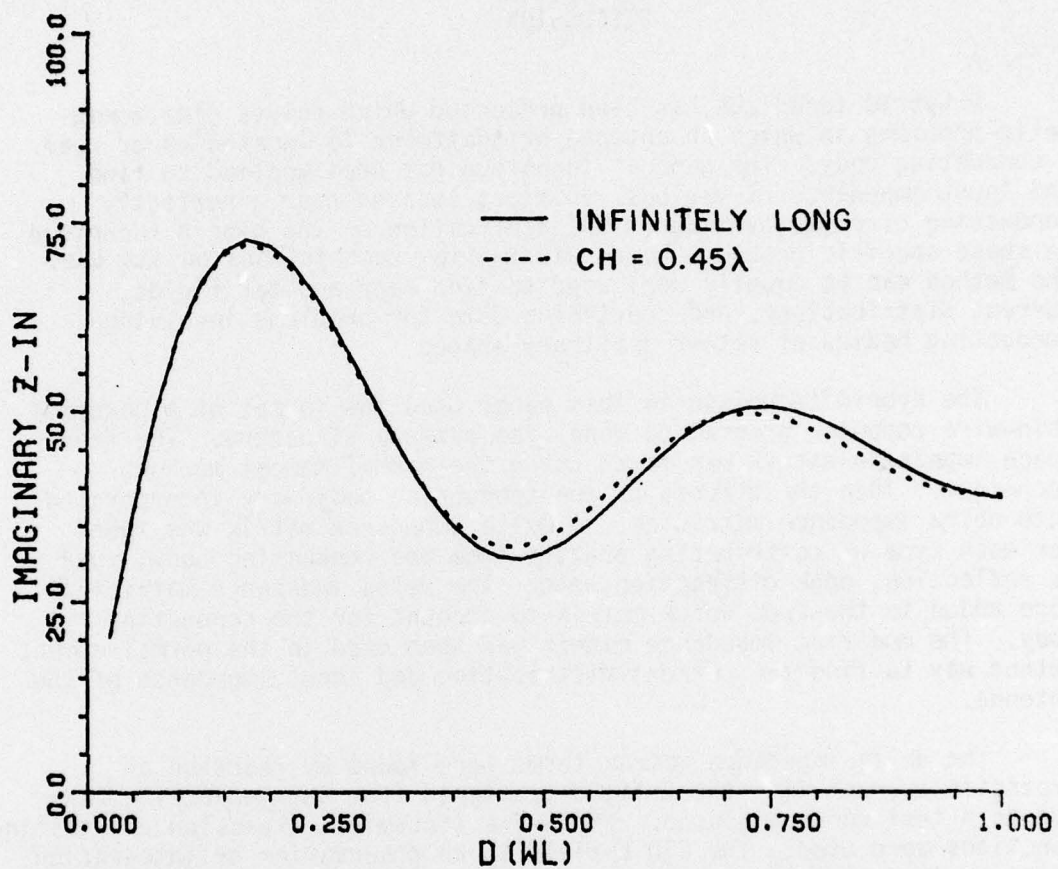Figure 53a. Real part of axial dipole input impedance near cylinder of radius A=0.25λ.

120

Figure 53b. Imaginary part of axial dipole input impedance
near cylinder of radius A=0.25λ.

CHAPTER V
DISCUSSION

A hybrid technique has been presented which solves electromagnetic problems in which an antenna or scatterer is located on or near a conducting body. The general technique has been applied to find the input impedance of various radiators located near a perfectly conducting circular cylinder. The application of the hybrid technique to these specific problems in no way implies restrictions on its use. The method can be equally well used to find near and far fields, current distributions, and scattering data for problems involving conducting bodies of rather arbitrary shape.

The hybrid technique in this paper used the format of a powerful thin-wire computer program to model the antenna structure. The free space impedance matrix was found using the normal moment method technique. Then the effects of the conducting body were incorporated into delta impedance matricies. A delta impedance matrix was found for each type of contributing scatter from the conducting body, such as reflection, edge diffraction, etc. The delta impedance matricies were added to the free space matrix to account for the conducting body. The modified impedance matrix was then used in the normal moment method way to find the current distribution and input impedance of the antenna.

The delta impedance matrix terms were found by reacting an expansion current with the E-field scattered from the conducting body due to a test current source. Piecewise sinusoidal expansion and testing functions were used. The GTD E-field at an observation or integration point on the receiving mode was composed of the superposition of end and feed point contributions from the source mode. Separating the contributions in this way accounted for the distributed nature of the source and resulted in spherical waves emanating from the points which were completely compatible with the ray optical nature of GTD. This way of combining thin-wire theory with GTD gave results that were far more accurate than other formats. Analytical justification as well as verification by example were presented in Chapter III.

The accuracy and facility of the hybrid technique were shown in Chapter IV by solving for the input impedance of various radiators as a function of their distance from a circular cylinder. Three orthogonal orientations were identified and antennas to match them were used. With the hybrid technique verified for these orthogonal orientations, clearly a more general radiator with an arbitrary combination of orientations could be solved with confidence.

122

An axially oriented half-wave dipole near the circular cylinder was solved by the hybrid technique. When the cylinder radius was large the hybrid technique was compared with an image theory solution. For small cylinder radii the hybrid solution was compared to an exact MM-eigenfunction solution. In both cases the agreement was excellent. For this orientation the solution was also compared with careful experimental measurements. The measurements were accomplished by doubling the input impedance of a quarter-wave monopole mounted with the cylinder over a ground and measuring the reflection coefficient. Results for both a thick and a thin dipole agreed very well with the measurements.

A radially oriented dipole presented a special problem in that ordinary GO predicted no effect on input impedance when the dipole was close to the cylinder. This incorrect solution was due to the non-zero ray path E-field which GO ignores. GO was extended to include a ray path field for this special orientation. The component reflects like image theory at the surface and then scatters as from a plane surface. Tilting the problem segment slightly from its exactly radial orientation offered another solution. Comparing the hybrid solution extended in these ways with image theory verified the techniques.

The circumferential orientation was verified with a square loop lying tangential to the circular cylinder. For large cylinder radii the hybrid solution agreed almost exactly with image theory. For smaller cylinder radii the solution was compared with experimental measurements made on a half-loop mounted with the cylinder over the ground plane. Both the thick and thin loop solutions tracked the impedance variations measured. The absolute levels were shifted slightly for two reasons. The frequency of operation was near resonance where rapidly varying impedance makes level matching difficult. Also, a section of line which was assumed to be ideal had a frequency dependent phase shift.

Thus, three orthogonal orientations were verified and the hybrid technique was clearly shown to be very accurate. A finite length cylinder was also investigated with the hybrid technique when an axial dipole was nearby. The results were compared with the infinitely long cylinder case. As expected, the finite length effects died out as the cylinder became longer.

Several minor limitations and restrictions on the hybrid technique can be pointed out. The antenna structure near the conducting body is limited in electrical size since the antenna must be modeled by wire segments no more than one-quarter wavelength in extent. The number of segments determines the number of modes and correspondingly the size of the impedance matrix the computer must work with. The conducting body must be a canonical shape or combination thereof for which GTD solutions exist for the canonical parts. Besides the field expressions, a method of finding the specular points on the surface must also be available.

123

In spite of the restrictions discussed, a very powerful hybrid technique has been presented for combining the moment method treatment of wire antennas with the GTD for curved surfaces. The method has been demonstrated to be accurate and versatile.

REFERENCES

[1]   Thiele, G. A. and Newhouse, T. M., "A Hybrid Technique for
       Combining Moment Methods with the Geometrical Theory of
       Diffraction," IEEE Trans. on Antennas and Propagation,
       Vol. AP-23, No. 1, January 1975.

[2]   Richmond, J. H., "Radiation and Scattering by Thin-Wire
       Structures in the Complex Frequency Domain," Report 2902-10,
       July 1973, The Ohio State University ElectroScience Laboratory,
       Department of Electrical Engineering; prepared under Grant
       NGL 36-008-138 for National Aeronautics and Space Administration.
       (NASA-CR-2396)

[3]   Richmond, J. H., "Computer Program for Thin-Wire Structures in
       a Homogeneous Conducting Medium," National Technical Informa-
       tion Service, Springfield, VA 22131, NASA Contractor Report
       CR-2399.

[4]   Kouyoumjian, R. G., and Pathak, P., "A Uniform Geometrical
       Theory of Diffraction for an Edge of a Perfectly Conducting
       Surface," Proc. of the IEEE, Vol. 62, No. 11, November, 1974,
       pp. 1448-1461.

[5]   R. J. Marhefka, "Analysis of Aircraft Wing-Mounted Antenna
       Patterns," Report 2902-25, June 1976, The Ohio State University
       ElectroScience Laboratory, Department of Electrical Engineering;
       prepared under Grant NGL 36-008-138 for National Aeronautics
       and Space Administration.

[6]   Stutzman, W. L., and Thiele, G. A., Modern Antenna Theory,"
       John Wiley and Sons, New York, 1979 (to be published).

[7]   Rumsey, V. H., "The Reaction Concept in Electromagnetic
       Theory," Physical Review, Ser. 2, Vol. 94, June 1954.

[8]   Deschamps, G., "Ray Techniques in Electromagnetics," Proc.
       IEEE, Vol. 60, pp. 1022-1035, September 1972.

[9]   Greer, E. D. and Burnside, W. D., "High Frequency Near Field
       Scattering by an Elliptic Disk," Report 4583-1, December 1976,
       The Ohio State University ElectroScience Laboratory, Department
       of Electrical Engineering; prepared under Contract N62269-76-C-
       0554 for Naval Air Development Center.

[10] Burnside, W. D., Yu, C. L., and Marhefka, R. J., "A Technique to Combine the Geometrical Theory of Diffraction and the Moment Method," IEEE Transactions on Antennas and Propagation, Vol. AP-23, pp. 551-558, July 1975.

[11] Ersoy, L., and Wang, N., "Surface Current and Charge Density Induced on an Infinite, Perfectly-Conducting Circular Cylinder in the Presence of Finite Axial Thin Wire - Transverse Magnetic Case," Report 4172-2, June 1977, The Ohio State University ElectroScience Laboratory, Department of Electrical Engineering; prepared under Contract F29601-75-C-0086 for Air Force Contract Management Division (PMRB), Kirtland Air Force Base, New Mexico.

[12] Richmond, J. H., "Computer Program for Thin-Wire Antenna over a Perfectly Conducting Ground," Report 2902-19, October 1974, The Ohio State University ElectroScience Laboratory, Department of Electrical Engineering; prepared under Grant NGL 36-008-138 for National Aeronautics and Space Administration. (NASA-CR-140622) (N74-34603)

[13] Richmond, J. H., personal communications.

[14] Richards, G. A., "Reaction Formulation and Numerical Results for Multiturn Loop Antennas and Arrays," Ph.D. Dissertation, The Ohio State University, 1970.